Characterisation of Transparent Conducting Thin Films Grown by Pulsed Laser Deposition and RF Magnetron Sputtering

Thesis submitted to
COCHIN UNIVERSITY OF SCIENCE AND TECHNOLOGY
in partial fulfillment of the requirements
for the award of the degree of
DOCTOR OF PHILOSOPHY

Manoj R

Department of Physics
Cochin University of Science and Technology
Cochin – 682 022, Kerala, India

October 2006

Characterisation of Transparent Conducting Thin Films Grown by Pulsed Laser Deposition and RF Magnetron Sputtering

Ph.D thesis in the field of material science

Author:

Manoj R
Optoelectronics Device Laboratory
Department of Physics
Cochin University of Science and Technology
Cochin – 682 022, Kerala, India
email: manojkochi@gmail.com

Supervisor:

Dr. M.K. Jayaraj
Reader
Optoelectronics Device Laboratory
Department of Physics
Cochin University of Science and Technology
Cochin – 682 022, Kerala, India
email: mkj@cusat.ac.in

October 2006

Dedicated to my Mother

Dr. M.K. Jayaraj
Reader
Department of Physics
Cochin University of Science and Technology
Cochin – 682 022

10th October 2006

Certificate

Certified that the work presented in this thesis entitled "*Characterisation of Transparent Conducting Thin Films Grown by Pulsed Laser Deposition and RF Magnetron Sputtering*" is based on the authentic record of research done by Mr. Manoj R under my guidance in the Department of Physics, Cochin University of Science and Technology, Cochin – 682 022 and has not been included in any other thesis submitted for the award of any degree.

Dr. M.K. Jayaraj

(Supervising Guide)

Phone : +91 484 2577404 extn 33 Fax: 91 484 2577595 email: mkj@cusat.ac.in

Declaration

Certified that the work presented in this thesis entitled "*Characterisation of Transparent Conducting Thin Films Grown by Pulsed Laser Deposition and RF Magnetron Sputtering* " is based on the original research work done by me under the supervision and guidance of Dr. M.K. Jayaraj, Reader, Department of Physics, Cochin University of Science and Technology, Cochin-682022 has not been included in any other thesis submitted previously for the award of any degree.

Cochin – 22
10th October 2006 Manoj R

Contents

Preface i
Chapter 1
Transparent Conducting Oxides
1.1 Introduction 5
1.2 General Properties of Transparent conducting Oxides 7

1.2.1 Theory of transparency and conductivity 7
1.2.2 Correlation of electrical and optical properties 8
1.2.3 Electrical properties 10
1.2.4 Optical properties and plasma frequency 11
1.2.5 Optical and Electrical Performance of Transparent Conductors 12
1.2.6 Work Function 13
1.2.7 Thermal Stability of Transparent Conductors 13
1.2.8 Minimum Deposition Temperature 14
1.2.9 Diffusion Barriers between Transparent Conductors and Sodium-Containing Glass Substrates 14
1.2.10 Etching Patterns in TCOs 14
1.2.11 Chemical Durability 14
1.2.12 Mechanical Hardness of TCOs 15
1.2.13 Production Costs 15
1.2.14 Toxicity 15

1.3 Structural classification of TCO 15
1.4 n-type Transparent Conductors 16
1.5 p- type Transparent Conductors 21
1.6 Conclusion 28
1.7 References 29

Chapter 2
Thin Film Deposition Techniques And Characterisation Tools
2.1 Introduction 37
2.2 Thin film Preparation Techniques 38
2.2.1 Thermal evaporation in vacuum by resistive heating 38
2.2.2 Electron beam evaporation 39
2.2.3 Sputtering 40
2.2.4 Pulsed Laser Deposition 45
i) Mechanisms of PLD 48

2.3 Characterisation tools 51
2.3.1 Thin film thickness 51
i) Optical interference method 51
ii) Stylus Profiler 52
2.3.2 X-ray diffraction studies 53
2.3.3 Scanning Electron Microscope (SEM) 55
2.3.4 Energy Dispersive X-Ray (EDX) Analysis 57
2.3.5 Atomic Force Microscopy (AFM) 59
2.3.6 Optical characterisation 61
i) Determination of band gap energy 61
ii) Photoluminescence 62
2.3.7 Electrical characterisation 65
i) Resistivity by two probe method 65
ii) Hall measurement 65
iii) Nature of conductivity – Carrier type 67
2.4 References 68

Chapter 3
Fabrication Of A Setup For Thermopower Measurements
3.1 Introduction 75
3.2 Experimental 75
3.2.1 Process control system 78
3.2.2 Block diagram 78
3.2.3 Control system parameters 79
3.2.4 Error 79
3.2.5 Variable range 80
3.2.6 Control parameter range 81
3.2.7 Continuous controller modes 81
i) The PID control 81
ii) Proportional control 82
iii) Integral control 84
iv) Derivative control 86
v) Proportional plus integral plus derivative control (PID) 87
3.3 Temperature Controller System - Hardware And SoftWare 88
3.3.1 Hardware 89
i) Sensors 89
ii) Interfacing 89
iii) Heater 90
3.3.2 Interfacing 91

3.3.3 Software 93
3.3.4 Heater 94
3.5 Conclusions 99
3.5 References 100

Chapter 4
Characterisation Of Pulsed Laser Deposited Zinc Oxide Thin Films
4.1 Introduction 105
4.2 Experimental 107
4.3 A Deposition Of Aluminium Doped Zinc Oxide Thin Films At High Temperatures. 108
4.3 B Deposition Of Aluminium Doped Zinc Oxide Thin Films At Room Temperature. 119
4.3 C Deposition Of Gallium And Nitrogen Codoped Zinc Oxide Thin Films At Room Temperature. 132
4.4 Conclusions 138
4.5 References 139

Chapter 5
Transparent Conducting Zinc Oxide Thin Film Prepared By Off Axis RF Magnetron Sputtering
5.1 Introduction 147
5.2 Experimental 147
5.3 Results and Discussions 151
5.4 Conclusion 158
5.5 References 159

Chapter 6
Properties Of RF Sputtered Calcium Doped $CuYO_2$ p-Type Transparent Conducting Films
6.1 Introduction 165
6.2 Experimental 166
6.3 Results and Discussions 168
6.4 Conclusion 179
6.5 References 180

Chapter 7
Summary and Outlook
7.1 Summary 185
7.2References 187
Appendix 189

Preface

Materials exhibiting transparency and electrical conductivity simultaneously, transparent conductors, Transparent conducting oxides (TCOs), which have high transparency through the visible spectrum and high electrical conductivity are already being used in numerous applications. Low-emission windows that allow visible light through while reflecting the infrared, this keeps the heat out in summer, or the heat in, in winter. A thin conducting layer on or in between the glass panes achieves this. Low-emission windows use mostly F-doped SnO_2. Most of these TCO's are n type semiconductors and are utilized in a variety of commercial applications, such as flat-panel displays, photovoltaic devices, and electrochromic windows, in which they serve as transparent electrodes. Novel functions may be integrated into the materials since oxides have a variety of elements and crystal structures, providing great potential for realizing a diverse range of active functions. However, the application of TCOs has been restricted to transparent electrodes, notwithstanding the fact that TCOs are *n*-type semiconductors. The primary reason is the lack of *p*-type TCOs, because many of the active functions in semiconductors originate from the nature of the *pn*-junction. In 1997, H. Kawazoe et al.[2] reported $CuAlO_2$ thin films as a first *p*-type TCO along with a chemical design concept for the exploration of other *p*-type TCOs. The first chapter describes the development of TCOs particularly ZnO and the delafossite structures p type TCOs.

The second chapter describes the different thin film deposition techniques used to deposit the p and n type TCOs and the different characterisation tools used to characterise the thin films. The thicknesses of the films were measured using Vecco Stylus profilometer.X-ray diffraction (XRD) studies were carried out to study the crystallograoghic properties of the thin films prepared. The energy dispersive X-ray analysis (EDX) and scanning electron microscopy (SEM) were used for evaluating the composition and morphology of the films. Optical properties were investigated using the UV-Vis-NIR spectrophotometer by recording the transmission/absorption spectra. The electrical properties were studied using the two probe and four

probe electrical measurements. Nature of conductivity of the films was determined by thermo probe and thermo power measurements. The deposition conditions and the process parameters were optimised based on these characterisations.

The third chapter describes the fabrication of an automated setup for the measurement of thermopower of thin films. Depending upon the sign of the thermoemf developed the nature of the charge carriers is determined. The hole mobility of the delafossite p type TCOs is generally low. This makes it difficult to determine the type of carriers by conventional hall measurement. Thermopower measurement is a method used to determine the nature of the charge carriers. For testing the thermopower measurement setup fabricated, the thermopower of copper is measured. The result obtained agrees well with the reported value for copper. The third chapter describes the fabrication and working of the thermopower setup in detail.

Fourth chapter deals with the deposition and characterisation of zinc oxide thin films deposited by pulsed laser deposition. The second and third harmonics of Nd:YAG were used to deposit the thin films. Thin films were deposited on fused quartz, Polyimide and Polyethylene terathalate (PET) substrates. The room temperature deposited thin films showed reasonable conductivity and good transmittance.

5% gallium doped zinc oxide thin films were deposited by PLD at room temperature in presense of a mixture of N_2O and O_2 gasses. The deposited films were amorphous by X–ray analysis. The films showed p type conductivity by thermopower analysis. The films showed > 80% transmittance in the visible range.

The films grown on quartz and PET substrates are highly transparent (>85%) in the visible region. The polyimide substrate, which is coloured, absorbs radiation below 500 nm and the transmission above 550 nm is about 60%

Fifth chapter describes the deposition of the ZnO and ZnO:Al thin films by off axis magnetron sputtering. Smooth films could be grown by the off axis configuration. Highly transparent and conductive films were deposited by

off axis magnetron sputtering. Undoped zinc oxide and aluminum doped zinc oxide films were prepared by rf magnetron sputtering of presynthesised target. All the films exhibit a transmission over 80% in the visible region. The electrical resistivity of the film strongly depends on the substrate temperature, substrate to target distance and orientation of the substrate. The increase in conductivity is due to the increase of carrier concentration and also due to the increased mobility of the carriers. Under the optimized deposition condition the ZnO:Al film show a resistivity 4.5X 10^{-4}ohm cm with transparency of >85%. Morphology of the films shows the films are very smooth. p–n junctions were fabricated with the p type zinc oxide deposited by the co doping of gallium and nitrogen by pulsed laser deposition and the n type aluminium doped zinc oxide thin films.

Sixth chapter describes the deposition of the delafossite structured calcium doped copper yittrium oxide thin films. The films were deposited in the on axis configuration at 80W rf power and 100°C substrate temperature. The conductivity of the films can be controlled by the oxygen intercalation into the thin films. Oxygen intercalation is acheived by annealing the thin films in various pressures of oxygen atmosphere at 420°C for one hour. The Ca doped $CuYO_2$ thin films prepared by RF magnetron sputtering show p-type conductivity (8 Scm^{-1}) after the oxygen intercalation. The conductivity can be increased by oxygen intercalation but at the expense of transmission. The Seebeck coefficient of +274 $\mu V\ K^{-1}$ confirms the p-type conduction in these materials. The temperature dependence of the conductivity indicates a predominant hopping conduction mechanism. The films become amorphous on annealing at one atmosphere oxygen pressure. The pn junctions formed by the p type calcium doped copper yttrium oxide and the n type aluminium doped zinc oxide thin films. These junctions show a forward to reverse ratio of 1.3 at 5 V.

Publications relating to the work presented in the Thesis

1. Characterisation of pulsed laser deposited ZnO:Al thin films, **R.Manoj**, M.K.Jayaraj, Thin Solid Films, Submitted
2. Effect of Oxygen intercalation on the properties of sputtered $CuYO_2$ p-type transparent conducting films, **R. Manoj**, M. Nisha, K. A. Vanaja, M. K. Jayaraj, Bull of Material Science to be submitted
3. Transparent conducting zinc oxide thin film prepared by off-axis rf magnetron sputtering, M.K.Jayaraj, Aldrin Antony, and **R.Manoj** Bull of Material Science 25 (2002) 227

Conference Proceedings

1. Growth of zinc oxide thin films for optoelectronic application by pulsed laser deposition. K. J. Saji, **R. Manoj**, R. S. Ajimsha, and M.K. Jayaraj, Proc. SPIE **6286**, (2006), 62860D.
2. Effect of oxygen partial pressure on growth of Pulsed Laser Deposited ZnO:Al thin films, **Manoj R**, Maneesh C, Aldrin Antony and M.K. Jayaraj, *Second National symposium on Pulsed Laser Deposition of thin films, India 2003.*
3. Preparation of ZnO:Al thin films by pulsed laser deposition, **Manoj.R**, Aldrin Antony, Vineeth.C and M.K.Jayaraj, Proc.of DAE-BRNS National Laser Symposium,Thiruvanthapuram, India (2002) P423
4. Preparation of ZnO.Ga thin films by pulsed laser deposition, Vineeth.C, **Manoj.R,** Aldrin Antony, Reeja.M, and M.K.Jayaraj, Proc. DAE Solid State Physics Symposium, Chadigarh, India Vol 45 (2002) P329

Other publications to which author has contributed.

1. Effect of substrate temperature on the growth of ITO thin films, Nisha M, Anusha S, Aldrin Antony, **Manoj R** and M.K. Jayaraj, Applied Surface Science 252(2005) 1430
2. Electrical and optical properties of $ZnGa_2O_4$ thin films deposited by pulsed laser deposition, K Mini Krishna, M.Nisha, R Reshmi, **R Manoj,** A.S.Asha, M.K.Jayaraj, Materials Forum 29 (2005) 243.
3. Pulsed laser deposition of $ZnGa_2O_4$ phosphor thin films, R.Reshmi, K.Minikrishna, **R.Manoj**, M.K.Jayaraj, Surface and Coating Technology 198(2005) 345.
4. Effect of pH on the growth and properties of chemical bath deposited ZnS thin films, Aldrin Antony, K.V. Murali, **Manoj**

R.,M.K.Jayaraj,Materials Chemistry and Physics 90/1 (2005) 106

5. Growth of $CuInS_2$ thin films by sulphurisation of Cu-In alloys, Aldrin Antony, Asha A.S., Rahana Yoosuf, **Manoj R**., M.K.Jayaraj, Solar Energy Materials and Solar Cells 81 (2004) 407
6. Influence of target to substrate spacing on the properties of ITO thin films, Aldrin Antony, Nisha M., **Manoj R**., M.K. Jayaraj, Applied Surface Science 225 (2004) 294
7. Preparation and characterisation of ZnS thin films by chemical bath deposition and electron beam evaporation, Murali K.V., Aldrin A, **Manoj R**. and M. K. Jayaraj, Materials, Active Devices and Optical Amplifiers, (Eds) C. Hasnain, J. Connie, H. Dexiu, N. Yoshiaki, R. Xiaomin, in: Proc. SPIE Int. Conf. APOC 2003, Wuhan,China, 5280 (2004) p600
8. β-In_2S_3 Thin Films Prepared by The Sulphurisation of Evaporated Indium Films, Rahana Yoosuf, Jerome Kalloor Cheekku, Aldrin Antony, **Manoj Ramachandran** and Madambi K. Jayaraj, Materials, Active Devices and Optical Amplifiers, (Eds) C. Hasnain, J. Connie, H. Dexiu, N. Yoshiaki, R. Xiaomin, in: Proc. SPIE Int. Conf. APOC 2003, Wuhan,China, 5280 (2004) p669
9. Influence of substrate temperature on the properties of rf magnetron sputtered ITO thin films, Anusha S, Nisha M, Aldrin Antony, **Manoj R** and M.K. Jayaraj, *DAE Solid State Physics Symposium,India 2003*
10. Growth of Single Phase In_2S_3 Films by Chalcogenisation of Metallic Indium Films, Rahana Yoosuf, Aldrin Antony, **Manoj R**, Mini Krishna, Nisha M and M.K.Jayaraj, *DAE Solid State Physics Symposium,India 2003*
11. Effect of heat treatment on the properties of rf magnetron sputtered ITO thin films, M.Nisha, Aldrin Antony, **Manoj.R** and M.K.Jayaraj, Proc. DAE Solid State Physics Symposium, Chandigarh, Inida Vol 45 (2002) P327
12. Chemical Bath deposition of indium doped ZnCdS Thin Films. Aldrin Antony, **Manoj.R** and M.K.Jayaraj, Proc. National conference on Thin Film Techniques and applications,Coimbatore, India (2002) P68.

Chapter 1

Transparent Conducting Oxides

This chapter gives an overview of the development of transparent conducting oxides, particularly the zinc oxide as an n type conductor. The recent development of delafossite materials as p type transparent conductors brings the possibility of uv emitting light emitting diodes and transparent p–n junctions.

1.1 Introduction

Materials exhibiting transparency and electrical conductivity simultaneously, transparent conductors, have been the focus of frontier research ever since the first report of transparent conducting CdO films. [1] Transparent conducting oxides (TCOs), which have high transparency through the visible spectrum and high electrical conductivity are already being used in numerous applications. Low-emission windows that allow visible light through while reflecting the infrared, this keeps the heat out in summer, or the heat in, in winter. A thin conducting layer on or in between the glass panes achieves this. Low-emission windows use mostly F-doped SnO_2. Most of these TCO's are n type semiconductors and are utilized in a variety of commercial applications, such as flat-panel displays, photovoltaic devices, and electrochromic windows, in which they serve as transparent electrodes. Novel functions may be integrated into the materials since oxides have a variety of elements and crystal structures, providing great potential for realizing a diverse range of active functions. However, the application of TCOs has been restricted to transparent electrodes, notwithstanding the fact that TCOs are *n*-type semiconductors. The primary reason is the lack of *p*-type TCOs, because many of the active functions in semiconductors originate from the nature of the *pn*-junction. In 1997, H. Kawazoe et al.[2] reported $CuAlO_2$ thin films as a first *p*-type TCO along with a chemical design concept for the exploration of other *p*-type TCOs. This has led to the fabrications of all oxide transparent diodes and transistors [3].

TCO's are wide band gap materials that have relatively high concentration of carriers in the conduction band. These arise either from defects in the material or from extrinsic dopants, the impurity level of which lie near the conduction band edge. The high carrier concentration would cause absorption of electromagnetic radiation. Thus a TCO represents a compromise between electrical conductivity and optical transmission. Reduction of resistivity involves either increase in the carrier concentration or in their mobility. The mobility of typical semiconductor is about 40 $cm^2\ V^{-1}\ s^{-1}$. Increasing the number of carriers leads to an increase in the

visible absorption while increasing the mobility has no negative effects on the figure of merit of the TCOs. Thus increasing the figure of merit of the TCOs essentially should aim to increase the mobility since this would increase the optical transmission and electrical conductivity

The relationship between mobility and carrier density of semiconductors is shown in figure 1.1 [4]
Conductivity is given by the relation

$$\sigma = \frac{\left(ne^2 t\right)}{\left(m\right)} \ \Omega^{-1}\text{cm}^{-1} \qquad (1.1)$$

Where, n is the carrier density, e the electronic charge, t the thickness of the semiconductor and m the mass of the charge carriers.

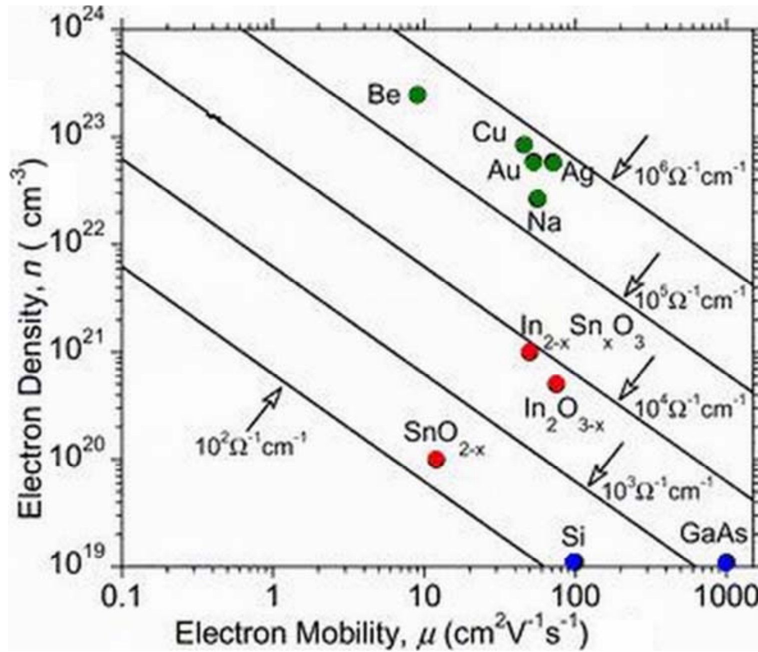

Figure 1.1 Relationship between mobility and carrier density of semiconductors

The lack of high-quality epitaxial or single-crystalline transparent oxide semiconductor films is another reason for their limited application. Although there have been many reports of the fabrication of transparent optoelectronic devices such as *pn*-junction diodes and transistors using transparent oxide semiconductors (TOSs), their performance is significantly inferior to III-V semiconductor devices because the thin films are polycrystalline, i.e. defects and grain boundaries in the active layer deteriorate the device performance. Optoelectronic properties and, therefore, device performance are expected to improve drastically by using single-crystalline or high-quality epitaxial film in place of nonoriented polycrystalline films [5]. The development of a high figure-of-merit p-type TCO would enable development of ultraviolet light emitting diodes, heterojunctions for solar cells, and all oxide transparent semiconductor devices such as diodes and transistors.

1.2 General Properties Of Transparent Conducting Oxides

1.2.1 Theory of transparency and conductivity

As far as the properties of a solid are concerned, one can see that optical transparency and electrical conductivity are antonyms to each other. This can be easily proved using the Maxwell's equations of electromagnetic theory [6] as described below.

For electromagnetic (em) waves passing through an uncharged semiconducting medium, the solution to Maxwell's equation gives the real and complex parts of the refractive index as

$$n^2 = \frac{\varepsilon}{2}\left[\left\{1+\left(\frac{2\sigma}{\upsilon}\right)^2\right\}^{1/2}+1\right] \quad \text{and}$$

$$k^2 = \frac{\varepsilon}{2}\left[\left\{1+\left(\frac{2\sigma}{\upsilon}\right)^2\right\}^{1/2}-1\right] \qquad (1.2)$$

where n is the refractive index of the medium, k is the extinction coefficient, ε is the dielectric constant, σ is the conductivity of the medium and ν is the frequency of the electromagnetic radiation. In the case of an insulator, where $\sigma \to 0$, then $n \to \varepsilon^{1/2}$ and $k \to 0$. This implies that an insulator is transparent to electromagnetic waves.

For a perfect conductor, the solution to the Maxwell's equation yields, the reflected and transmitted component of the electric field vector as $E_R = -E_I$ and $E_T = 0$. This means that the wave is totally reflected with 180^0 phase difference. In other words, a good conductor reflects the radiations incident on it, while a good insulator is transparent to the electromagnetic radiations.

1.2.2 Correlation of electrical and optical properties

The optical phenomena in the IR range can be explained on the basis of Drude's theory for free electrons in metals [7,8,9]. When the free electrons interact with an em field, it may lead to polarisation of the field within the material. It affects the relative permittivity ε. For an electron moving in an electric field, the equation of motion can be written as,

$$m\left(\frac{d}{dt}+\frac{1}{\tau}\right)\delta v(t) = F \qquad (1.3)$$

where τ is the relaxation time .

The force on an electron in an alternating field is given by

$$F = -eE\, e^{-i\omega t} \qquad (1.4)$$

Let us assume a solution to (1.4) in the form $\delta v = \delta v\, e^{-i\omega t}$

Then (1.3) becomes,

$$m\left(-i\omega+\frac{1}{\tau}\right)\delta v = -eE$$

or ,

$$\delta v = -\frac{e\tau/m}{1-i\omega\tau} \qquad (1.5)$$

The current density is

$$j = nq\delta v = \frac{ne^2\tau}{m(1-i\omega\tau)}E ,$$

where n is the electron concentration and q is the charge on the electron.

The electrical conductivity is

$$\sigma(\omega) = \frac{ne^2\tau}{m(1-i\omega\tau)} = \sigma_0 \frac{1+i\omega\tau}{1+(\omega\tau)^2} \qquad (1.6)$$

Here, $\sigma_0 = ne^2\tau / m$ is the dc conductivity.

At high frequencies, $\omega\tau >>1$, we can write,

$$\sigma(\omega) = \sigma_0\left(\frac{1}{(\omega\tau)^2} + \frac{i}{\omega\tau}\right) = \frac{ne^2}{m\omega^2\tau} + i\frac{ne^2}{m\omega}$$

In this equation the imaginary term is dominant and is independent of τ. Thus we can express the result as a complex dielectric constant instead of expressing it as a complex conductivity.

The dielectric constant $\varepsilon = 1 + (4\pi P/E)$

where $P = -\dfrac{ne^2/m}{\omega^2 + i\omega/\tau}E$

Then,

$$\varepsilon(\omega) = 1 - \frac{4\pi ne^2/m}{\omega^2 + i\omega/\tau} \qquad (1.7)$$

This expression gives the dielectric constant of a free electron gas. For $\tau \to \infty$ the dielectric constant is positive and real if $\omega^2 > 4\pi ne^2/m$.

Electromagnetic wave cannot propagate in a medium with negative dielectric constant because then wave vector is imaginary and the wave decays exponentially. Waves incident on such a medium are totally reflected. We can denote the cut off frequency as $\omega_p = \left(4\pi ne^2/m\right)^{1/2}$ this is known as the

plasma frequency. The material is transparent to the em radiation whose frequency is greater than the plasma frequency.

1.2.3 Electrical properties

Numerous investigations have been made on the electrical properties of transparent conducting oxide films to understand the conduction phenomena [10,11]. Researchers have made a systematic study on the effect of various parameters such as nature of substrate, substrate temperature, film thickness, dopant and its concentration etc [12,13] on the electrical properties of TCO films.

The high conductivity of the TCO films results mainly from non stoichiometry. The conduction electrons in these films are supplied from donor sites associated with oxygen vacancies or excess metal ions[14]. These donor sites can be easily created by chemical reduction. Unintentional doping(which happens mainly in the case of film deposition by spray pyrolysis), intentional doping and contamination by alkali ions from the glass substrate can affect electrical conductivity.

One of the major factor governing the conductivity of TCO films is the carrier mobility. The mobility of the carriers in the polycrystalline film is dependent on the mechanism by which carriers are scattered by lattice imperfections. The various scattering mechanisms involved in semiconducting thin films are acoustic deformation potential scattering [15], piezoelectric scattering [16], optical phonon scattering [17] neutral impurity scattering [18], ionized impurity scattering [19], electron-electron scattering [20] and grain boundary scattering [21].

In the case of a polycrystalline film, the conduction mechanism is dominated by the inherent inter-crystalline boundaries rather than the intra-crystalline characteristics. These boundaries generally contain fairly high densities of interface states that trap free carriers by virtue of the inherent disorders and the presence of trapped charges. The interface states results in a space charge

region in the grain boundaries. Due to this space charge region, band bending occurs, resulting in potential barriers to charge transport.

1.2.4 Optical properties and plasma frequency

The optical properties of a transparent conducting film depend strongly on the deposition parameters, microstructure, level of impurities and growth techniques. Being transparent in the visible and NIR range and reflecting to IR radiations, they act as selective transmitting layer. The transmission spectrum of a TCO is given in figure 1.2.

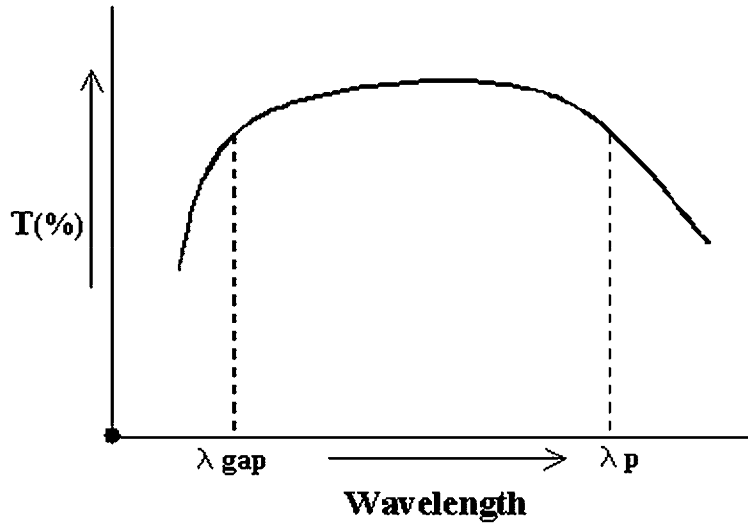

Figure 1.2. Transmission spectrum of TCO

The Transmission spectrum shows that for wavelengths longer than plasma wavelength the TCO reflects radiation while for shorter wavelengths TCO is transparent. At frequencies higher than the plasma frequency, the electrons cannot respond to the changing electric field of the incident radiation, and the material behaves as a transparent dielectric. At frequencies below the plasma frequency, the TCO reflects the incident radiation while at frequencies above the band gap of the material, the material absorbs the incident radiation. For most TCO materials, the plasma frequency falls in the near-infrared part of the spectrum, and the visible region is in the higher,

transparent frequency range. The plasma frequency increases approximately with the square root of the conduction-electron concentration. The maximum obtainable electron concentration and the plasma frequency of TCOs generally increase in the same order as the resistivity[22].

1.2.5 Optical and Electrical Performance of Transparent Conductors

TCOs have two important qualities with which they can be judged, optical transmission and electrical conductivity, and these two parameters are somewhat inversely related, a method of comparing the properties of these films is essential. Figure of merit have allowed researchers to compare the various results in a reasonable and direct manner. Researchers have developed different methods for finding the figures of merit of the films.

One of the earliest equations defining a figure of merit was developed by Fraser and Cook[23] and is given by the relation $F_{FC} = \frac{T}{R_s}$ where T is the transmission and R_s is the sheet resistance of the thin film. This value was often multiplied by 1000 to allow comparisons of numbers greater than one. This definition depends on the film thickness.

Another definition for figure of merit, F_H, developed by Haacke [24] is also related to the above definition. However, F_H puts more emphasis on the optical transparency because F_{FC} was too much in favor of sheet resistance, resulting in a maximum figure of merit at relatively large film thicknesses. The figure of merit was redefined as $F_H = \frac{T_a^x}{R_s}$ where $x>1$. Haacke selected the value of $x = 10$. The definition by Haacke is also thickness dependent.

The third definition for figure of merit was developed by Iles and Soclof [25]. A figure of merit that is independent of film thickness is given by

$$F_{1s} = R_s\left[1 - T\right] = \frac{\alpha}{\sigma}$$

By this definition, a lower value of figure of merit indicates films of better quality.

Most of the variation in the figure of merit of TCO is due to differences in mobility, but the free-electron concentration does not affect the figure of merit. The electron mobility is determined by the electron-scattering mechanisms that operate in the material. First of all, some scattering mechanisms, such as scattering of electrons by phonons, are present in pure single crystals. Practical TCOs need much higher doping levels and for these high doping levels, scattering by the ionised dopant atoms become another important mechanism that alone limits the mobility. This maximum mobility is lowered still further by other scattering mechanisms such as grain-boundary scattering, present in polycrystalline thin films. The best TCO films, ZnO:F and Cd_2SnO_4, have been prepared with mobilities in the range of 50–60 $cm^2\ V^{-1}\ s^{-1}$[26].

1.2.6 Work Function

The work function of a TCO is defined as the minimum energy required to remove an electron from the fermi level to the vacuum level. ZnO has a work function of 4.57eV [27].

1.2.7 Thermal Stability of Transparent Conductors

TCOs will generally will have an increase in resistivity if heated to a high enough temperature for a long enough time. TCOs remains stable to temperatures slightly above the optimised deposition temperature.

1.2.8 Minimum Deposition Temperature

The substrate temperature, during deposition of TCO thin films, must be at a sufficiently high in order to develop the required properties for the TCO. The required temperatures are usually found to increase in the following order: $ITO<ZnO<SnO_2<Cd_2SnO_4$ [10]. ITO is preferred for deposition on thermally sensitive substrates, such as plastic, while cadmium stannate requires highly refractory substrates to achieve its best properties.

1.2.9 Diffusion Barriers between Transparent Conductors and Sodium-Containing Glass Substrates

When TCOs are deposited on sodium containing glass, such as soda-lime glass, sodium can diffuse into the TCO and increase its resistance. This effect is particularly noticeable for tin oxide, because sodium diffuses rapidly at the high substrate temperatures (often 550^0C) used for its deposition. It is common to deposit a barrier layer on the glass prior to the deposition of tin oxide. Silica or alumina is used commonly as the barrier layer between soda-lime glass and tin oxide.

1.2.10 Etching Patterns in TCOs

For some applications of TCOs, such as displays, heaters, or antennas, parts of the TCO must be removed. Zinc oxide is the easiest material to etch, tin oxide is the most difficult, and indium oxide is intermediate in etching difficulty [10]. Series-connected thin-film solar cells need to remove TCOs along patterns of lines. This removal is usually carried out by laser ablation.

1.2.11 Chemical Durability

The ability of a TCO to withstand corrosive chemical environments is inversely related to its ease of etching. Tin oxide is the most resistant TCO, while Zinc oxide is readily attacked by acids or bases.

1.2.12. Mechanical Hardness of TCs

The mechanical durability of TCOs is related to the hardness of the crystals from which they are formed. Titanium nitride and tin oxide are even harder than glass and can be used in applications that have these coatings exposed. Zinc oxide is readily scratched, but can be handled with care. Thin silver films are so fragile that they cannot be touched and can be used only when coated with protective layers.

1.2.13. Production Costs

The costs of producing a transparent conducting material depend on the cost of the raw materials and the processing of it into a thin layer. The cost of the raw materials generally increases in this order: Cd <Zn<Ti< Sn< Ag< In. The costs of the deposition methods typically increase in the following order: Atmospheric pressure CVD<Vacuum Evaporation <Magnetron Sputtering<Low-Pressure CVD < Sol-gel <Pulsed Laser Deposition. The speed of the process is also very important in determining the cost.

1.2.14 Toxicity

Some of the elements used in TCOs are toxic. This increases the cost of processing them because of the need to protect workers and prevent the escape of toxic materials into the environment[10]. Toxicity of the elements generally increases in as Zn<Sn<In<Ag<Cd. Cadmium compounds are carcinogens and thus are heavily regulated and even prohibited from being used for some applications.

1.3 Structural Classification Of TCO

Ingram et al classifies TCO structurally into four main families [28] as given in table1.1. The first family has cations tetrahedrally coordinated by oxygen, and is *n*-type in character. ZnO is the only known oxide to possess this coordination exclusively. The second family has cations in octahedral

coordination, and is also *n*-type in character. This is the largest family of TCOs, including CdO, In_2O_3, SnO_2,$CdIn_2O_4$, Cd_2SnO_4, and most of the best *n*-type complex oxide materials. The third family of TCOs has cations in linear coordination with oxygen, and is *p*-type in character. This family includes $CuAlO_2$, related Cu- and Ag-based delafossites and $SrCu_2O_2$. Finally, the cage-structure oxide, $12CaO{\cdot}7Al_2O_3$, is listed as the first member of a potential new family of TCOs; it is *n*-type in character.

Table 1.1. Families of transparent conducting oxides.

Structural feature	**Carrier type**	**Examples**
Tetrahedrally-coordinated cations	*n*-type	ZnO
Octahedrally-coordinated cations	*n*-type	CdO, In_2O_3, SnO_2, Cd_2SnO_4, etc.
Linearly-coordinated cations	*p*-type	$CuAlO_2$, $SrCu_2O_2$, etc.
Cage framework	*n*-type	$12CaO{\cdot}7Al_2O_3$

1.4 n -Type Transparent Conductors

Tin doped Indium oxide (ITO) is one of the most popular transparent oxide semiconductor that has been widely studied and used commercially. ITO has electrical conductivity of ~ 10^4 Ω^{-1} cm^{-1} and transmission of > 80%. This close to metallic conductivity, in a material that is transparent, has resulted in many important applications like current spreading layers in light emitting diodes and thermal insulation for windows [29]. The high cost of indium and tin has spawned the search for an alternative for ITO and zinc oxide is fast emerging as an alternative.

The absolute limit to the resistivity would be 3 x 10^{-5} Ω cm for the TCOs and the corresponding carrier concentration would be about 9 x 10^{21} cm^{-3} [30]. At higher concentrations, the reflectivity due to the carriers would be very high and the film can no longer be used as a transparent conductor.

The unique optoelectronic properties of zinc oxide, the low cost and its non-toxicity have attracted considerable interest over the last few years. The optical and electrical properties, high chemical and mechanical stability makes ZnO as one of the most promising material for TCO. The abundance of ZnO in nature makes it a low cost material than most of the currently used TCO's (SnO_2, ITO). The average amount of zinc available on earth's crust is 132 ppm while Indium is only 0.1 ppm and tin is 40 ppm. zinc oxide occurs in nature as the mineral zincite. Zinc oxide crystallises in the hexagonal wurtzite (B 4-type) lattice. The zinc atoms are nearly in the position of hexagonal close packing. Every oxygen atom lies within a tetrahedral group of four zinc atoms. All these tetrahedras point in the same direction along the hexagonal axis giving the crystal its polar symmetry. The wurtzite structure is shown in figure 1.3.

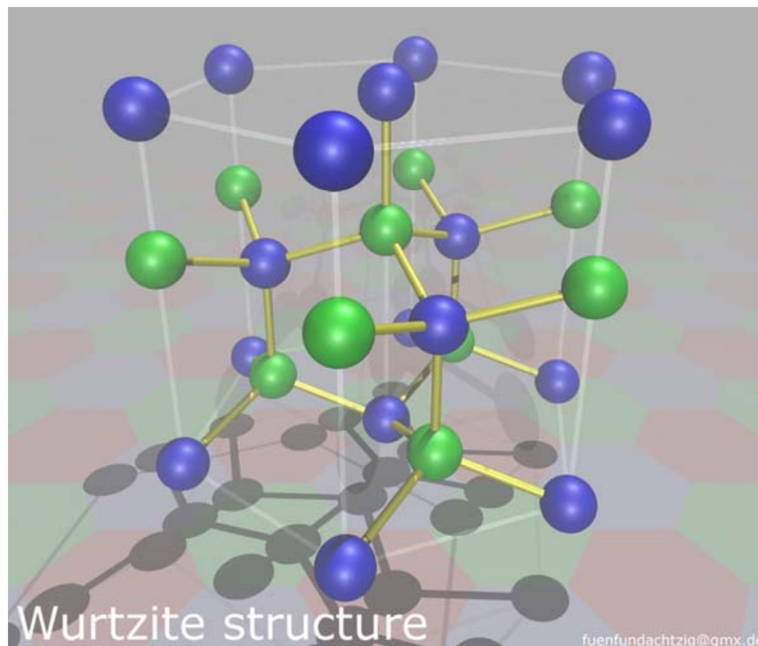

Figure 1.3. Wurtzite structure of ZnO

The lattice constants are a = 3.24 A^o and c = 5.19 A^o [14]. The fundamental band gap of ZnO has been calculated from the band structure models to be 3.5 eV [31].

Zinc oxide has attracted the interest of researchers due to its various properties over the years, as a TCO much research has been carried out and more recently the reports of p type doping in ZnO has ensured that this material remains in the focus of frontiers of material research for some more time. The stability of ZnO has prompted it to be used in space applications. Tonon et al have irradiated ZnO pigments coated on aluminium substrates with electrons and protons and studied the degradation of ZnO. The studies conclude that the damage rate is low for ZnO [32]. Thin films of ZnO are suitable as electrode material for optoelectronic devices. ZnO has been grown on InP and Si substrates with more than 80% transmission and resistivity as low as $3 \times 10^{-4}\ \Omega$ cm [33].

Acoustoelectric devices such as surface acoustic wave devices (SAW) have been fabricated with ZnO. For example a 1.5 G Hz. SAW filter with a minimum loss of 1.3 dB and a stopband attenuation of more than 30 dB in the frequency range below that of passband which can be used in mobile communication terminals has been fabricated [34]. Due to the unique conducting mechanism based on oxygen vacancies, ZnO has been used to fabricate oxygen gas sensors. ZnO also exhibit good piezoelectric properties. ZnO and ZnO:Al thin films have been deposited by rf planar magnetron sputtering. The piezoelectric properties of ZnO enable the fabrication of gas sensors in the SAW structure. ZnO:Al thin films have better sensitivity towards O_2 [35]. Diluted magnetic semiconductors in which magnetic ions substitute for cations of the host semiconductor material are assumed to be ideal systems for spintronics. 3d transition metal doped ZnO have shown ferromagnetic behaviour above room temperature [36]. The varistors prepared by mixing zinc oxide with oxides of various metals finds application as surge controllers in electronic industry [37].

ZnO shows very strong spontaneous and stimulated emissions by excitons even at room temperature. This implies that the ZnO can be used for fabricating light emitting diodes(LED) and Laser diodes (LD). Theraja et al have demonstrated random lasing action in optically pumped ZnO powder

sample. The lasing action is attributed to multiple scattering in the powder [38]. Bagnall et al report the laser emission from exciton – exciton scattering at intermediate intensities and electron - hole plasma emission at higher intensities for MBE grown ZnO epilayers with a threshold intensity of 240 kW cm^{-1} [39]. The non linear optical response of ZnO thin films prepared by pulsed laser deposition (PLD) for various thickness and crystallinity show that the second order susceptibility to be as large as 10 pm/V. These non linear effects originate at the grain boundaries and interfaces. [40]

Doping of ZnO films with Al, Ga, In, Ge, improves their electrical conductivity. [41] Aluminium doped zinc oxide films show high transmittance from UV to near IR region and nearly metallic electrical conductivity. They are used as the transparent electrodes in solar cells. Al doped ZnO films have been widely studied and have low resistivity of $2 – 5 \times 10^{-4}\ \Omega$ cm, which is comparable to that of ITO films.

Various methods of thin film preparation have been used for the growth of ZnO; like evaporation [42], Chemical vapour deposition (CVD) [43], spray pyrolysis [44], magnetron sputtering [45] and pulsed laser deposition (PLD) [46]. For growing high quality ZnO films PLD has attracted much attention since PLD enables the growth of high quality thin film at relatively low substrate temperature.

Ohya et. al [47] have used dip coating to deposit ZnO thin films. The films were initially fired at various temperatures ranging from 400 ^{o}C to 700 ^{o}C for 30 minutes or 1 hour. The resistivities of such films were very high. The films were later annealed at 500 ^{o}C to 700 ^{o}C in N_2 atmosphere for 30 minutes this reduced the resistivity by two orders of magnitude. As the aluminium content is increased the resistivity increases while as the indium content increases, the resistivity decreases. ZnO thin films deposited by spray pyrolysis at a substrate temperature of 500 ^{o}C and the effect of Al and In doping has been studied. The effects of annealing in vacuum and argon atmosphere at 300 ^{o}C were also studied and indium is reported to be a better dopant than Al for ZnO [48].

Effect of N doping on the properties of ZnO films has been studied by Y. Sato et. al. [49] Zinc was evaporated in mixture of oxygen and nitrogen atmosphere. N_2/ N_2+ O_2 varied from 0 % to 100%. 80 W RF discharge was used to excite the gasses in order to increase their reactivity. Resistivity increases from 0.1 Ω cm to 10 Ω cm as more N is incorporated into the films.

Reactive evaporation with dc glow discharge in a controlled O_2 atmosphere was used to grow ZnO films of resistivity 1.4 X 10^{-3} Ω cm and transmission greater than 90% [50]. The study of growth processes of ZnO thin films by PLD indicates polycrystalline growth for thin films as thin as 10 nm and oriented growth from about 50 nm. Initial growth is an amorphous layer of ZnO on glass, since the energy of formation of glass ZnO interface is very large, no crystalline phase occurs. The growth of ZnO further on the amorphous layer of ZnO requires less energy for crystallizing hence polycrystalline ZnO begins to grow from about 10 nm. After 50 nm thickness oriented ZnO grows upon the polycrystalline ZnO [51].

The films grown even in the presence of O_2 background pressure were oxygen deficient. Though the films grown in vacuum ($ZnO_{0.75}$) were more deficient than those grown in presence of 5 mtorr ($ZnO_{0.95}$) O_2 gas, none of the films were stoichiometric [52].

The PL emission spectrum of ZnO has been extensively studied. The large excitonic binding energy of ZnO, almost 60 MeV, make it a promising candidate as UV emitter. The PL emission at 385 nm is due to the band gap emission. The PL spectrum of ZnO obtained by exciting with 270 nm shows emissions at 380 nm and 520 nm. PL spectra obtained after the samples were irradiated with electrons and protons showed a quenching of the 520 nm line. The fact that the 520 nm line is more quickly quenched in both cases even though the total dose of the electron irradiation was less suggests that the nature of defects involved in optical degradiation is the same with electrons and protons. The 380 nm line is attributed to the band gap emission of the material while the 520 nm line is attributed to the emission due to structural

disorder. This could be either due to oxygen vacancies or interstitial zinc ions [53].

The luminescent centres should be related to one of the three charge states whose existence has been proved for vacancy.

1. The F centre which is a neutral vacancy occupied by two electrons, acting as a shallow donor at about 0.05 eV from the valance band.
2. The F^{+} centre, which is a positively charged centre and forms a trap at about 0.3 eV below the conduction band.
3. F^{2+} centre, a doubly ionised centre at 0.8 eV – 2.0 eV below the conduction band.

The PL intensities of 540 nm for the ZnO films depend more on the stoichiometry of the films than on the textured grain size of the polycrystalline films [54]. The 540 nm emission is attributed to the oxygen vacancies [55].

1.5 p- Type Transparent Conductors

NiO thin film was the first reported p-TCO with a moderate 40% transparency in the visible region and a high 7.0 S cm^{1} room-temperature conductivity [56]. The bandgap of NiO single crystal is between 3.6 and 4.0 eV.[57]. Nickel vacancies as well as excess oxygen in interstitial sites are responsible for enhanced p-type conductivity of the material.[58]
The p type TCOs reported so far generally have less conductivity than that reported for n type TCOs. The large electronegativity of oxygen could be producing a strong localisation of the valance band edge of oxides thereby producing a deep trap where positive holes are localised [59]. These holes cannot migrate even under an applied field. Thus efforts should be made to modulate or modify the energy band structure to reduce the localisation of the valance band edge so as to increase the mobility of the holes. Cu_2O and Ag_2O show p type conductivity. However their low band gap (~ 2eV) make it impossible to use them as transparent conductors. Analysing the structure of these compounds show linear coordination of two oxygen ions to Cu^{+} ions

this could be an indication of the fact that the $3d^{10}$electrons of Cu^+ have comparable energy with O $2p^6$ electrons. This could be reducing the localization effects of the traps produced at the valance band edge. But the three dimensional interaction of Cu^+ ions should be expanding the band edge effectively reducing the band gap. Thus if the Cu^+ interactions could be reduced while the linear coordination with two oxygen atoms be retained in any crystal structure, this would produce p type transparent conductors.

Owing to the strong ionic nature of metal-oxygen bonding, holes are typically localized at the valence band edge, which is dominated by oxygen-2p levels therefore limiting p-type conduction. Two methods have been suggested to enhance the covalency between metal oxygen bonding, thereby limiting localization. Choosing cations having closed d-shells of energy comparable to that of the oxygen-2p levels (i.e., Cu^+, Ag^+, and Au^+, especially when found in linear coordination with oxygen [60]), and choosing a structure in which oxygen adopts tetrahedral coordination. An aggressive search for a viable p-type TCO was motivated by the report of Kawazoe et al. on the optical and electrical properties of copper aluminate ($CuAlO_2$) thin films prepared by laser ablation. $CuAlO_2$, which crystallizes in the delafossite structure having the general formula $A^{1+}B^{3+}O^{2-}$ show p-type conduction. The delafossite structure comprises of alternating layers of slightly distorted edge-shared BO_6 octahedral and two-dimensional close-packed A-cation planes forming linear $O–A^{1+}–O$ "dumbbells" [61] as found in the well-known p-type oxide semiconductor Cu_2O[62]. The delafossite structure is shown in figure 1.4. Furthermore, the oxygen atoms are coordinated by four cations (one A^{+1} and three B^{3+}). Depending on the stacking of the layers, two polytypes are possible.

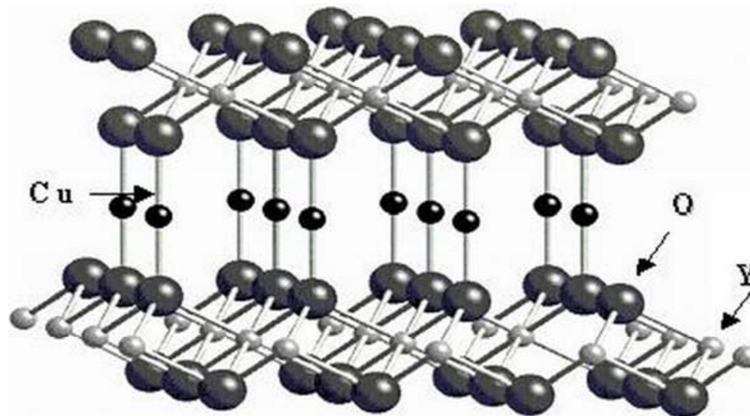

Figure 1.4 Delafossite structure

The “3R” polytype consists of “AaBbCcAaBbCc...” stacking along the *c*-axis and has rhombohedral symmetry with the space group $R\overline{3}m$ (No. 166), whereas the “2H” polytype consists of an alternate stacking sequence (“AaBbAaBb...”) and has the space group *P*63/*mmc* (No. 194) [63].

$CuYO_2$ is p-type semiconductor having wide bandgap isostructural with $CuAO_2$ delafossite (where A= Fe, Co, Rh, Ga,Sc,Y or lanthanides) [64]. Intercalation with oxygen to form $CuAO_{2+\delta}$ phases is possible for compounds with large A^{3+} cations. Cava et al [65,66] have investigated the properties of polycrystalline $CuYO_{2+\delta}$ and $CuLaO_{2+\delta}$ phases. The $CuYO_{2+\delta}$ doped with calcium show conductivity as high as 10 Scm^{-1} after the oxygen intercalation. Similar observation of increase in conductivity has been reported for $CuScMgO_{2+\delta}$ films on oxygen intercalation [67]. But the oxygen intercalation results in reduced transmittance in these films.

$CuAlO_2$ was the first prepared in the thin film form by Kawazoe [2]. Many materials including $CuGaO_2$, $CuInO_2$, $CuYO_2$, were also prepared in the bulk form all these materials show low conductivity (< 10^{-1} S cm^{-1}) and have low transmittance in the visible range. (≈ 50%). Doped copper delafossites like $CuGaO_2$:Fe, $CuInO_2$:Ca, $CuYO_2$:Ca, $CuFe_{1-x}V_xO_2$, $CuCo_{1-x}Sb_xO_2$, $CuMn_{1-x-}Sb_xO_2$ etc also show low conductivity and transmittance. The $CuNi_{1-x-}$

Sb_xO_2:Sn delafossite thin films with were obtained reasonable conductivity of 5 x 10^{-2} S cm^{-1} and transmittance of 60% in the visible range [68]

Silver based delafossites are difficult to synthesis by solid state reactions. They are not as stable as the Cu based delafossites. Thin films of $AgInO_2$ showed n type conductivity. Magnesium doping in bulk $AgInO_2$ leads to p type conduction. Very low conductivity is observed for these powders. The other silver based delafossites reported are also low conducting. They include $AgCrO_2$, $AgScO_2$, and $AgGaO_2$. p type conductivity of 2 x 10^{-1} S cm^{-1} and transparency of 50% in the visible is obtained for thin films of $AgCoO_2$ [68].

The cause of p type conductivity in these materials is due to excess oxygen (or metal deficit) in the crystallite sites. Changing the preparation conditions of the materials result in deviation of composition from stoichiometry in these materials. Thin film preparation of silver based delafossite compounds is a challenging task due to the instability of the silver compounds.

The Cu – 3d character of the valance band edge of the copper based delafossite have an edge over the O – 2p character of the valance band edge of silver based delafossites. Since the d mainfold holes are more mobile than the p mainfold holes [69].

The origin of p type conductivity in zinc oxide has been controversial. From a first principles calculation, Yamamoto and Yoshida [70] proposed that ‘‘co-doping’’ of donor acceptor dopants (e.g. Ga and N, respectively) in ZnO might lead to p-type conduction. In this method the simultaneous doping of both acceptor (N) and donor (Ga) into the ZnO lattice were carried out with an acceptor concentration twice that of the donor concentration to get a maximum conductivity in p-ZnO. The essential approach of this method is to stabilize the N substitution in the appropriate ZnO lattice sites by the formation of N–Ga–N type bonds, which reduce the N–N repulsive interaction (Madelung Energy) thereby making the acceptor level shallower, thus enhancing the acceptor doping. Successful p type doping of ZnO was first demonstrated by Joseph et al. [71] with a room temperature resistivity

of 0.5 Ω cm and a carrier concentration of 5 x 10^{19} cm^3 in p-type ZnO thin films deposited on glass substrate with Ga and N as dopants.

Thin films grown by spray pyrolysis of nitrogen doped p type ZnO have a carrier concentration of 10^{18} cm^3 and resistivity of 10^{-2} Ω cm [72]. The low density of compensative native defects as well as the hydrogen passivation in the ZnO:N film grown by ultrasonic spray pyrolysis (USP) probably account for the good p type conduction. The high hole mobility may be due to the nanocrystal structure of ZnO based films grown by ultrasonic spray pyrolysis. The photoluminescence spectrum exhibits a strong near-band-edge emission and a very weak deep-level emission in both undoped and N-doped ZnO films, indicating that the ZnO-based films grown by the USP technique are very close to stoichiometry and of optically high quality.

p-type conductivity of intrinsic ZnO thin films deposited by plasma-assisted metal-organic chemical vapor deposition with a hole concentration above 10^{17} cm^{-3} was achieved at the growth temperatures of 250 and 300 °C. It is speculated that the oxygen chemical potential is enhanced by virtue of oxygen plasma, which can lower the formation energy of some acceptor defect, such as zinc vacancy, and this accounts for the p-type conductivity. Increasing the growth temperature to 350 and 400 °C results in n-type conductivity with an electron concentration around 10^{17} cm^{-3}. The inversion to n-type conductivity can be explained as the compensation effect by the ionized oxygen vacancy donor, which is readily formed at a high growth temperatures. The *p*-type behavior is temperature dependent. The origin of intrinsic p-type behavior has been ascribed to the formation of zinc vacancy and some complex acceptor center. Understanding of these intrinsic acceptor states will help elucidate the extrinsic as well as intrinsic p-type doping mechanism in ZnO [73]. The films grown at optimum conditions show a resistivity of 12.7 Ω cm and a hole concentration of 1.88 x 10^{17} cm^{-3}.

Arsenic doped ZnO thin flms show p type conductivity. ZnO: As films grown on O – face of ZnO substrates and Si – face of SiC show p type conductivity with a carrier concentrationof 9 x 10^{16} cm^{-3} and mobility of 6 cm^2/Vs. is obtained with resistivity of 12 Ω cm for thin films. The PL emission at 3.359 eV is attributed to acceptor bound exciton emission and the PL emission at 3.322 eV and 3.273 eV is attributed to recombination

emissions between free electrons and acceptor holes. The donor to acceptor recombinations result in PL emissions at 3.219 eV and 3.172 eV. [74].

p-type conduction in ZnO thin films has also been realized by Al–N co-doping method. ZnO:Al,N thin films were prepared in NH_3–O_2 atmosphere with the substrate temperature in the range of 360–600 ^{O}C. The conduction type of Al–N co-doped ZnO thin films are dependant greatly on the growth temperature. Room temperature resistivity of 24.5 Ω cm and a hole concentration of 7.48 x 10^{17} cm^3 with a Hall mobility of 0.341 cm^2 / V s in ZnO thin films on sapphire substrate. The substrate temperature exerts a remarkable influence on the structural characteristics this is because that the substrate temperature restricts diffusion behaviour of nucleation particle on substrate surface. According to the nucleation theory, for a perfect heteroepitaxy nucleation, it is necessary to satisfy surface diffusion condition, the substrate temperature must be higher than a critical value. Below this value, the sputtering molecules or atoms with higher energy can also be ''cooled'' quickly, their surface diffusion length is greatly reduced, and they cannot migrate to nucleation position. The surface of the film obtained under the critical temperature would be rough and with polycrystal or amorphous structure. When the growth temperature is too high, the absorption life of ZnO molecule will be shortened, and the decomposition of ZnO molecule is faster than the combination of Zn and O, even under high partial pressure of O_2. This will introduce local Zn-rich region and result in a large number of point defect (V_o or Zn_o), even leading to amorphous state in the ZnO film [75].

The development of p type transparent oxide materials has lead to the fabrication of all oxide diodes and transistors. The progress achieved in the field of semiconductor oxide diodes and transistors has paved way for newer applications for transparent conductors and a new field of electronics called Transparent Electronics has been defined.

The realization of a transistor is of great importance in the context of transparent electronics since the control electrode of such a device facilitates the achievement of logic, amplification, memory, and other types of signal conditioning and processing functions which, within the context of microelectronics, play an important role in our modern information society.

The conventional thin film transistors developed with opaque elements or polymers have a drawback that their control electrodes are opaque. Thus from the point of view of transparent electronics, one challenge facing polymer light emitting devices centres around the thin-film transistor (TFT) array control circuitry. While needed for maximized brightness and efficiency, the opaque TFTs restrict the amount of light that can be transmitted to the observer. OLEDs and PLEDs lack the intrinsic property of bistable emission, therefore they must be driven by higher voltages and currents for suitable brightness in a passive matrix addressing scheme. The light emitting pixels may be controlled by a thin-film transistor array for much better brightness and efficiency. Unfortunately, the current opaque TFTs severely restrict the amount of light detected by the observer. Depending upon the design of the array and interconnects, typically only a fraction of the emitted light is used by the observer for the information. A large portion of the energy of the display is lost. One method to increase the efficiency is to combine the recent progress in transparent oxides that are semiconducting to near-metallic with the PLEDs. ZnO is one of a few oxides that can be grown as a crystalline material at relatively low deposition temperatures on various substrates such as amorphous glasses and plastics. By using these characteristics it is possible to realize thin film transistors by using ZnO as the active channel layer. It is expected that the characteristics of ZnO–TFT's will not degrade on exposure to visible light, due to the wide band gap of its active channel layer, whereas the characteristics of amorphous Si TFTs and poly-Si TFTs do degrade. Therefore, there is no need to shield the active channel layer from visible light in TFT's when ZnO is used as the active channel. This makes the TFT structurally simple and transparent to visible light, which would allow the aperture ratio of active matrix arrays to be increased. [76] ZnO is a material with excellent properties for developing transparent electronic devices.

1.6 Conclusion

In general, the traditional groups of materials used to build transparent conducting oxides include SnO_2, In_2O_3, ZnO (doped with F or Al), and CdO. However indium oxides are volatile, cadmium is poisonous. Several binary oxides are unstable, CdO converts to $Cd(OH)_2$, In_2O_3 converts to $In(OH)_3$ at less than 150^oC, SnO_2 absorbs water. Only zinc oxide can be doped to form either p type or n type material. The p type TCO's of delafossite structure are generally less transparent (hardly 50% at 500nm) than ZnO. Thus useful devices can be fabricated only using ZnO thin films that show better than 80% transmittance over the entire visible spectrum. It would be sensible to work towards understanding the basic growth mechanisms and reasons for p type conduction in ZnO or for the methods to increase transmittance in delafossite structure materials. Thus on the point of the consideration of cost, toxicity or environmental considerations and applications zinc oxide far surpasses competition from any other material under current research interest.

1.7 References

[1.] K. Badeker, Ann. Phys. **22** (1907) 749

[2.] H. Kawazoe, M. Yasukawa, H. Hyodo, M. Kurita, H. Yanagi and H. Hosono, Nature ***389*** (1997) 939

[3.] R.L.Hoffman, B.J.Norris and J.F.Wager, Appl. Phy.Lett **82** (2003) 733

[4.] P.P. Edwards, A. Porch, M.O. Jones, D.V. Morgan and R.M. Perks, Dalton Trans. (2004) 2995

[5.] H. Ohta and H. Hosono, Materials Today **7** (2004) 42

[6.] D. J. Griffits, Introduction to Electrodynamics, Prentice – Hall of India, New Delhi, (1994)

[7.] I. Hamberg and C.G. Granqvist, J. Appl. Phys. **60** (1986) R123

[8.] J. Hu and R. G. Gordon, J Appl. Phys. **71** (1992) 880

[9.] I. Hamberg, A. Hjortsberg, and C. G. Granqvist, Appl. Phys. Lett. **40** (1982) 362

[10.] R. G. Gordon, Proc. Of MRS workshop "Transparent conducting oxides (TCOs)" August (2000) 5

[11.] K. L. Chopra, S. Major and D. K. Pandya, Thin Solid Films **102** (1983) 1

[12.] E. Shanthi, V. Dutta, A. Banerjee, and K. L. Chopra, J. Appl. Phys. **51** (1980) 6243

[13.] A .De and S. Ray, J. Phys. D: Appl.Phys. **24** (1991) 719

[14.] H.L. Hartnagel, A.L. Dawar, A.K.Jain and C. Jagadish, Semiconducting transparent thin films, IOP publishers (1995)

[15.] J. Bardeen and W. Shockley, Phys. Rev. **80** (1950) 72

[16.] A. R. Huston, J. Appl. Phys. **32** (1961) 2287

[17.] H. Ehrenreich, J. Appl. Phys. **32** (1961) 2155

[18.] C. Erginsoy, Phys. Rev. **79** (1950) 1013

[19.] V. A. Johnson, and K. Lark–Horovitz, Phys. Rev. **71** (1947) 374

[20.] J. Appel, Phys. Rev. **122** (1961) 1760

[21.] R. L Petritz, Phys. Rev. **104** (1956) 1508

[22.] T. J.Coutts, D. L. Young and L. Xiaonan, MRS Bull. **8** (2000) 58

[23.] D. B. Fraser and H. D. Cook, J. Electrochem. Soc. **119**, (1972) 1368

[24.] G. Haacke, Appl. Phys. **47**, (1976) 4086
[25.] P. A. Iles and S. I. Soclof, I. E. E. Photovoltaic Specialists Conference, (1976) 978
[26.] Ti X. Li, T. Gessert, C. DeHart, T. Barnes, H. Moutinho, Y. Yan, D. Young, M. Young, J. Perkins, and T. Coutts, **NREL/CP-520-31017** (2001)
[27.] R. L. Hoffmann, Master of Sciences Thesis, Oregon State University (1992)
[28.] B.J. Ingram, G.B. Gonzalez, D.R. Kammler, M.I. Bertoni and T.O. Mason, Journal of Electroceramics, **13**, (2004) 167
[29.] P.P. Edwards, A. Porch, M. O. Jones, D. V. Morgan, and R. M. Perks, Dalton transactions B408864F (2004)
[30.] M. Chen, Z.L. Pei, X. Wang, Y. H. Yu, X.H. Liu, C. Sun and L. S. Wen, J. Phys D **33,** (2000) 2538
[31.] U. Rossler, Phys. Rev. **184** (1969) 733
[32.] C. Tonon, C. Duvignacq, G. Teyssedre and Magdeleine, J.Phys. D: Appl Phys. **34** (2001) 124
[33.] M. Purica, E. Budianu and E. Rusu, Thin solid films **383** (2001) 284
[34.] J.Kioke, K. Shimoe, H. Ieki, Jpn. J.Appl.Phys. **32**. (1993) 2337
[35.] M. Penza, C. Martucci, V. I. Anisimkin, and L. Vasanelli, Materials science fourm **203** (1996) 137
[36.] P. Sharma A. Gupta, K. V. Rao, F. J. Owens, R. Sharma, R. Ahuja, J. M. O. Guillen, B. Johansson and G. A. Gehring Nature mater. **2**. (2003) 673.
[37.] A. Bui, H. T. Nguyen and A. Loubiere J. Phys. D: Appl Phys. **28** (1995) 774.
[38.] R. K. Theraja, A. Mitra, Appl. Phys. B **71** (2000) 181
[39.] D. M. Bagnall, Y. F. Chen, Z. Zhu, T. Yao, S. Koyama, M.Y. Shen, T. Goto, Appl. Phys. Lett. **70** (1997) 230.
[40.] H. Cao, J. Y. Wu, H. C. Ong, J. Y. Dai, and R. P. H. Chang, Appl. Phys. Lett., **73** (1998) 3
[41.] Wang R, King L H and Sleight A W J Mater. Res. **11** (1996) 1659.

[42.] J. H. Morgan and D. E. Brodie, Can. J. Phys. **60,** (1982) 1387.
[43.] J. Lu, Z. Ye, J. Huang, L. Wang, and B. Zhao, Appl. Sur. Sci. **207**, (2003) 295.
[44.] P. Nunes, E. Fortunato, R. Martins, Thin Solid Films **383** (2001) 277.
[45.] K. K. Kim, H. S. Kim, D. K. Hwang, J. H. Lim, S. J. Park, Appl. Phys. Lett **83**, (2003) 63.
[46.] S. J. Henley, M. N. R. Ashfold, D. Cherns, Surface and Coatings Technology **177–178**, (2004) 271
[47.] Y. Ohya, H. Saiki and Y. Takahashi, J. Mater. Sci. **29** (1994) 4099
[48.] P. Nunes, B. Fernandes, E. Fortunato, P. Vilarinho, R. Martins, Thin Solid Films **337** (1999) 176
[49.] Y. Sato and S. Sato, Thin Solid Films **281–282** (1996) 445
[50.] J. H. Morgan and D.E. Brodie, Can. J. Phys. **60** (1982) 1387.
[51.] S. Hayamizu, H. Tabata, H. Tanaka, and T.Kawai J. Appl. Phys. **80** (1996) 787
[52.] S. V. Prasad, S. D. Walck, J.S. Zabinski, Thin solid Films **360** (2000) 107
[53.] C. Tonon, C. Duvignacq, G. Teyssedre and Magdeleine, J.Phys. D: Appl Phys. **34** (2001) 124
[54.] S.H. Bae, S. Y. Lee, B.J. Jin, S. Im Appl. Sur. Sci. **169–170**, (2001) 525
[55.] K. Vanheusden, C.H. Seager, W. L. Warren, D. R. Tallant, J. A. Voigt, Appl. Phys. Lett. **68**, (1996) 403.
[56.] H.Sato, T.Minami, S.Takata, T.Yamada, Thin Solid Films **236** (1993) 27
[57.] D. Adler, J. Feinleib, Phys. Rev. B **2** (1970) 3112.
[58.] E. Antolini, J. Mater. Sci. **27** (1992) 3335.
[59.] Hiroshi Yanagi, Transparent p/n type oxide semiconductors with delafossite structure: Chemical design and material exploration. Thesis (2001).
[60.] H. Kawazoe, M. Yasukawa, H. Hyodo, M. Kurita, H. Yanagi and H. Hosono, Nature ***389*** (1997) 939

[61.] Hiroshi Kawazoe, Hiroshi Yanagi,Kazushige Ueda, and Hideo Hosono MRS Bulletin (2000) 28
[62.] L. Kleinman, And K. Mednick, Phys. Rev. B **21,** (1980) 1549
[63.] K. Ueda, S. Inoue, H. Hosono, N. Sarukura and M. Hirano. Appl. Phys. Lett. **78** (2001) 2333.
[64.] R. D. Shannon, D. B. Rogers, and C.T. Prewitt, Inorg Chem **10** (1971) 713.
[65.] R. J. Cava, H. W. Zandbergen, A. P. Ramierz, H. Takagi, C. T. Chen, J. J. Krajewski, W. F. Peck.jr, J. V. Waszczak, G. Meigs, R. S. Roth, and L. F. Schneemeyer, J. Solid state chem. **104** (1993) 437.
[66.] R. J. Cava, W. F. Peck.jr, J. J. Krajewski, S. W. Chenog, and H. Y. Hwang, J. Mater Res **9** (1994) 314.
[67.] H. Yanagi, S. Park, A. D. Draeseke, D. A. Keszler and J.Tate, J. Solid state chem **175** (2003) 34.
[68.] J. Tate, M. K. Jayaraj, A. D. Draeseke, T. Ulbrich, A. W. Sleight, K. A. Vanaja, R. Nagarajan, J. F. Wager, R. L. Hoffman, Thin solid films, **411** (2002) 119.
[69.] A.N. Banerjee, K. K. Chattopadhyay, Progress in Crystal Growth and Characterisation of materials. **50** (2005) 52
[70.] T. Yamamoto, H.K. Yoshida, Jpn. J. Appl. Phys. 38 (1999) L166.
[71.] M. Joseph, H. Tabata, T. Kawai, Jpn. J. Appl. Phys. **38** (1999) L1205.
[72.] Jun-Liang Zhao, Xiao-Min Li, Ji-Ming Bian, Wei-Dong Yu, Can-Yun Zhang, Journal of Crystal Growth **280** (2005) 495.
[73.] Y. J. Zeng, Z. Z. Ye, W. Z. Xu, J. G. Lu, H. P. He, L. P. Zhu, B. H. Zhao, Y. Che and S. B. Zhang Applied Physics Letters **88**, (2006) 262103
[74.] Y.R.Ryu, T.S.Lee and H.W.White, Appl. Phys. Lett. **83** (2003) 87.
[75.] Guodong Yuan, Zhizhen Ye, Qing Qian, Liping Zhu, Jingyun Huang,Binghui Zhao, Journal of Crystal Growth **273** (2005) 451
[76.] Satoshi Masuda, Ken Kitamura, Yoshihiro Okumura, Shigehiro Miyatake, Hitoshi Tabata and Tomoji Kawai, J. Appl. Phys. **93** (2003) 1624

Chapter 2

Thin Film Deposition Techniques And Characterisation Tools

This chapter describes the various thin film deposition techniques employed for the growth of the thin films and the various characterisation methods used in the present investigation.

2.1 Introduction

Any solid or liquid object with one of its dimensions very much less than that of the other two may be called a 'thin film' [1]. Thin film devices would typically be about 5 to 50 μm thick in contrast to bulk devices, which are about 50 to 250 μm thick [2]. If the growth is atom by atom or molecule by molecule it is called thin film and if the growth is grain by grain it is thick film. The thickness is not as important in defining a film as the way it is created with the consequential effects on its microstructure and properties. For example the microstructural features of the absorber layer sensitively influence the photovoltaic performance in a solar cell and in some cases, specific microstructures may be necessary to obtain the desired performance. A wide variety of microstructures and consequently properties can be obtained by simply varying the deposition conditions during the growth of the film. Thin film properties are strongly dependent on the methods of deposition, the substrate materials, the substrate temperature, the rate of deposition and the background pressure. The application and the properties of the given material determine the most suitable technique for the preparation of thin films of that material.

The thin films prepared for the studies presented in this thesis were mainly deposited using radio frequency (rf) magnetron sputtering and pulsed laser deposition techniques. Radio frequency magnetron sputtering technique was employed for the deposition of calcium doped copper yttrium oxide, pure zinc oxide and aluminum doped zinc oxide thin films while pulsed laser deposition technique was used to deposit aluminum and gallium doped zinc oxide thin films. Vacuum evaporation technique was used to deposit metal electrodes (aluminum, copper or silver) for electrical characterisation. The structural, optical and electrical properties of these films were studied using different characterisation tools.

2.2 Thin film Preparation Techniques

Generally any thin film deposition follows the sequential steps: a source material is converted into the vapour form (atomic/molecular/ionic species) from the condensed phase (solid or liquid), which is transported to the substrate and then it is allowed to condense on the substrate surface to form the solid film [2]. Depending on how the atoms/molecules/ions/clusters of species are created for the condensation process, the deposition techniques are broadly classified into two categories, viz. physical methods and chemical methods.

Chemical bath deposition, chemical vapour deposition, and spray pyrolysis are examples of chemical method of thin film deposition. Thermal evaporation, e beam evaporation, rf and dc sputtering and pulsed laser deposition (PLD) are examples of physical methods of thin film preparation.

The following sections discuss the methodology and experimental set-up used in various thin film deposition techniques.

2.2.1 Thermal evaporation by resistive heating

Thermal evaporation is the most widely used technique for the preparation of thin films of metals, alloys, and also many compounds, as it is very simple and convenient. Here the only requirement is to have a vacuum environment in which sufficient amount of heat is given to the evaporants to attain the vapour pressure necessary for the evaporation. The evaporated material is allowed to condense on a substrate kept at a suitable temperature.

When evaporation is made in vacuum, the evaporation temperature will be considerably lowered and the formation of the oxides and incorporation of impurities in the growing layer will be reduced. Evaporation is normally done at a pressure of 10^{-5} Torr. At this pressure a straight line path for most of the emitted vapour atoms is ensured for a substrate to source distance of

nearly 10 to 50 cm [3]. The characteristics and quality of the deposited film will depend on the substrate temperature, rate of deposition, ambient pressure, etc. and the uniformity of the film depends on the geometry of the evaporation source and its distance from the source. The deposition by thermal evaporation is simple, convenient and is widely used. Excellent and detailed reviews on the know-how of the thermal evaporation have been discussed by Holland [4].

2.2.2 Electron beam evaporation

In electron beam evaporation (EBE) a stream of electrons is accelerated through fields of typically 5–10kV and focussed onto the surface of the material for evaporation. The electrons lose their energy very rapidly upon striking the surface and the material melts at the surface and evaporates. That is, the surface is directly heated by impinging electrons, in contrast to conventional heating modes. Direct heating allows the evaporation of materials from water-cooled crucibles. Such water-cooled crucibles are necessary for evaporating reactive and in particular reactive refractory materials to avoid almost completely the reactions with crucible walls. This allows the preparation of high purity films because crucible materials or their reaction products are practically excluded from evaporation [4,5].

Electron beam guns can be classified into thermionic and plasma electron categories. In the former type the electrons are generated thermionically from heated refractory metal filaments, rods or disks. In the latter type, the electron beams are extracted from plasma confined in a small space.

The copper electrodes for the electrical characterisation of the ZnO:Al thin films were evaporated using a 3kW electron beam source (Hind High Vacuum, Bangalore) and a six-inch diameter diffusion pump backed by a rotary pump (make – Indian High vacuum Pumps, Bangalore).

2.2.3 Sputtering

Sputtering is one of the most versatile techniques used for the deposition of transparent conductors when device quality films are required. Sputtering process produces films with better controlled composition, provides films with greater adhesion and homogeneity and permits better control of film thickness. The sputtering process involves the creation of gas plasma usually an inert gas such as argon [6] by applying voltage between a cathode and anode. The target holder is used as cathode and the anode is the substrate holder. Source material is subjected to intense bombardment by ions. By momentum transfer, particles are ejected from the surface of the cathode and they diffuse away from it, depositing a thin film onto a substrate. Sputtering is normally performed at a pressure of 10^{-2} –10^{-3} Torr.

Normally there are two modes of powering the sputtering system; dc and rf biasing. In dc sputtering system a direct voltage is applied between the cathode and the anode. This method is restricted for conducting materials only. rf sputtering is suitable for both conducting and non-conducting materials; a high frequency generator (13.56 MHz) is connected between the electrodes of the system. Magnetron sputtering is a process in which the sputtering source uses, magnetic field at the sputtering target surface. Magnetron sputtering is particularly useful when high deposition rates and low substrate temperatures are required [7].

Both reactive and non-reactive forms of dc, rf and magnetron sputtering have been employed for the deposition of compound semiconductors. In reactive sputtering, the reactive gas is introduced into the sputtering chamber along with argon to deposit thin films. For example to deposit metal oxide thin films pure metal target is sputtered in a mixture of argon and oxygen atmosphere. The deposition rates and properties of the films strongly depend on the sputtering conditions such as the partial pressure of the reactive gas, the sputtering pressure, substrate temperature and substrate to target spacing.

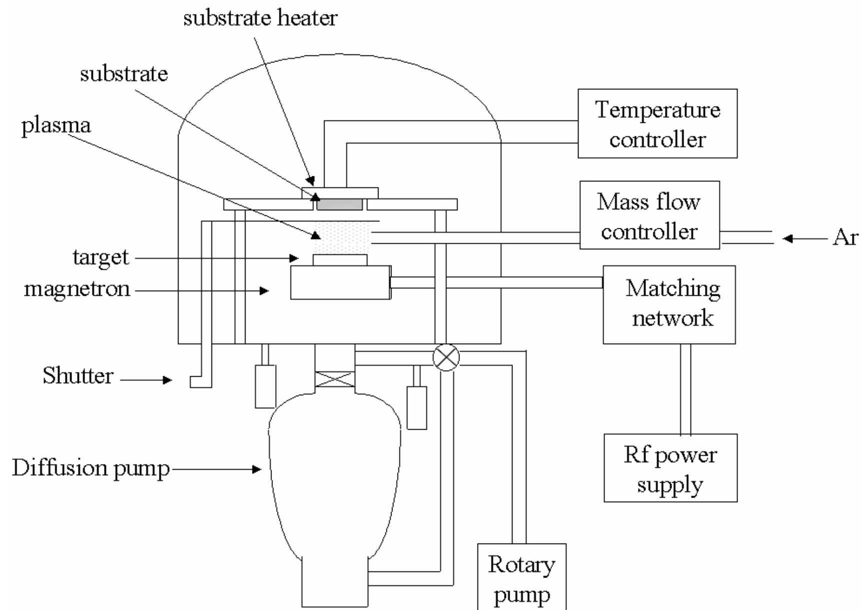

Figure 2.1 RF Sputter Deposition System

The process of rf sputter deposition is made possible due to the large difference in mass, and hence mobility, of electrons and inert gas ions. Because electrons are many times less massive than ions, electrons attain much greater velocities and travel much further than ions during each cycle of the applied rf voltage waveform. Since electrons travel much further, they eventually accumulate on the target, substrate and chamber walls such that the plasma is the most positive potential in the system. These induced negative voltages or "sheath voltages", cause acceleration of positive ions toward the negatively charged surfaces, which subsequently leads to sputtering events. The volume adjacent to a surface tends to be relatively free of electrons because of the negatively charged surface. This leads to a "dark space" because electrons are not available to excite gas atoms [8]. A schematic diagram of the rf sputtering system is shown in figure 2.1. The target is selectively sputtered by controlling the relative surface areas of the

target and the substrate holder. If space charge limited current is assumed, the ion current flux, J can be estimated by the Child- Langmuir equation [8],

$$J = \frac{KV^{3/2}}{D^2 m_{ion}} \quad (2.1)$$

Where D is the dark space thickness, V is the sheath voltage, m_{ion} is the ionic mass and K is the proportionality constant. Since the positive ion current must be equal at both the electrodes,

$$\frac{A_A V_A}{D_A^2} = \frac{A_B V_B}{D_B^2} \quad (2.2)$$

Where A_A and A_B are the surface areas of electrodes A and B respectively. It should be noted that this step differs from the assumption of treating the positive ion current densities equal. If the positive ion current densities were equal, there would be a much greater positive ion current flowing during one half cycle of the applied voltage waveform than the other due to the much greater area of the grounded substrate electrode. Therefore, because this system is assumed to be in steady state, the total positive ion current per half cycle should be the relevant quantity.

The glow discharge itself is a region where large quantities of positive and negative charge exist and can be modelled as a wire. Since most of the voltage in the glow discharge is dropped across the dark space, and they have small conductivities, they can be modelled as capacitors such that the capacitances,

$$C \propto A/D \quad (2.3)$$

Furthermore, an ac voltage will divide across two series capacitors such that,

$$\frac{V_A}{V_B} = \frac{C_B}{C_A} \tag{2.4}$$

From equations (2.1), (2.2) and (2.3),

$$\frac{V_A}{V_B} = \left(\frac{A_B}{A_A}\right)^2 \tag{2.5}$$

This equation tells that smaller area will see larger sheath voltage, whereas larger area will see a smaller sheath voltage by a power of 2. The usefulness of this result is that $A_B > A_A$ must hold to selectively sputter the target. This is done in practice by grounding the substrate holder to the entire chamber resulting in a very large A_B. For this reason it is extremely important that the substrate holder and the system are well grounded to ensure that resputtering of the growing film does not occur.

Sputtering yield is defined as the quantity of the material sputtered per ion (atoms/ion or grams/ion) [9]. To measure the sputtering yield accurately, we need to measure three experimental parameters namely the crater volume (cm^3) formed by sputtering, the ion current (A) and the sputtering time (sec). Main features observed for the sputtering techniques are:

- ⇒ Sputtering yield is different for different elements. Sputtering yield increases as the reciprocal of the binding energy of the surface atoms.
- ⇒ Sputtering yield decreases as the surface damage increases i.e. the sputtering yield of rough surface is lower than that of smooth surface.
- ⇒ As the mass of the sputtering species increases, the sputtering yield increases.
- ⇒ Light mass ions penetrate deeper into the target than heavier mass ions.

- ⇒ As sputtering energy increases, the sputtering yield increases up to 10 –100 keV. At higher energies, the sputtering yield again decreases since the ions penetrate into the target.
- ⇒ Since smaller particles penetrate further into the target, the energy when the yield starts to decrease is lower for lighter particles.
- ⇒ For multicomponent samples, the lightweight particle is usually preferentially sputtered if the binding energies of the components are similar. The sputtering rate of each component increases as the reciprocal of the binding energy and mass of that component.
- ⇒ Sputtering of oxide targets result in preferential depletion of oxygen.
- ⇒ Sputtering yield of metal oxide is less than the sputtering yield of corresponding metals.
- ⇒ For oxide samples, sputtering in an oxygen rich environment decreases the sputtering yield; the sputtering yield does not vary in other environments (e.g. CO, N_2) indicating that adsorption without chemical bonding is not enough to reduce the sputtering yield.

An in-house made magnetron has been used for the rf sputtering of calcium doped copper yttrium oxide, aluminium doped ZnO and ZnO thin films. A magnet of 2000 gauss was used to deflect the ions. A schematic diagram of the magnetron is shown in figure 2.2. The vacuum system consists of a six-inch diameter diffusion pump backed by a rotary pump (make – Indovision, Bangalore). The rf supply was connected to the magnetron through a capacitive matching network (make–Digilog Instruments, Bangalore). The flow of argon gas into the vacuum chamber was controlled using a mass flow controller (make Bronkhorst, Holland).

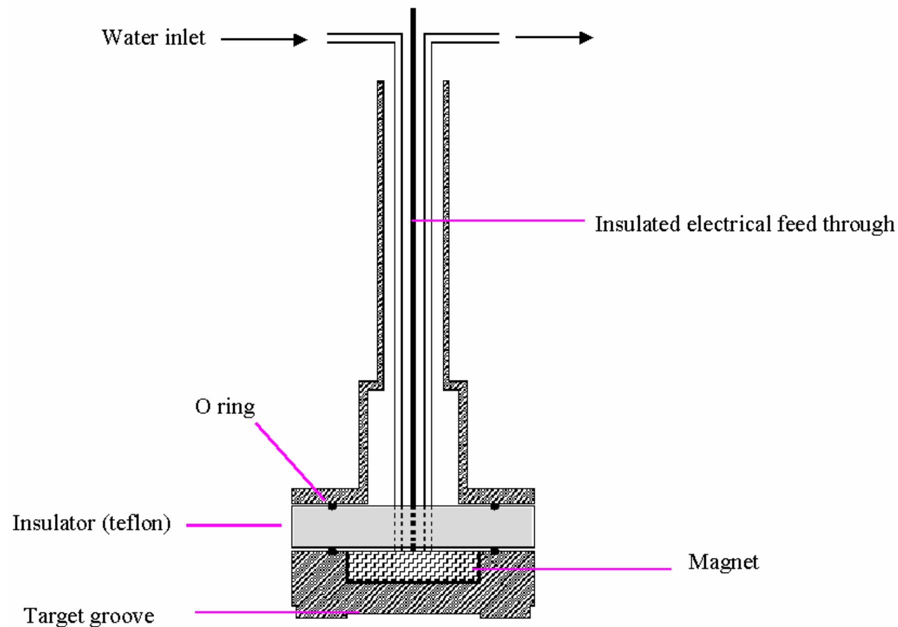

Figure 2.2 Schematic structure of the magnetron

2.2.4 Pulsed Laser Deposition

Pulsed laser deposition (PLD) is clearly emerging as one of the premier thin film deposition technologies. PLD has gained a great deal of attention in the past few years for its ease of use and success in depositing materials of complex stoichiometry. PLD was the first technique used to successfully deposit a superconducting $YBa_2Cu_3O_{7-d}$ thin film. Since that time, many materials that are normally difficult to deposit by other methods, especially multi-element oxides, have been successfully deposited by PLD. In the case of multielemental compounds such as high temperature superconductors, ferroelectrics and for electro optic materials, this technique is extremely successful. This technique offers many potential applications, from integrated circuits and optoelectronics to micro mechanics and medical implants [10]

The laser is a source of energy in the form of monochromatic and coherent photons, enjoying ever increasing popularity in diverse and broad applications. In many areas such as metallurgy, medical technology and electronic industry, the laser has become an irreplaceable tool. In material science lasers also play a significant role either as a passive component for process monitoring or as an active tool by coupling its radiation energy to the material being processed, leading to various applications such as localized melting during optical pulling, laser annealing of semiconductors, surface cleaning by desorption and ablation, laser induced rapid quench to improve surface hardening and most recently pulsed laser deposition for growing thin films [11]

The best quality films can be deposited by controlling the fundamental criteria of the substrate temperature (T), the relative and absolute arrival rates of atoms (R_i, Where i could vary from 1 to 6) and the energy of the depositing flux (E). PLD offers the best control over these criteria than other vacuum deposition techniques [11].

Figure 2.3 shows the schematic diagram of a pulsed laser deposition system. The main advantage of PLD derives from the laser material removal mechanism; PLD relies on a photon interaction to create an ejected plume of material from any target. The vapor (plume) is collected on a substrate placed at a short distance from the target. Though the actual physical processes of material removal are quite complex, one can consider the ejection of material to occur due to rapid explosion of the target surface due to superheating. Unlike thermal evaporation, which produces a vapor composition dependent on the vapor pressures of elements in the target material, the laser-induced expulsion produces a plume of material with stoichiometry similar to the target. It is generally easier to obtain the desired film stoichiometry for multi-element materials using PLD than with any other deposition techniques.

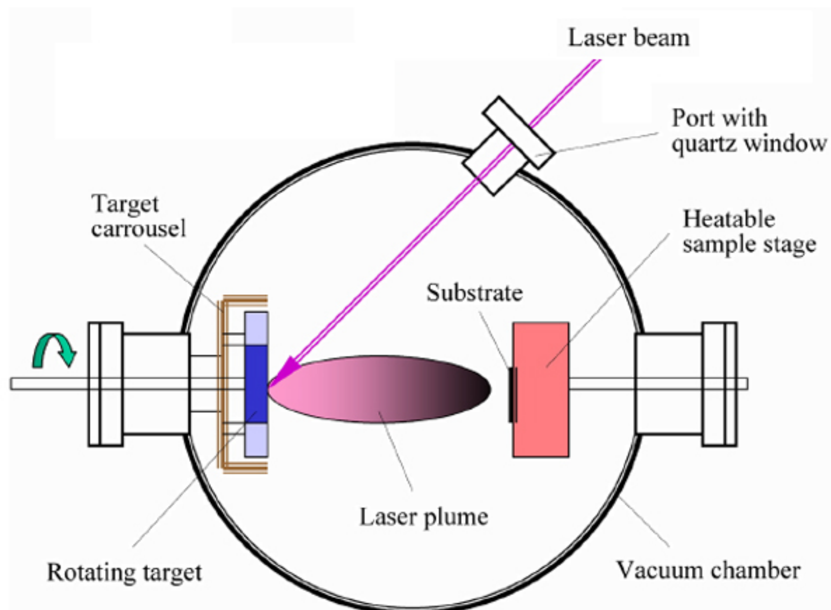

Figure 2.3 Schematic diagram of the pulsed laser deposition system.

Typical plasma temperature measured by emission spectroscopy during initial expansion is ≈ 10,000 K, which is well above the boiling point of most materials (≈ 3000 K). Heating of the plasma to these temperatures is thought to occur by inverse–Bremsstrahlung absorption of the laser light in a free – free transition of electron ion pair. This high temperature would evaporate the surface layer of the target thereby producing exact composition in the thin films.

The main advantages of pulsed laser deposition are:

- ***conceptually simple***: a laser beam vaporizes a target surface, producing a film with the same composition as the target.
- ***versatile***: many materials can be deposited in a wide variety of gases over a broad range of gas pressures.
- ***cost-effective***: one laser can serve many vacuum systems.
- ***fast***: high quality samples can be grown reliably in 10 or 15 minutes.
- ***scalable:*** as complex oxides move toward volume production.

i) ***Mechanisms of PLD***

The mechanism of pulsed laser deposition, in contrast to the simplicity of the set-up, is a very complex physical phenomenon. It not only involves the physical process of the laser-material interaction of the impact of high-power pulsed radiation on solid target, but also the formation plasma plume with high energetic species and even the transfer of the ablated material through the plasma plume onto the heated substrate surface. Thus the thin film formation process in PLD generally can be divided into the following four stages.

1. Laser radiation interaction with the target
2. Dynamics of the ablated materials.
3. Deposition of the ablation materials on the substrate.
4. Nucleation and growth of a thin film on the substrate surface

Each stage in PLD is critical to the formation of quality epitaxial, crystalline, stoichiometric and uniform thin film.

In the first stage, the laser beam is focused onto the surface of the target. At sufficiently high flux densities and short pulse duration, all elements in the target are rapidly heated up to their evaporation temperature. Materials are dissociated from the target surface and ablated out with stoichiometry as in the target. The instantaneous ablation rate is highly dependent on the fluences of the laser shining on the target. The ablation mechanisms involve many complex physical phenomena such as collisional, thermal, and electronic excitation, exfoliation and hydrodynamics.

During the second stage the emitted materials tend to move towards the substrate according to the laws of gas-dynamics and show the forward peaking phenomenon. The spatial thickness varies as a function of cos θ. The spot size of the laser and the plasma temperature has significant effects on the deposited film uniformity. The target-to-substrate distance is another parameter that governs the angular spread of the ablated materials. A mask placed close to the substrate could reduce the spreading.

The third stage is important to determine the quality of thin film. The ejected high-energy species impinge onto the substrate surface and may induce various type of damage to the substrate. These energetic species sputter some of the surface atoms and a collision region is formed between the incident flow and the sputtered atoms. Film grows after a thermalized region is formed. The region serves as a source for condensation of particles. When the condensation rate is higher than the rate of particles supplied by the sputtering, thermal equilibrium condition can be reached quickly and film grows on the substrate surface at the expenses of the direct flow of the ablation particles and the thermal equilibrium obtained.

The effect of increasing the energy of the adatoms has a similar effect of increasing substrate temperature on film growth [11]. Typical power densities involved in PLD are approximately 50 MW cm^{-2} for a reasonable growth rate. (> 1 A^o/shot) If plasma is formed during laser target interaction in vacuum or in air then an explicit laser – plasma interaction occurs. Due to which ions in the plasma are accelerated to as much as 100 – 1000 eV [11]. Nucleation-and-growth of crystalline films depends on many factors such as the density, energy, ionization degree, and the type of the condensing material, as well as the temperature and the physico-chemical properties of the substrate.The two main thermodynamic parameters for the growth mechanism are the substrate temperature T and the supersaturation D_m. They can be related by the following equation

$$D_m = kT \ln(R/R_e) \qquad (2.6)$$

where k is the Boltzmann constant, R is the actual deposition rate, and R_e is the equilibrium value at the temperature T.

The nucleation process depends on the interfacial energies between the three phases present - substrate, the condensing material and the vapour. The critical size of the nucleus depends on the driving force, i.e. the deposition rate and the substrate temperature. For the large nuclei, a characteristic of

small supersaturation, they create isolated patches (islands) of the film on the substrate, which subsequently grow and coalesce together. As the supersaturation increases, the critical nucleus shrinks until its height reaches on atomic diameter and its shape is that of a two-dimensional layer. For large supersaturation, the layer-by-layer nucleation will happen for incompletely wetted foreign substrates.

The crystalline film growth depends on the surface mobility of the adatom (vapour atoms). Normally, the adatom will diffuse through several atomic distances before sticking to a stable position within the newly formed film. The surface temperature of the substrate determines the adatom's surface diffusion ability. High temperature favours rapid and defect free crystal growth, whereas low temperature or large supersaturation crystal growth may be overwhelmed by energetic particle impingement, resulting in disordered or even amorphous structures.

The mean thickness (N_{99}) at which the growing thin and discontinuous film reaches continuity, is given by the formula

$$N_{99} = A(1/R)^{1/3} \exp(-1/T) \qquad (2.7)$$

where R is the deposition rate (supersaturation related) and T is the temperature of the substrate and A is a constant related to the materials[11]. In the PLD process, due to the short laser pulse duration (~10 ns) and hence the small temporal spread (<=10 ms) of the ablated materials, the deposition rate can be enormous (~10 nm/s). Consequently a layer-by-layer nucleation is favoured and ultra-thin and smooth film can be produced. In addition the rapid deposition of the energetic ablation species helps to raise the substrate surface temperature. In this respect PLD tends to demand a lower substrate temperature for crystalline film growth.

The films grown by pulsed laser deposition in the present studies were carried out in a vacuum chamber pumped by a six-inch diffusion pump backed by a rotary pump (Indovision, Bangalore). The laser used was the

second (532 nm) and third harmonics(355 nm) of Nd:YAG laser (Spectra Physics model GCR 150). The flow of oxygen into the chamber was controlled using a mass flow controller (Bronkhorst, Holland)

2.3 Characterisation tools

The optimisation of the preparation conditions is the main task in order to get device quality films. This has to be carried out on the basis of detailed structural, compositional, morphological, optical and electrical properties of the films obtained at different growth conditions. In the following sections the techniques used for the film characterizations are discussed briefly.

2.3.1 Thin film thickness

Thickness plays an important role in the film properties unlike a bulk material. Reproducible properties are achieved only when the film thickness and the deposition parameters are kept constant. Film thickness may be measured either by in-situ monitoring of the rate of deposition or after the film deposition. The thicknesses of the thin films prepared for the work presented in this thesis were measured either by optical interference method or by a stylus profiler (Dektak 6M).

i) ***Optical interference method***

Film thickness can be measured accurately from interference fringes using multiple beam interferometry. This technique was first used by Weiner [12] and later was modified by Tolansky [13]. Two reflecting surfaces are brought in close proximity such that a small wedge with a small air gap in between them is formed. If a monochromatic light falls at normal incidence on it, interference of light due to the multiple reflected beams results in a series of fringes (Fizeau). The distance between the fringes depends on the air gap as well as on the wavelength of the monochromatic light.

The film for thickness measurement is deposited on a flat surface so as to leave a sharp edge between the film and the uncoated region of the substrate. Over this film a highly reflecting coating of aluminium forms a sharp step on the film edge. Another optically flat glass slide known as the reference plate with a partially transparent aluminium film coated over it is then placed over the specimen with the metal coated surfaces in contact with each other so as to leave a small air gap at the step. A monochromatic parallel beam of light (λ) is then incident on this two plates assembly and reflected light is then observed through a microscope. A set of sharp fringes perpendicular to the step with equal displacements will be observed and the thickness (t) can be determined using the relation,

$$t = \frac{b\lambda}{2a} \tag{2.8}$$

where b is the displacement of the fringes at the step and a is the distance between consecutive fringes. The sharpness of the fringes depends on the reflectivity of the metal coating, the spread of the incident beam, air gap etc.

ii) ***Stylus Profiler***

The stylus profiler takes measurements electromechanically by moving the sample beneath a diamond tipped stylus (fig. 2.4). The high precision stage moves the sample according to a user defined scan length, speed and stylus force. The stylus is mechanically coupled to the core of a linear variable differential transformer (LVDT). As the stage the sample, the stylus moves over the sample surface. Surface variations cause the stylus to be translated vertically. Electrical signals corresponding to the stylus movement are produced as the core position of the LVDT changes. The LVDT scales an ac reference signal proportional to the position change, which in turn is conditioned and converted to a digital format through a high precision, integrating, analog-to-digital converter [14]. The film whose thickness has to be measured is deposited with a region masked this creates a step on the

sample surface the thickness of the sample can be measured accurately by measuring the vertical motion of the stylus over the step.

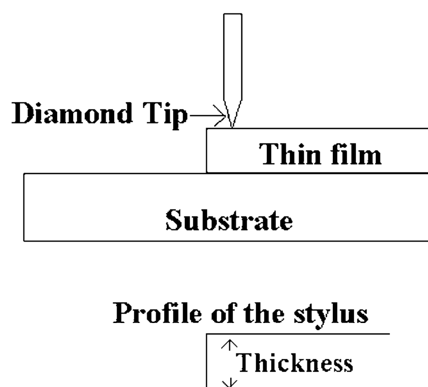

Figure 2.4. Schematic diagram illustrating the determination of thin film thickness with Stylus Profiler

2.3.2 X-ray diffraction studies

Electrical and optical properties of the thin films grown are influenced by the crystallographic nature of the films. X-ray diffraction (XRD) studies were carried out to study the crystallograoghic properties of the thin films prepared.
A given substance always produces a characteristic x-ray diffraction pattern whether that substance is present in the pure state or as one constituent of a mixture of substances. This fact is the basis for the diffraction method of chemical analysis. The particular advantage of x-ray diffraction analysis is that it discloses the presence of a substance and not in terms of its constituent chemical elements. Diffraction analysis is useful whenever it is necessary to know the state of chemical combination of the elements involved or the particular phase in which they are present. Compared with ordinary chemical analysis the diffraction method has the advantage that it is much faster, requires only very small sample and is non destructive [15].

The basic law involved in the diffraction method of structural analysis is the Bragg's law. When monochromatic x-rays impinge upon the atoms in a

crystal lattice, each atom acts as a source of scattering. The crystal lattice acts as series of parallel reflecting planes. The intensity of the reflected beam at certain angles will be maximum when the path difference between two reflected waves from two different planes is an integral multiple of λ. This condition is called Bragg's law and is given by the relation,

$$2dSin\theta = n\lambda \qquad (2.9)$$

where n is the order of diffraction, λ is the wavelength of the x-rays, d is the spacing between consecutive parallel planes and θ is the glancing angle (or the complement of the angle of incidence)[16].

X-ray diffraction studies gives a whole range of information about the crystal structure, orientation, average crystalline size and stress in the films. Experimentally obtained diffraction patterns of the sample are compared with the standard powder diffraction files published by the International Centre for Diffraction Data (ICDD).

The average grain size of the film can be calculated using the Scherrer's formula [15],

$$d = \frac{0.9\lambda}{\beta Cos\theta} \qquad (2.10)$$

where, λ is the wavelength of the x-ray and β is the full width at half maximum intensity in radians.

The lattice parameter values for different crystallographic systems can be calculated from the following equations using the (hkl) parameters and the interplanar spacing d.

Cubic system, $$\frac{1}{d^2} = \frac{h^2 + k^2 + l^2}{a^2} \qquad (2.11)$$

Tetragonal system, $$\frac{1}{d^2} = \frac{h^2 + k^2}{a^2} + \frac{l^2}{c^2} \tag{2.12}$$

Hexagonal system, $$\frac{1}{d^2} = \frac{4}{3}\left(\frac{h^2 + hk + k^2}{a^2}\right) + \frac{l^2}{c^2} \tag{2.13}$$

X-ray diffraction measurements of the films in the present studies were done using Rigaku automated x-ray diffractometer. The filtered copper Kα (λ=1.5418A^0) radiation was used for recording the diffraction pattern.

2.3.3 Scanning Electron Microscope (SEM)

The Scanning Electron Microscope (SEM) is a microscope that uses electrons rather than light to form an image. There are many advantages for using the SEM instead of an optical microscope [17]. The SEM has a large depth of field, which allows a large amount of the sample to be in focus at one time. The SEM also produces images of high resolution, which means that closely spaced features can be examined at a high magnification. Preparation of the samples is relatively easy since most SEMs only requires that sample should be conductive. The combination of higher magnification, larger depth of focus, greater resolution, and ease of sample observation makes the SEM one of the most heavily used instruments in current research and development. The electron beam comes from a filament, made of various types of materials. The most common is the tungsten hairpin gun. This filament is a loop of tungsten that functions as the cathode. A voltage is applied to the loop, causing it to heat up. The anode, which is positive with respect to the filament, forms powerful attractive forces for electrons. This causes electrons to accelerate toward the anode. The anode is arranged, as an orifice through which electrons would pass down to the column where the sample is held. Other examples of filaments are Lanthanum Hexaboride filaments and field emission guns.

The streams of electrons that are attracted through the anode are made to pass through a condenser lens, and are focused to very fine point on the sample by the objective lens (fig. 2.5). The electron beam hits the sample, producing secondary electrons from the sample. These electrons are collected by a secondary detector or a backscatter detector, converted to a voltage, and amplified. The amplified voltage is applied to the grid of the CRT that causes the intensity of the spot of light to change. The image consists of thousands of spots of varying intensity on the face of a CRT that correspond to the topography of the sample.

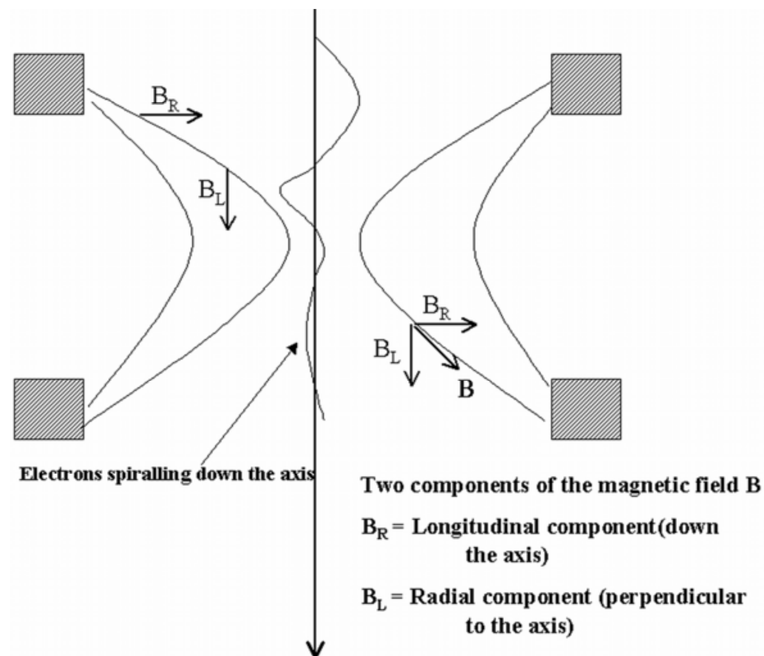

Figure. 2.5 The focusing of electrons in SEM

Figure 2.6 shows the interaction of electrons with matter in order to make sure we have the information from the sample surface only, when a SEM is used, the column must always be at a vacuum. Otherwise there are chances for contamination of the sample and also the electrons beam would induce

ionisation in any background gas that would effect the measurement being made on the sample.

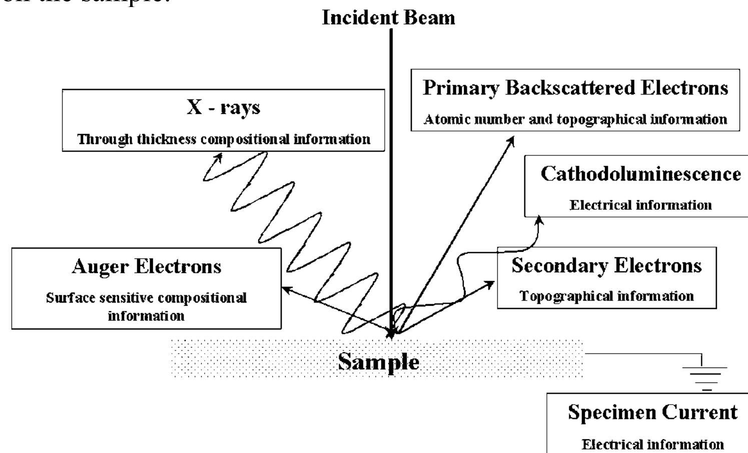

Figure. 2.6 In SEM set up, interaction of electron with the sample produces both photons and electrons.

2.3.4 Energy Dispersive X-Ray (EDX) Analysis

EDX Analysis stands for energy dispersive x-ray analysis. It is sometimes referred to as EDAX analysis. It is a technique used for identifying the elemental composition of the specimen, or an area of interest thereof. The EDX analysis system works as an integrated feature of a scanning electron microscope (SEM), and cannot operate on its own without the latter [17,18]. During EDX Analysis, the specimen is bombarded with an electron beam inside the scanning electron microscope. The bombarding electrons collide with the specimen atom's own electrons, knocking some of them off in the process. A higher-energy electron from an outer shell eventually occupies a position vacated by an ejected inner shell electron. To be able to do so, however, the outer electron must give up some of its energy by emitting an x-ray. The amount of energy released by the transferring electron depends on which shell it is transferring from, as well as which shell it is transferring to. Furthermore, the atom of every element releases x-rays with unique amounts of energy during the transferring process. Thus, by measuring the energy of

the x-rays emitted by a specimen during electron beam bombardment, the identity of the atom from which the x-ray was emitted can be established.

The EDX spectrum, is a plot of intensity of x-ray vs energy of the emitted x-ray. An EDX spectrum normally displays peaks corresponding to the energy levels for which the most x-rays had been received. Each of these peaks is unique to an atom, and therefore corresponds to a single element. The higher the intensity of peak in a spectrum, the more concentrated the element is in the specimen. An EDX spectrum plot not only identifies the element corresponding to each of its peaks, but the type of x-ray to which it corresponds as well. For example, a peak corresponding to the amount of energy possessed by x-rays emitted by an electron in the L-shell going down to the K-shell is identified as a K_α peak. The peak corresponding to x-rays emitted by M-shell electrons going to the K-shell is identified as a K_β peak as shown in figure. 2.7.

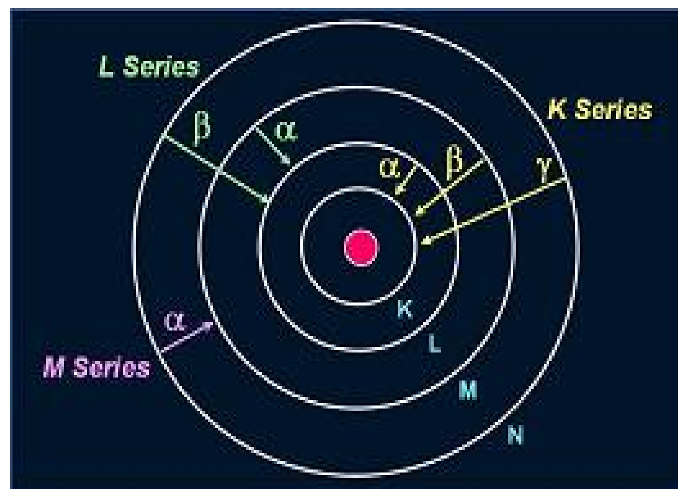

Figure. 2.7 Electronic transitions showing the emission of x rays.

2.3.5 Atomic Force Microscopy (AFM)

Following the invention of the scanning tunnelling microscope (STM), a number of new scanning probe microscopes (SPM) has been developed that use the key components of the STM. One of the most important SPM is the atomic force microscope (AFM) [18]. In atomic force microscopy a tip, integrated to the end of a spring cantilever, is brought within the interatomic separations of a surface, such that the atoms of the tip and the surface are influenced by interatomic potentials. As the tip is rastered across the surface, it bounces up and down with the contours of the surface. By measuring the displacement of the tip (*i.e.* the deflection of the cantilever), one can theoretically map out the surface topography with atomic resolution. The first AFM's measured cantilever deflections using a piggy-backed STM. Later instruments used more practical optical techniques. The AFM is essentially identical in concept to the scanning profilometer, except that the deflection-sensitivity and resolution are improved by several orders of magnitude. There are a large number of applications for the AFM, including biological systems, polymers, and a host of insulator and semiconductor materials.

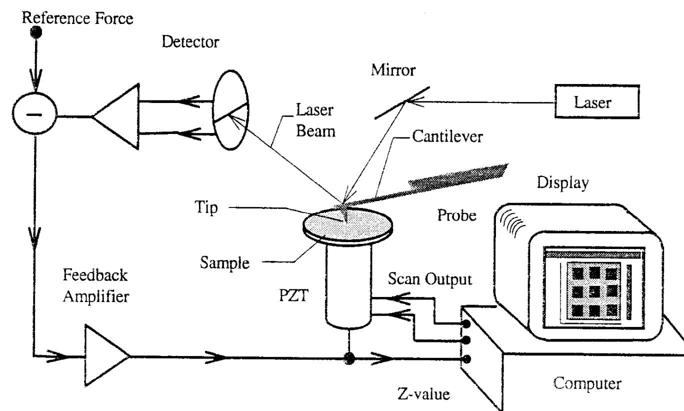

Figure. 2.8 The essential elements of an AFM

An AFM images a surface in a manner analogous to the gramophone stylus sensing the groves of gramophone disk. The essential elements of an AFM

are shown in the figure 2.8. The tip is attached to a cantilever type spring as shown in the figure 2.9. As the tip and sample interact, forces act on the tip and cause the cantilever (spring) to deflect. The cantilever position is monitored by a position detector. The output of the detector is connected to a feedback controller that regulates the force between the sample and the tip by moving the sample up or down. The sample is moved by a PZT scanning actuator. The cantilever must be soft enough to deflect a measurable amount without damaging the surface features of the sample. The amount of deflection is proportional to the force acting on the tip.

$$F_{spring} = -k \cdot \Delta Z \tag{2.14}$$

where F is the force on the sample, k is the spring constant of the cantilever, and, ΔZ is the deflection of the cantilever.

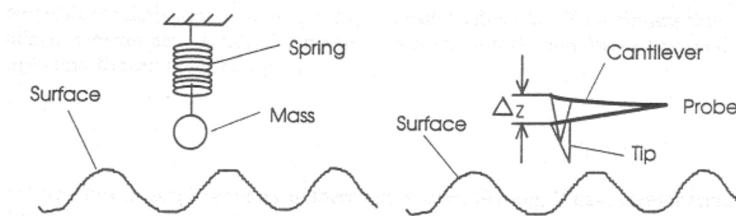

Figure. 2.9 Attachment of the tip to the cantilever in an AFM.

Various modes of AFM measurements include contact mode, dynamic force mode, phase mode. Friction force microscope, magnetic force microscope, surface potential microscope, etc are scanning probes microscopes slight variation in the working principles from that described above.

2.3.6 Optical characterisation

i) ***Determination of band gap energy***

Intrinsic optical absorption of a single photon across the band gap is the dominant optical absorption process in a semiconductor. When the energy of the incident photon ($h\nu$) is larger than the band gap energy the excitation of electrons from the valence band to the empty states of the conduction band occurs. The light passing through the material is then absorbed and the number of electron hole pairs generated depends on the number of incident photons $S_0(\nu)$ (per unit area, unit time and unit energy). The frequency ν is related to the wavelength λ by the relation, $\lambda = c/\nu$, where c is the velocity of light. The photon flux $S(x,\nu)$ decreases exponentially inside the crystal according to the relation [15],

$$S(x,\nu) = S_0(\nu) \exp(-\alpha x) \qquad (2.15)$$

where, the absorption coefficient α, ($\alpha(\nu) = 4\pi k\upsilon/c$) is determined by the absorption process in semiconductors and k is the extinction coefficient.

For the parabolic band structure, the relation between the absorption coefficient (α) and the band gap of the material is given by [19],

$$\alpha = \frac{A}{h\nu} (h\nu - E_g)^r \qquad (2.16)$$

where, r = 1/2 for allowed direct transitions, r = 2 for allowed indirect transitions, r = 3 for forbidden indirect transitions and r = 3/2 for forbidden direct transitions. A is the parameter which depends on the transition probability. The absorption coefficient can be deduced from the absorption or transmission spectra using the relation,

$$I = I_0 e^{-\alpha t} \qquad (2.17)$$

where, I is the transmitted intensity and I_0 is the incident intensity of the light and t is the thickness of the film. In the case of direct transition, from equation 2.16, $(\alpha h\nu)^2$ will show a linear dependence on the photon energy ($h\nu$). A plot of $(\alpha h\nu)^2$ against $h\nu$ will be a straight line and the intercept on energy axis at $(\alpha h\nu)^2$ equal to zero will give the band gap energy.
The transmissions of the thin films were recorded using Hitachi uv-vis-nir 330 spectrophotometer and Jasco V500 spectrophotometer in the present studies.

ii) Photoluminescence

Luminescence in solids is the phenomenon in which electronic states of solids are excited by some energy from an external source and the excited states release energy as light. When energy comes from short-wavelength light, usually U.V, the phenomenon is called photoluminescence (PL)[20]
PL is divided into two major types: Intrinsic and extrinsic depending on the nature of electronic transition producing it.

a) ***Intrinsic luminescence***

There are three kinds of intrinsic: 1) band-to-band luminescence 2) exciton luminescence 3) cross-luminescence.

Band –to –band luminescence:

Luminescence owing to the band-to-band transition, ie to the recombination of an electron in the conduction band with a hole in the valance band, can be seen in pure crystal at relatively high temperature. This has been observed in Si,Ge and IIIb-Vb compounds such as GaAs.

Exciton luminescence:

An exciton is a composite particle of an excited electron and a hole interacting with one another. It moves in a crystal conveying energy and produces luminescence owing to the recombination of the electron and the hole. There are two kinds of excitons: Wannier exciton and Frenkel exciton.

The Wannier exciton model express an exciton composed of an electron in the conduction band and a hole in the valence band bound together by couloumb interaction. The expanse of the wavefunction of the electron and hole in Wannier exciton is much larger than the lattice constant. The excitons in IIIb-Vb and IIb-VIb compounds are examples for Wannier exciton. The Frenkel exciton model is used in cases where expanse of electron and hole wave function is smaller than lattice constant. The excitons in organic molecular crystals are examples of Frenkel exciton.

Cross luminescence

Cross luminescence is produced by the recombination of an electron in the valance band with a hole created in the outer most core band. This is observed in number of alkali and alkaline-earth halides and double halides. This takes place only when the energy difference between the top of valance band and that of conduction band is smaller than the bandgap energy. This type of luminescence was first observed in BaF_2.

b) *Extrinsic luminescence*

Luminescence caused by intentionally incorporated impurities, mostly metallic impurities or defects is classified as extrinsic luminescence. Most of the observed type of luminescence of practical application belongs to this category. Intentionally incorporated impurities are activators and materials made luminescent in this way are called phosphors.
Extrinsic luminescence in ionic crystals and semiconductors is classified into two types: unlocalized and localized. In the unlocalized type, the electrons and holes of the host lattice participate in the luminescence process, while in localized type the luminescence excitation and emission process are confined in a localized luminescence center.

unlocalised type:

In semiconductors donors and accepters act as luminescence activators. There are two types of luminescence transitions i.e. the transition of a free carrier to a bound carrier and the transition of a bound electron at a donor to

a bound hole at an acceptor. These kinds of luminescence lines and bands are usually observed in compound semiconductors such as IIIb-Vb and IIb-VIb compounds.

Localised type:

Various kinds of metallic impurities intentionally incorporated in ionic crystals and semiconductors create efficient localized luminescence centres. Localized type centres are classified into: 1) allowed transition type b) forbidden transition type in terms of electric dipole transitions. The electric dipole transition can take place between energy levels with different parities. The selection rule for this transition in atoms is $\Delta l = \pm 1$. When atoms and ions are incorporated in crystals, the forbidden character of the dipole transition is altered by the perturbation of the crystal electric field, so that the forbidden transition becomes allowed to some degree.

Many phosphors that are important from a practical viewpoint are synthesized by incorporating following activators.

a) Allowed transition type:

(i) s↔ p transition –F centre↔(an electron trapped at an anion vacancy)

(ii) s^2↔sp transition Tl^{+} ,Sn^{2+}, Pb^{2+}, Sb^{3+}, Bi^{3+}

(iii) f ↔d transition Eu^{2+}, Ce^{3+}

b) Forbidden transition type:

(i) d↔d transition Ti^{3+} , Cr^{3+} , Cr^{2+} , Mn^{4+} , Mn^{2+} , Fe^{3+} , Fe^{2+}

(ii) f↔f transition - Pr^{3+} , Nd^{3+} , Sm^{3+} , Eu^{3+} , Tb^{3+} , Tm^{3+} (and other trivalent rare earth ions)

Iron group ions show luminescence owing to the $3d^n \leftrightarrow 3d^n$ $(n = 2 - 8)$ transition in the visible to infrared region. Among them, Cr^{3+} and Mn^{4+} ions with the $3d^3$ configuration and the Mn^{2+} ion with the $3d^5$ configuration are important for phosphor application. The luminescence spectra of Mn^{2+} are always bands, which vary over a wide visible range from blue to red [20].

Two types of luminescence spectra can be distinguished: excitation and emission. In the case of an excitation spectrum the wavelength of the exciting light is varied and the intensity of the emitted light at a fixed emission wavelength is measured as a function of the excitation wavelength. The excitation spectrum gives information on the position of excited states just as the absorption spectrum does, except that the former reveals only the absorption bands that result in the emission of light. The observed differences between the absorption and excitation spectra can yield useful information. An emission spectrum provides information on the spectral distribution of the light emitted by a sample. The time resolved PL measurements are a powerful tool for the determination of the radiative efficiency. The radiative efficiency specifies the fraction of excited states, which de-excite by emitting photons. [16,20].

The emission and excitation spectra for the powder and thin film samples are recorded using Fluorolog –3 spectroflurometer consisting of 450W Xenon arc lamp, monochromator and a CCD detector.

2.3.7 Electrical characterisation

i) ***Resistivity by two probe method***

The resistivity of the films is determined by the two-probe method with the electrodes in planar geometry. Evaporated indium layers or high conducting silver paste was used as the electrodes. The current voltage measurements were carried out using a Keithley`s source measure unit (Model SMU 236). The resistivity (ρ) of the films is calculated applying ohm's law, by the relation $\rho = RA/L$. Where R is the resistance given by the slope of the current – voltage characteristic curves. A is the area of the film in planar geometry which is given by the product of the film thickness and the width of the film. L is the spacing between the electrodes.

ii) ***Hall measurement***

The electrical resistivity of a semiconductor thin film can be written using Ohm's law,

$$\rho = \frac{1}{en\mu} \tag{2.18}$$

where 'ρ' is the film resistivity, e is the electronic charge, n is the number of carriers corresponding to the carrier concentration and 'μ' is the carrier mobility. According to Ohm's law the carrier mobility affects resistivity. Low resistivity can be achieved by increasing the carrier concentration or mobility or both. Increasing carrier concentration is self-limiting because at some point the increased number of free carriers decreases the mobility of the film due to carrier scattering. Hence there is a trade off between the carrier density and carrier mobility for achieving low resistivity.

In the case of Zinc oxide films, the resistivity (ρ), carrier concentration (n), carrier mobility (μ), and sheet resistance were measured using four point probe in the Van der Pauw configuration [21]. Samples used were 1cm x 1cm in size. The ohmic contacts were made using silver paste. The silver paste was applied at the corners of the sample symmetrically as shown in figure 2.10.

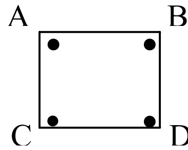

Figure 2.10. Symmetric connections for taking the hall measurements

Let R_1 be the potential difference between A and B per unit current through C and D or vice versa. Similarly R_2 the potential difference between B and C per unit current through D and A.
Then sheet resistance R_s can be calculated using the relation

$$R_s = \left(\frac{\pi}{\ln 2}\right)\left(\frac{R_1 + R_2}{2}\right) f\left(\frac{R_1}{R_2}\right) \tag{2.19}$$

Where $f\left(\frac{R_1}{R_2}\right)$ is the Van der Pauw function and is given by the relation,

$$f\left(\frac{R_1}{R_2}\right) = 1 - 0.3466\left(\frac{R_1 - R_2}{R_1 + R_2}\right)^2 \qquad (2.20)$$

The Hall signal was measured between two ends while passing the current through the other two ends. Hall mobility is,

$$\mu = \Delta R \times \frac{10^8}{BR_s} \qquad (2.21)$$

Where ΔR is the change in resistance due to magnetic field (B), which was applied to measure Hall voltage. Carrier concentration was determined using the equation 2.18. The hall coefficient R_H is given by,

$$R_H = \mu \ \rho \qquad (2.22)$$

The type of carriers can be understood from the sign of the R_H. The negative values of R_H correspond to the electrons (n-type) and positive values to holes (p-type) responsible for conduction..

iii) *Nature of conductivity – Carrier type*

Thermo power measurement is a useful technique for the evaluation of the type of carriers responsible for the conduction. Thermo power measurements were carried out using an automated set up, the details of which are given in chapter 3. The set-up is similar to the one designed by Young et al [22]. The slope of the thermoemf versus ΔT curve gives the Seebeck coefficient. A positive Seebeck coefficient is obtained when the majority carriers are holes and a negative Seebeck coefficient for electrons. This technique is especially useful for characterisation of type of carriers in semiconductor materials with low mobility for charge carriers.

2.4 References

[1.] L. I. Maissel and R. Glang, Handbook of Thinfilm technology Mc Graw Hill Book Company, , 1983

[2.] A.Goswami, Thin Film Fundamentals. New Age International (P) Limited, New Delhi, 1996

[3.] K.L. Chopra, Thin Film Phenomena, Robert E. Krieger Publishing Co. Inc., New York, 1979

[4.] L. Holland, Vacuum Deposition of Thin films, John Wiley & Sons Inc., New York, 1956

[5.] J. George, Preparation of thin films, Marcel Dekker Inc.,NewYork, 1992.

[6.] D.L. Smith, Thin-film deposition, Mc Graw – Hill Inc, Washington D.C.,1995

[7.] F.L.Akkad, A.Punnose, J.Prabu, J.Appl.Phys A 71(2000) 157

[8.] B.Chapman, Glow Discharge Processes, John Wiley & Sons, New York, 1980

[9.] V. S. Smentkowski, Progress in Surface Science **64** (2000) 1

[10.] R.Venkatesan and Steven M. Green; *The industrial physicist* (1996) 22.

[11.] Douglas B. Chrisey and Graham K. Hubler; *Pulsed Laser Deposition of Thin Films*, John Wiley and sons Inc., New York, 1994

[12.] O.Weiner, Wied.Ann. **31**(1887) 629

[13.] S. Tolansky, Multiple Beam Interferometry of Surfaces and Thin films, Oxford University Press, New Jersy, 1948

[14.] Veeco Dektak 6M Manual 2004

[15.] B.D. Cullity and S.R. Stock, Elements of X ray diffraction, Third edition, Prentice Hall, New Jersey, 2001

[16.] Charles Kittel, Introduction to Solid State Physics, Seventh edn, Wiley Eastern Limited, New Delhi, 1996

[17.] D. K. Schroder *Semiconductor material and device characterization*, second edition, A Wiley-interscience publication, New York, 1998.

[18.] P. E .J. Flewit and R. K. Wild, *Physical methods for material characterization*, second edition, IOP publishing, London, 2003.
[19.] J.Bardeen, F.J.Blatt and L.H. Hall, Proceedings of Photoconductivity Conf. (1954,Atlantic City), (Eds) R.Breckenridze, B.Russel and T.Hahn, J.Wiley and Chapman and Hall, New York, 1956
[20.] D.R.Vij (Ed.) *Luminescence of solids*, Plenum Press, New York, 1998
[21.] Manual, Model H 50 MMR technologies Inc. California
[22.] D.L.Young, T.J.Coutts, V.I. Kaydanov, Rev. Sci. Instruments **71** (2000) 462

Chapter 3

Fabrication Of A Setup For Thermopower Measurements

An automated set up for measuring the thermopower was built. A custom software was used to control a predetermined difference in temperature. The temperature difference can be reversed. The setup was tested using copper and was found to give the thermopower values in close agreement with those reported in literature. The thermopower of various samples were measured.

3.1 Introduction

Common transport phenomena's like reistivity, Hall, Seebeck effects and some other lesser known phenomena's like Nernst, Ehingshausen effects provide valuable insight into the physical characteristics of materials. In other words, measurement of transport properties provides an important tool for material characterisation. It provides information on carrier degeneracy, type, scattering mechanisms, Fermi level, effective mass, and band structure [1].

Transparent conducting oxide (TCO) thin films are finding their place in large volume applications. They are being used as contacts for cathode ray tubes, Flat panel displays etc. With the development of p-type materials, there are possibilities for a new generation of contacts of p type semiconductors and devices. But the currently developed p type TCOs exhibit low mobility that is difficult to measure by conventional dc hall measurement technique. For example it is difficult to extract the sign of the carriers from the Hall coefficient measurements for carriers with mobility less than 10^{-5} m^2 V^{-1} s^{-1}. The TCO's have mobility in this range and thereby the measurement of Seebeck coefficient provides a method for identification of type of charge carriers and also quantifies the no of charge carriers in the sample. Since a larger Seebeck coefficient implies a larger number of carriers we can also get a quantitative measure of the number of carriers.

3.2 Experimental

The sample holder for the thermopower measurement is similar to the one reported by Young et. al. [1]. The sample holder is shown in figure 3.1, it is made from copper and can be thermally attached to a closed cycle two stage cryostat. The copper blocks 'F' and 'G' are electrically isolated from each other and also from the sample-holder stage, but thermally connected via a sheet of 2 mm thick teflon. The heating element in the blocks is carbon resistance (100Ω) mounted with stycast^{TM} epoxy in hole bored through the centre of the heating blocks parallel to its axis. Embedded in, but electrically isolated from, the heater block is a type 'K' differential thermocouple made

from chromel alumel. The junctions of the chromel alumel differential thermocouple are located as close as possible (Below 1mm from the surface of the blocks F,G where the samples are mounted) to the mounting surface of the heater block and are thermally anchored which stycast™ epoxy .

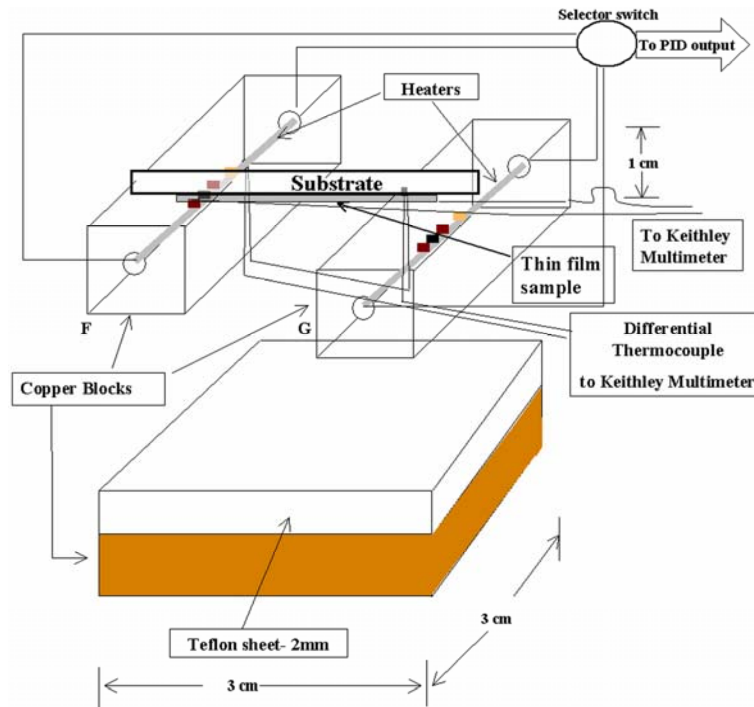

Figure 3.1. An exploded view of the Seebeck measurement sample holder.

All the thermocouple junctions are located just under the surface of the copper blocks exactly where the sample is loaded. Both of them are drilled and tapped with holes on the inside of the channel between the blocks. All of the wires exiting the sample holder are wound in twisted pairs to minimise magnetic interference and these pairs are wound around the cryostat expander arm multiple times to minimise heat conduction [2].

The two ends of the thermocouple and the ends of the heater resistor are connected to the PID – temperature controller which controls the temperature gradient between the blocks.

The objective of the temperature controller is to maintain a temperature difference of 1^0C between the two copper blocks of the experimental set-up in order to facilitate the thermo e.m.f. measurement of the thin film sample. One crucial aspect in the selection of a proper temperature sensor is we have used a differential thermocouple. (type K, Cromel-alumel) owing to the convenience it offers in the measurement of temperature difference and also due to its low thermal inertia which supports good control. However, the sensitivity of a thermocouple is relatively low, only about 40µV/^{0}C in the case of a type-K thermocouple This is a serious challenge, as it demands a high performance amplifier capable of amplifying microvolt level signal with the required accuracy. It is not easy to construct such an amplifier using locally available components hence we decided to use an existing micro voltmeter (Model – KEITHLY 2000) for temperature measurement. A personnel computer is used to implement the control function, which communicates with the micro voltmeter through IEEE-488 interface. The heater voltage is calculated using PID control algorithm and it is sent to the heater through a D/A channel of an analogue interface and which is inserted into one of a bus expansion slot of the PC. The entire control programme that also includes provision for a real-time graphical display (figure 3.2) of the control parameter is written in C-language.

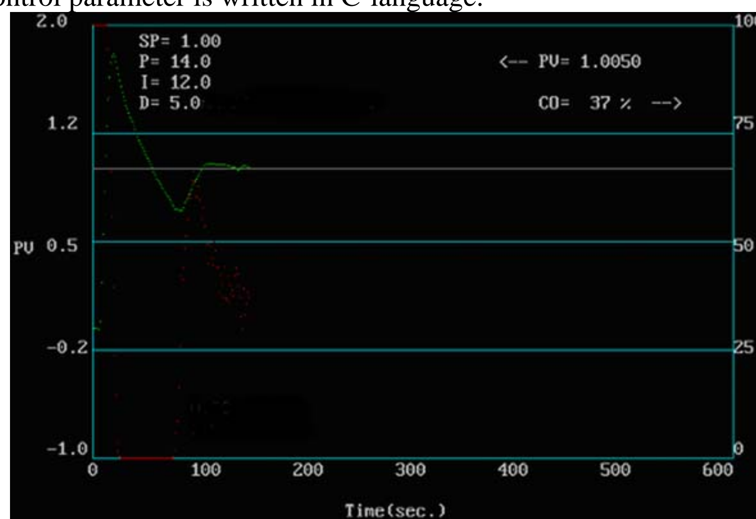

Figure 3.2. Screen dump of the process controller program output

3.2.1. Process control system

The basic strategy by which the control system operates is quite logical and natural. In process control the basic objective is to maintain a quantity at some desired value regardless of external influences. The desired value is called the set point or reference value. The elements of a process control system are the various separate parts of the system. The basic elements of the process control system are the following:

- Process
- Measurement
- Error detector
- Controller

3.2.2. Block diagram

Each element in the process-control system is represented in a block diagram. Figure 3.3 shows the block diagram.

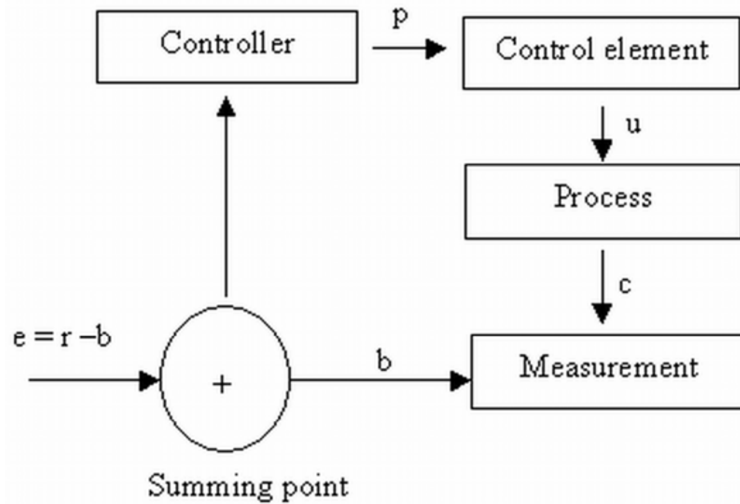

Figure 3.3. Block diagram of a control loop

3.2.3. Control system parameters

We can examine the general properties of the controller shown below in figure 3.4.

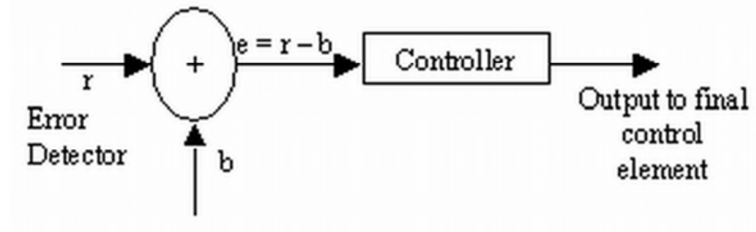

Figure 3.4. The detector and controller diagram.

(1) Inputs to the controller are measured, indication of both the controlled variable and a set point representing the desired value of the variable are available.

(2) The controller input is a signal representing action to be taken when the measured value of the controlled variable deviates from the set point.

The measured indication of the variable is denoted by b, while the actual variable is indicated by c.

3.2.4 Error

The deviation of error of the control variable from the set point is given by

$$e = r-b$$

Here, e = error, b = measured indication of variable, r = set point of variable
The above equation expresses error in an absolute sense, or in units of the measured analog of the control signal.
To describe the controller operation in a general way, it is better to express the as percent of the measured variable range (i.e, the span). The measured value of the variable can be expressed as percent of span over a range of measurement by the equation,

$$Cp=((C-C_{min})/(C_{max}-C_{min})) \quad (3.1)$$

Where

C_p=measured value as percentage of measurement range

C= actual measured value

C_{max}=maximum of measured value

C_{min}=minimum of measured value

The previous equation is in terms of the actual measured variable C, but the same equation can be expressed in terms of the measured indication b. It is only necessary to translate the measured minimum and maximum to b_{max} and $b_{min.}$

To express error as percent of span, it is also necessary to write both the set point and measurement in terms of percent of span and take the difference as per equation (3.1).

The result is

e_p=(r-b/b_{max}-b_{min})x100 (3.2)

Where

e_p= error expressed as percentage of span

A positive error indicates a measurement below the set point, and a negative error indicates a measurement above the set point. In the computer software the error is expressed by an equation such as

DE=(D_{SP}-DV)/(D_{MAX}-D_{MIN}) (3.3)

Where DV=measured input

D_{SP}=set point

D_{MAX}=maximum of range

D_{MIN}= minimum of range

3.2.5 Variable range

The variable under control has a range of values within which control is to be maintained. This range can be expressed as the minimum and maximum value of the variable or the normal value plus and minus the spread about this normal. When a computer-based control system is used, the dynamic variable is converted into an n-bit digital signal. Often, the transformation is

made so that all 0's are the minimum values of the variable and all 1's are maximum values.

3.2.6. Control parameter range

Another range is associated with the control output. Here we assume the final control element has some minimum and maximum on the process. The controller output range is the translation of out put to the range of possible values of final control alignment. The output is expressed as a percentage where 0% is the minimum controller output and the 100% the maximum.

The controller output as a percent of full scale when the output varies between specified limit given by

$$P=(u-u_{min}/u_{max}-u_{min})x100 \qquad (3.4)$$

Where

P=controller output as percent of full scale
U= value of the output
U_{max}=maximum value of controlling parameter.
U_{min}=minimum value of controlling parameter.

3.2.7. Continuous controller modes

The most common controller action used in process control is one or a combination of continuous modes. In these modes the output of the controller changes smoothly in response to the error or rate of change of error.

i) The PID control

PID control means proportional, Integral and/or Derivative control meaning that the control signal may be proportional, derivative or an integral of the error value. These three types may be used separately or in co-ordination as required by the application.

ii) Proportional control

In the system with proportional control there is continuous linear relation between he value of the control variable and the correction applied. The applied correction is changed by the same amount for each unit of deviation. Proportional control in pictorially demonstrated in figure 3.5.

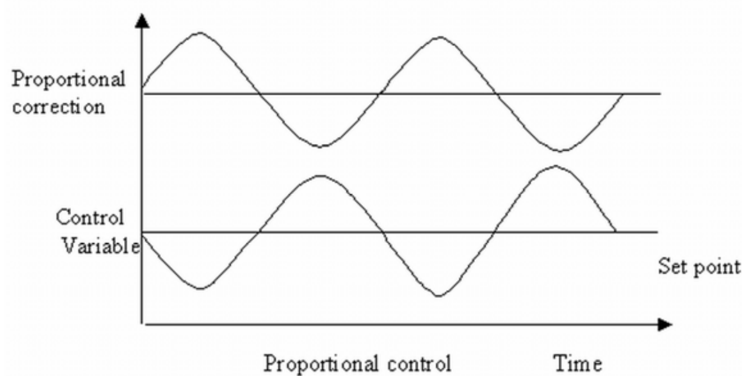

Figure 3.5. Variation of proportional correction term.

The following equation describes the input-output relation for proportional control.

$$P = K_p e_p + P_o \qquad (3.5)$$

$$\text{and } K_p = \frac{100}{PB}$$

Where P = output at any given time

P_o = output when e = o is zero error.

e = error signal i.e. (set point value – measured value)

Proportional band PB (in %) is defined as percentage of full scale change in input required changing the output from 0-100%. The proportional gain is defined as

G_{in} = Proportional Band/100

In proportional controllers when the control variable deviates from the set value due to momentary disturbance, the controller gives a correction, which

is proportional to deviation. The correction forces the controlled variable towards the set value reducing the error, which is in turn, causes a reduction in the correction action.

1. If the error is zero, the output is a constant equal to P_o.
2. If there is error, for every 1% of error a correction of K_p percent is added to or subtracted from P_o depending on the reverse or direct action of the controller.
3. There is a band of error about zero of magnitude P_B within which the output is not saturated at 0% or 100%.
4. An important characteristic of the proportional control mode is that it produces a permanent residual error in the operating point of the controlled variable when a change in load occurs.

This error is called offset, it can be minimised by a larger constant K_p, which also reduces the proportional band. If a transient error occurs the system responds by changing controller output in correspondence with the transient to effect a return to zero error. Suppose, however, a load, change occurs that requires a permanent change in controller output to produce the zero error state. The proportional mode is provided through the software by an equation is given by

$P=P_0+KP*DE$

$PR_{OUT}=P*R_{OUT}$

P_O= fraction of out put with no error

KP= proportional gain (%/%)

P=fraction of output with error

R_{OUT}= maximum output

PR_{OUT}=output

Because one-to-one correspondence exist between controller output and error, it is clear that a new zero error controller output can never be achieved. Instead, the system produces a small permanent offset in reaching a compromise position of controller output under new loads. The manual action to compensate the proportional control above is that it is not suitable for taking case of load variations.

iii) Integral control

The integral control signal is proportional to error signal integrated over a period of time. Integral action continuous to build up a correction till the error is forced to zero. The integral control overcomes the drawback of offset present in proportional control, as the control responds to both magnitude of error and duration of error. The correction given by integral action is given by.

$$\frac{dp}{dt} = K_I e_p \qquad (6)$$

Where $\frac{dp}{dt}$ = rate of controller output changes (%/s)

K_I = constant relating the rate to the error [(%/s)/%]

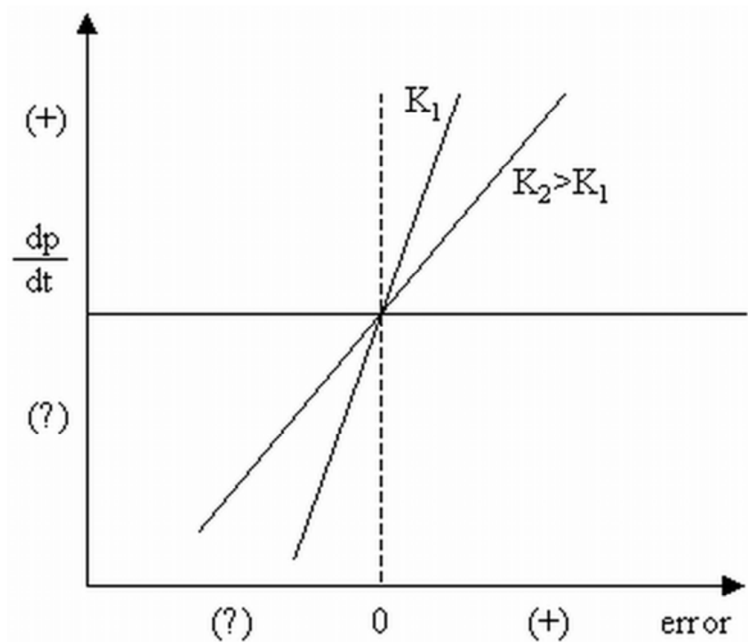

Figure 3.6. The rate of output changes depends on gain and error

In some cases the inverse of K_I, called the integral time $T_I = 1/K_I$ expressed in second or minute, is used to describe the integral mode.

Then the actual control output is

$$P_{(E)} = K_I \int_o^t e_p(t)\, dt + P_{(o)} \qquad (6)$$

$P_{(o)}$ = controller output at t = 0

The limitation of integral control is that it is also acts as a correction build up gradually. Thus the equation shows that the present controller output depends on the previous error from when the observation started at t=0. The constant K_I express the scaling between the error and controller output. Thus a large value of K_I means ha small error produces a large value of output and vice versa. The figure. 3.6 shows the graphical illustration of the relation between the rate of change of output and error for two different values of K_I.

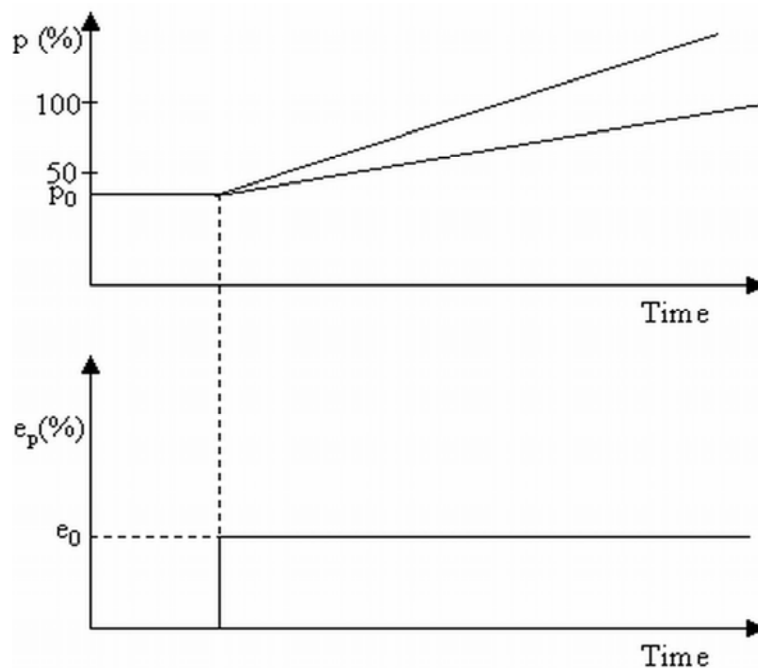

Figure 3.7. Illustration of integral mode response to a constant error

The figure 3.7 shows how for a fixed error the different K_I values produce the different values of output as a function of time predicted by the equation. Thus we see that the faster rate provided by K_I causes a much greater controller output at a particular time after the error is generated.

iv) Derivative control

In this control, the correction is proportional to the rate of change of error. As soon as there is deviation, the derivative control generates a momentary excess correction, which speeds up the corrective action.

The correction given by the derivative controller is

$$D = K_D \frac{dep}{dt} \qquad (3.7)$$

Where D = Derivative control signal

Derivative mode of controller action where an output of 50% has been assumed for the zero derivative state

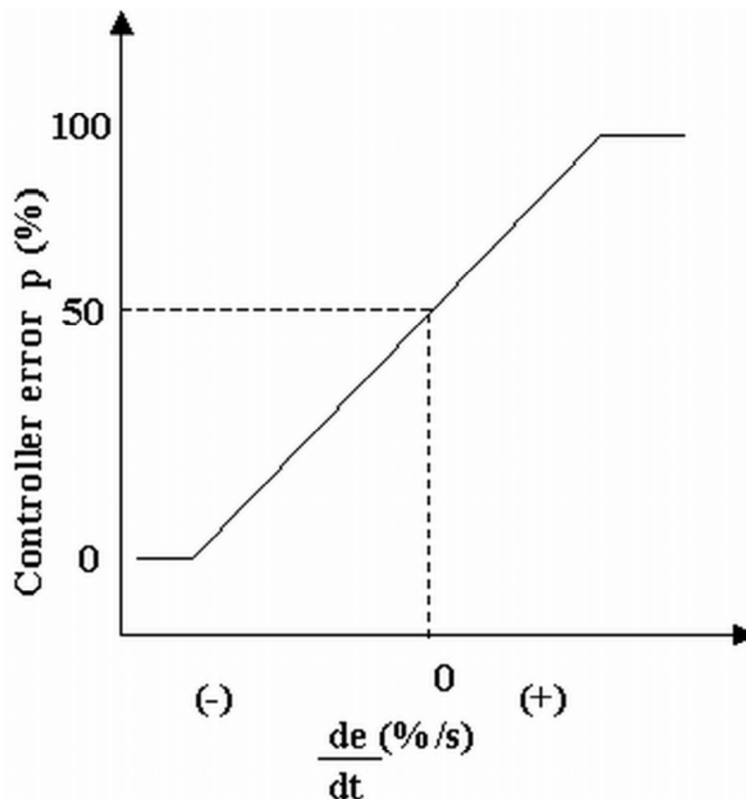

Figure 3.8. Rate of error change

The derivative gain constant is also called derivative time and is expressed in minutes. Figure 3.8 shows the controller output for the rate of change of error that is a unique of controller output. The time plot of error and controller response further shows the behaviour of this mode. The extent of controller output depends on the rate at which the error is changed and not on the error.

v) Proportional plus integral plus derivative control (PID)

The algorithm used for more demanding tasks are PID controller with proportional, integral and derivative action simultaneously. The correction given is represented by

$$P = K_p e_p + K_p K_I \int_o^t e_p dt + K_p K_D \frac{de_p}{dt} + P_I(o) \qquad (3.8)$$

This mode eliminates the offset of the proportional mode and still provides fast response.

PID controllers are used where the derivative action can help to compensate for lags in the process. For example, in temperature control loop the adverse effect of lag associated in the temperature measuring element can be partially reduced by derivative control action. The controller senses the rate of movement from the set point and starts moving the control value earlier than it would with only the proportional action. The integral action of the controller continuous with the time until the offset has completely vanished thus this mode of control employs the advantages of all the three modes as listed below.

1. Derivative action reduces the overshoot, which often occurs, when integral action is added to proportional action.
2. Derivative action counteracts the lag characteristics introduced by integral action.
3. Integral action reduces the offset when added to proportional control.

The figure 3.9 shows the behaviour of a typical feedback control system using different kind of control, when it is subjected to permanent disturbance like step change in load variation.

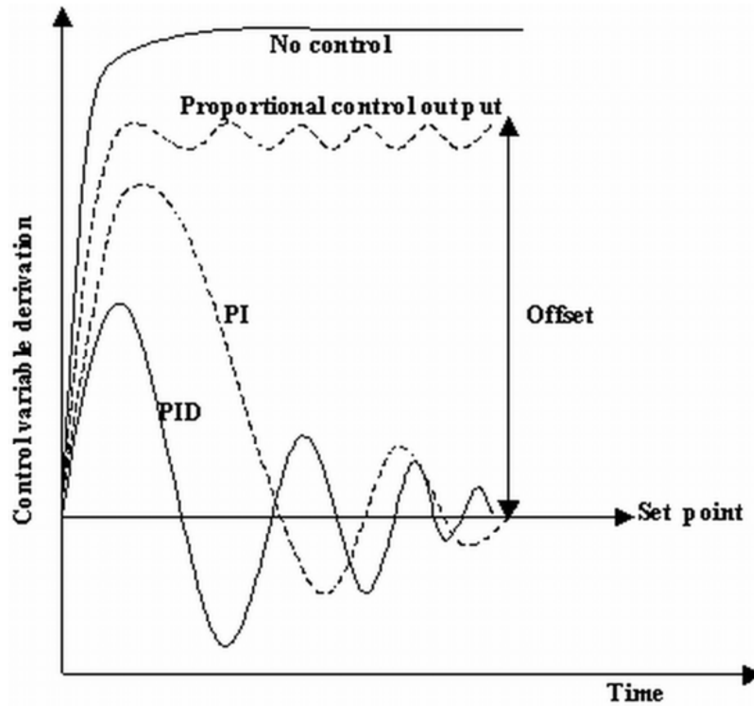

Figure 3.9. Control of output with Proportional mode alone and with PID mode

3.3. Temperature Controller System - Hardware And SoftWare

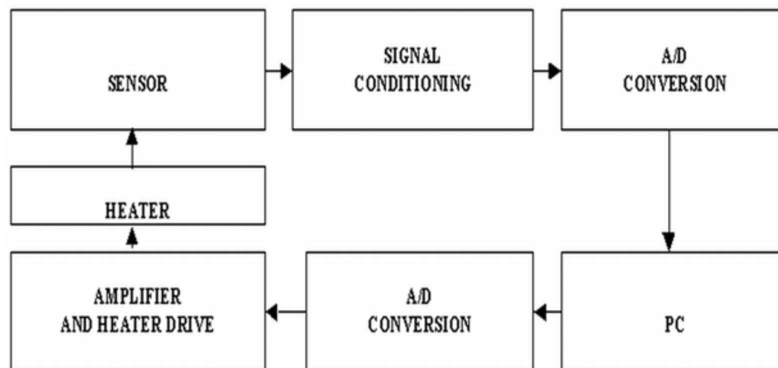

Figure 3.10. Elements of PID controller

3.3.1. Hardware

Block diagram of pc based temperature controller is as follows(fig 3.10)
The parts of hardware are described in detail below:
i) Sensors

Sensors provide a means of inputting information to a process control system. This information relates to external physical conditions such as temperature, position, and pressure. The data returned from the sensors together with control inputs from the operator will subsequently be used to determine the behaviour of the system. Any practical industrial process control system will involve the use of number of device for censoring a variety of physical parameters. The choice of sensor will be governed by a number of factors including accuracy, resolution, cost, and physical size.

ii) Interfacing

As the computer can process only digital data, there must be interface between the PC and the analog signals. This is made possible using an ADC/DAC digital 1/O card.

The IEEE-488

The IEEE-488 provides a means of interconnecting a micro controller with a vast range of test and measuring instruments. The bus is ideally suited to the implementation of auto test equipment (ATE).

Automatic measurement is important in many applications, not just within the production test environment.

Advantages of IEEE-488 based measurement systems incorporating pc-based controllers include:

1. Elimination of repetitive manual operation (freeing the test technician for more demanding tasks).
2. Equipment settings are repeatable (thus ensuring consistency of measurement)

3. Increased measurement through output (measurement rates are typically between 10 and 100 times faster than those which can be achieved by conventional manual method).
4. Reduction of errors caused by maladjustment or incorrect readings.
5. Consistency of measurement (important in applications where many identical measurements are made)
6. Added functionality (stored data may be analysed and processed in variety of ways.

Reduction in skill of operators (despite the complexity of equipment, user friendly software can guide operators through the process of connection and adjustment prior to making a measurement).

iii) Heater

The output from the computer is given to the heater circuit, which consists of the amplifier and the heater driver.

Experimental set – up

The sensor that is employed in this project is a chromel alumel thermocouple. Various thermocouples (or alloys of metals) and their operating range are shown in table3.1.

Table. 3.1. Different types of thermocouples and their usable range.

Type	Materials	Normal range
J	Iron-Constantan	-190°C to 760°C
T	Copper-constantan	-200°C to 371°C
K	Chromel-alumel	-190°C to 1260°C
E	Chromel-constantan	-100°C to 1260°C
S	90% platinum + 10% rhodium platinum	0°C to 1482°C
R	87% platinum + 13% rhodium – platinum	0°C to 1482°C

3.3.2 Interfacing

The ADC/DAC digital card used in this project is ALS-PC-02. This is designed to be used with XT/AT compatible 1/O channel bus. This card provides 12 bit A/D conversion facility (8/ 16 channel), 12 bit D/A conversion (2 channel) and 48 programmable 1/O lines. The salient features of the card are given below:

A/D converter:

- Jumper selected 8 differential / 16 single ended channels.
- Jumper selectable uni- polar analog input (0 to = 10V, + / -10V)
- 12-bit A/D converter with conversion speed of 25 microseconds.
- Provision to connect TTl compatible external trigger source for acquisition sequence.
- Provision to perform data acquisition in DMA mode using the system DMAZ channel 1.
- Acquisition frequency 25 kilohertz
- 3 programmable timers using 8253 which can be used for
  1. Acquisition sequence control / timing
  2. External synchronization
  3. Interruption mode.

D/A converter:

- Two 12 bit programmable D/A converters
- Jumper selectable unipolar/ bipolar operations
- +/-10V or 0-10V out put range
- Fast circuit setting time of less than 3 microseconds

Installation:

Detailed installation procedure of the card is given below.

Base address selection and 1/O map

The base address of the board is selected from the on- board Dipswitch settings SW/1 through SW/5. The address lines A 5 to A9 on the PC bus are used for address decoding. The switch settings SW/1 -SW/5 are compared with these address lines and the card gets selected if a match occurs. The relation of the DIP switches to address lines as follows:

Switch section	1	2	3	4	5	6	7	8
Address line	A9	A8	A7	A6	A5	X	X	X

X-indicates not used

A switch section in the 'ON' position corresponds to a logic "O' state and the OFF' position corresponds to a logic '1' state.

To sect a default base address of 300H, the switch settings are follows:

Switch selection	1	2	3	4	5	6	7	8
Status	OFF	OFF	ON	ON	ON	OFF	OFF	OFF

Other possible address 200H & 280H are given below:

To select a base address of 200H, the switch settings are as follows:

Switch section	1	2	3	4	5	6	7	8
Status	OFF	ON	ON	ON	ON	OFF	OFF	OFF

To select a base address of 280H, the switch settings are as follows:

Switch section	1	2	3	4	5	6	7	8
Status	OFF	ON	OFF	ON	ON	OFF	OFF	OFF

The address lines A0 through A4 are used for selection of an on - board 1/O devices. This implies that the board occupies 32 contiguous addresses above the base address. The addresses of the different on board 1/O device relative to the base address (BA) employed in this project work are shown below:

BA+14	LOW BYTE OF ADC
BA+15	HIGH BYTE OF ADC
BA+1C	LOW BYTE OF DACI
BA+1D	HIGH BYTE OF DACI

3.3.3. Software

The programming language used in this project is C. Despite its origin and close association with UNIX, C is now available in a variety of microcomputer implementations. These include the immensely popular Borland Turbo C and Quick C from Microsoft. Both of these packages will run on any PC or PC- compatible machine.

The C language is comparatively small it but it employ a powerful range of control flow and data structure. It has, therefore, becomes increasingly popular amongst programmers and software engineers. The language is well suited to the development of effective real- time applications and is ideally suited to the world of control and instrumentation. C is an excellent choice for small, tight, and fast application. The relatively small core of the language has been instrumental in ensuring in a high degree of portability from one hardware configuration to another. C offers some significant advantages in the development of software for real applications. The language promotes the use of structure, is highly portable and yields code, which is relatively compact. Furthermore, when complied it can offer execution speeds, which are far in excess of those, which can be obtained with comparable interpreted languages.

A number of include files are provides with the C run time library. These files contain macro and constant definition. Type definition and function declarations that are in the include files are given the file extension ‘h’. The descriptions of the files used in the program are as follows:
Bios.h: contains function, declaration and structure definition for the BIOS service routines.
Conio.h: contains functions, declaration for the consoles and port 1/O routines.
Dos.h: contains macro definitions, functions declarations and type definitions for the MS-DOS interfaces.
Stdio.h: contains definitions of constant, macros, and types. Also contains function declarations for the stream I/O functions. Example: printf, scan etc.
Graphics.h: contains function and constants to plot graph like put pixel, line etc.
The detailed controller program is give as appendix I

3.3.4. Heater

A 100Ω, 1/2 W carbon resistor is used as the heater in the copper block. The heater driver circuit consist of an operational amplifier IC- 741 and a transistor SL 100. the circuit diagram is shown in figure 3.11. The voltage swing capability of the input of the circuit enhances the current capability through the heater resistor R_h.

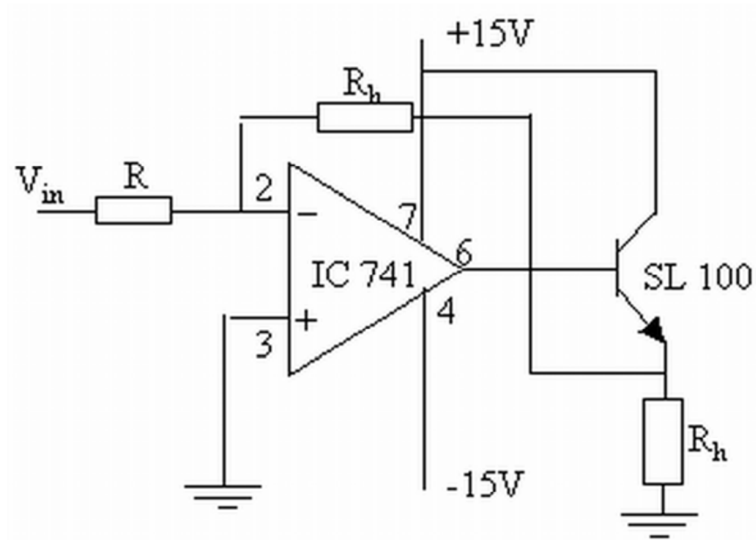

Figure 3.11. Power booster circuit.

The photograph of the setup mounted on the cold finger of the closed cycle helium cryostat is shown in figure 3.12.

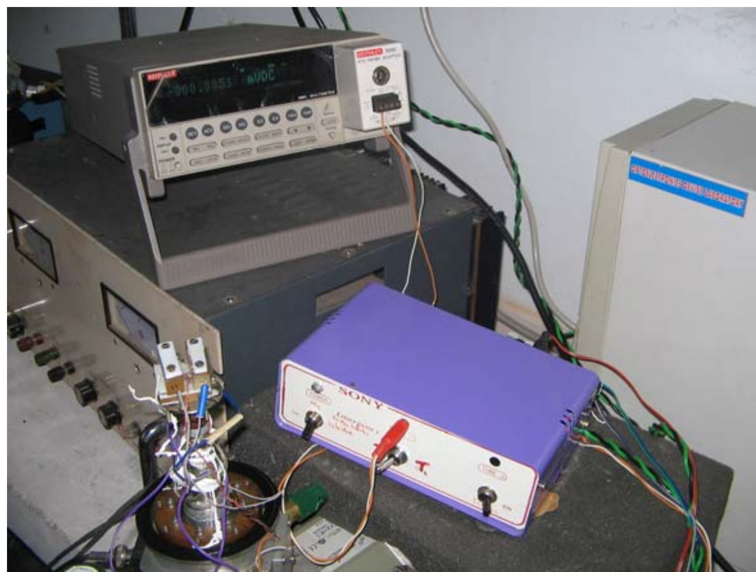

Figure 3.12. Photograph of the thermopower measurements setup mounted on the cold finger of the cryostat.

When the setup was tested at room temperature, it was seen that even a slight disturbance in the room was disturbing the thermal equilibrium (fig.3.13). So the whole setup was mounted onto the cold finger of a cryostat.

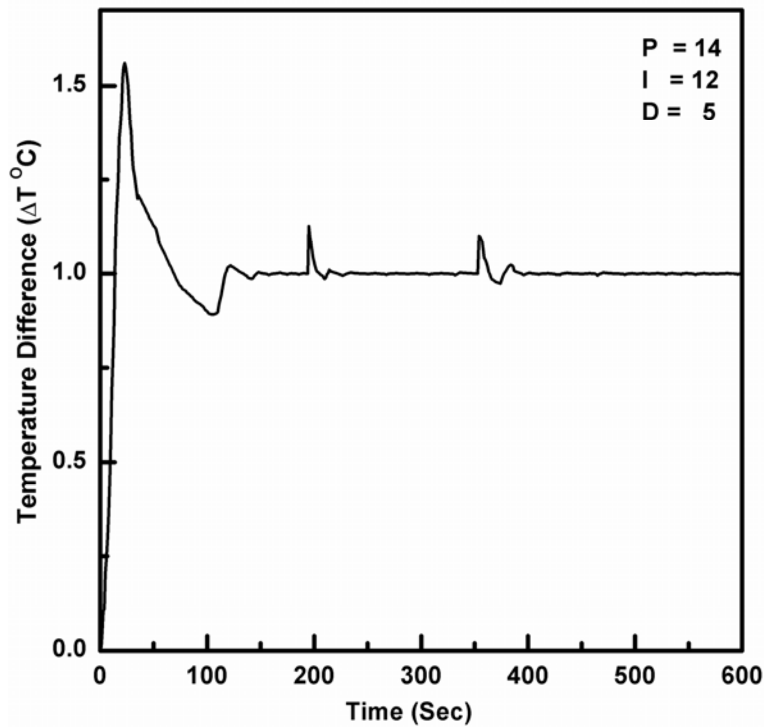

Fig 3.13. Thermopower setup at room temperature open to atmosphere

Then the setup is initially checked for a set temperature difference of 1°C for more than an hour. The PID values are optimised and set up program is allowed to run and the temperature difference between the blocks is seen to be between 1.005 °C and 0.995 °C after the initial increase to 1.2 °C figure 3.14. The temperature difference is maintained well with both heaters.

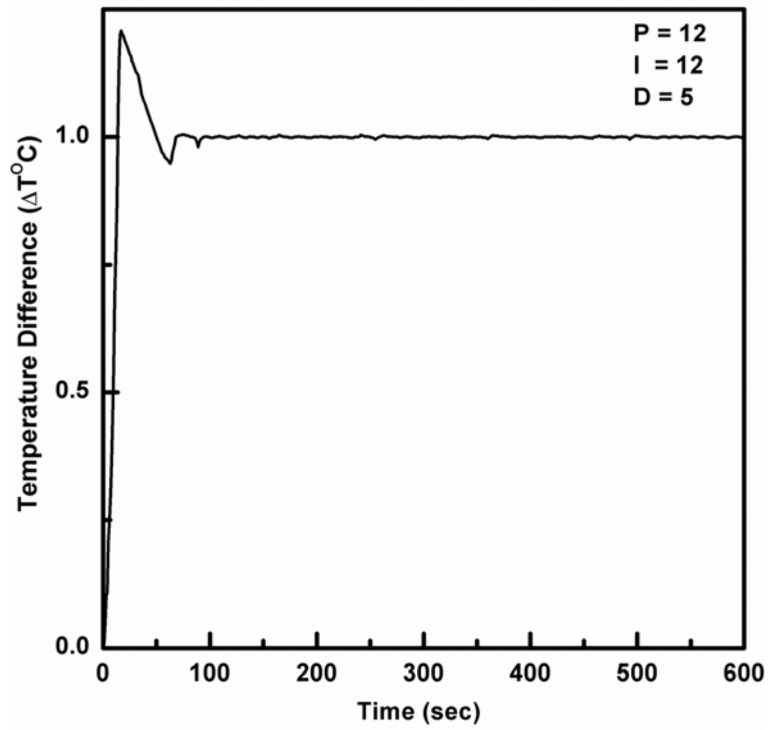

Figure 3.14 Thermopower setup mounted on cold finger of cryostat.

The thermopower of copper sheet was measured and is shown in figure 3.15. The value obtained 1.73 μ V K^{-1} is in close agreement with the reported value of thermopower for copper[3] (1.71 μ V K^{-1}). Thermopower of ZnO:Al thin films were measured and the Seebeck coefficent is found to be -1.44 mVK^{-1} for the ZnO:Al thin film sample.(fig 3.16)

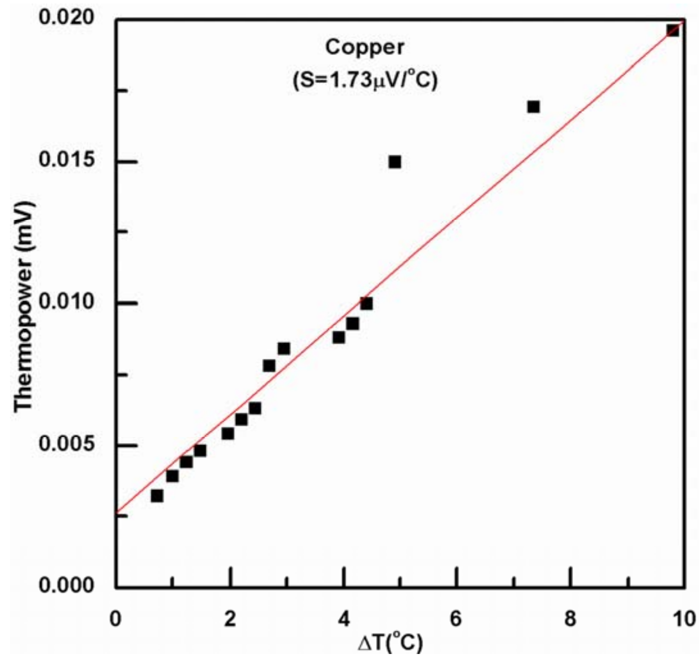

Fig 3.15. Thermopower of copper sheet

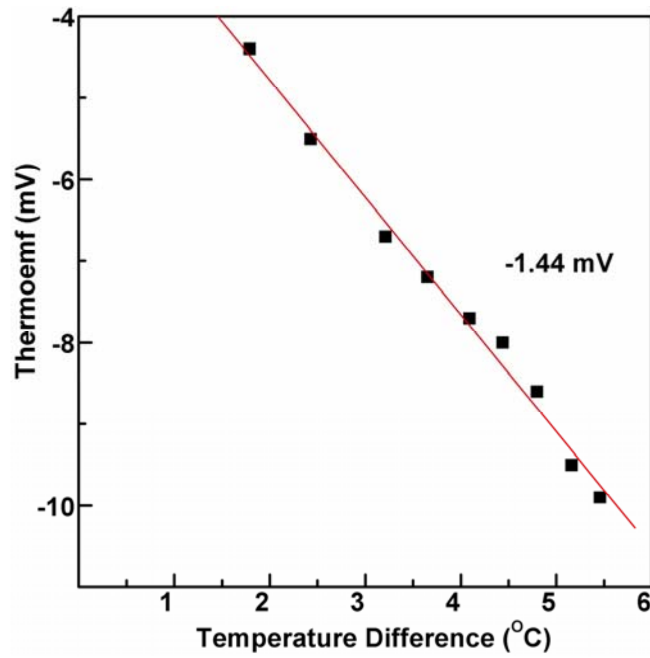

Fig 3.16. Thermopower of ZnO:Al thin films

3.4. Conclusions

A setup for the measurement for the thermopower was fabricated. The process controller program was found to be working satisfactorily. The setup was standardised by measuring the thermopower of copper sheet. The measured value of the thermopower is in close agreement with that of the reported value of copper.

3.5. References

[1.] D.L.Young and T.J.Coutts and V.I. Kaydanov, Review of Scientific instruments **71** (2000) 462.

[2.] J.Yeager and M.A. Hrusch-Tupta, Low level measurements,Precision dc Current,Voltage and Resistance measurements, 5th Ed. Keithley Instruments Inc. Cleveland, 1997.

[3.] A S Karolik, J. Phys.: Condens. Matter **13** (2001) 1093.

Chapter 4

Characterisation Of Pulsed Laser Deposited Zinc Oxide Thin Films

Thin films of aluminium doped ZnO have been deposited on polymer and quartz substrates at room temperature by pulsed laser deposition (PLD) technique. The influence of the deposition parameters such as substrate temperature, oxygen pressure on the properties of the PLD grown films have been studied. Structural, optical and electrical properties of the thin films are analysed. All the films grown under optimised conditions are optically transparent, electrically conducting and c-axis oriented. The ZnO:Al films were also grown on quartz substrate at higher substrate temperatures. The oxygen pressure required for the growth of crystalline thin films decrease as the substrate temperature increases.

4.1. Introduction

The aluminium doped ZnO thin films are widely being studied for the use of transparent conducting electrodes. Al doped ZnO thin films are used as transparent electrodes in solar cells since with the wide bandgap (~3.2eV) ZnO is solar blind [1–4]. The stability of ZnO makes it suitable for space applications [5]. Thin films of ZnO are used as electrode material for photodetectors [6], and they exhibit good piezoelectric and optical properties. Due to its unique conducting mechanism based on oxygen vacancies, ZnO has been used to fabricate oxygen gas sensors [7]. The strong spontaneous and stimulated emissions by excitons even at room temperature in ZnO make it attractive for fabrication of light emitting diodes (LED) and Laser diodes (LD) [8,9].

The techniques for the growth of high quality p –type ZnO thin films [10–12] have been progressing in the last few years. Codoping with Al, In or Ga along with nitrogen in ZnO results in p type conductivity. Al doped ZnO has been used as the transparent electrode in organic electroluminescent devices (OLED). Deposition of good quality ZnO thin films at lower temperature make ZnO more attractive than the indium tin oxide electrodes for the application of OLEDs [13, 14]. Most of the methods for the growth of ZnO thin films, such as sol-gel synthesis [15], chemical vapour deposition [16], metal organic chemical vapour deposition [17], Molecular beam epitaxy [18] and pulsed laser deposition (PLD) [19] use high substrate temperature for obtaining good quality films. Table 4.1 gives a brief review of the temperatures and methods of preparation of ZnO thin films by different workers.

For the full exploitation of the attractive properties of ZnO, high quality c axis oriented ZnO has to be grown at low substrate temperature. Growth of crystalline films depend on the energy of the adatoms, for the adatoms reaching the substrate need to move on the substrate surface for proper orientation, this can be achieved either by increasing the temperature of the substrate or increasing the energy of the adatoms.

Table 4.1: Conditions for the growth ZnO thin films prepared by various methods.

Growth Technique	Substrate Temperature (^oC)		Background gas	Post deposition heat treatment	Reference
P.L.D	600	10^{-4} –10 mbar	O_2, N_2O	–	20
P.L.D	700	10^{-4} –10 mbar	N_2	–	20
P.L.D	200–800	10.13 mbar	O_2	–	21
MoCVD	200–500			500°C for 10 minutes	22
Rf Sputtering	350–750	>0.2 mbar		RTA 800°C	23
P.L.D (on Al_2O_3 and NaCl Substrates)	RT– 500	0.013 mbar	O_2		24
P.L.D	200–500	6.67 X 10^{-6} mbar& 0.027 mbar	O_2		25
P.L.D	750	0.133X10^{-3} – 1.33 mbar	O_2		26
P.L.D	300–800	0.133X10^{-3} – 0.13 mbar	O_2		27
Sol–Gel	400			450 – 550	28
CVD	50 – 250	Dimethyl Zinc, H_2O, Triethylaluminium			29
Spray Pyrolysis	400		Flow of N_2	200 – 300	30
MBE	400		H_2O vapour & O_2		31

The energy of adatoms in thermal evaporation technique has energy 0.1eV whereas adatoms in PLD have about 100eV. Thus PLD would be an ideal choice for attempts to grow crystalline films at low temperatures. In this chapter the growth and characterisation of polycrystalline ZnO films deposited by PLD is described.

4.2. Experimental

The aluminium doped zinc oxide thin films were prepared by pulsed laser ablation of the ZnO:Al (2wt% Al doped ZnO) target. The ZnO:Al targets were prepared from the 99.99% pure ZnO and aluminium oxide powder. The ZnO and Al_2O_3 powders were mixed with agate mortar and pestle. The powder was pressed and sintered at 900^0C for 10 hours in air. To obtain highly conducting and transparent crystalline ZnO:Al thin films, the deposition conditions such as substrate to target distance, oxygen pressure, substrate temperature were optimised. ZnO:Al films were deposited using the second harmonics (532 nm) of Nd:YAG laser (Spectra Physics INC,GCR 150), with pulse width of 6-7 ns at a repetition rate of 10 Hz. The laser beam was focused using a spherical convex lens on to the target at an angle of 45°. Target was rotated during laser ablation in order to avoid the formation of craters. The films were also grown by the third harmonics of Nd.YAG (λ=355 nm) with pulse energy of (~ 2.7 J/cm^2). The optimised growth conditions such as oxygen pressure and substrate to target distance does not appreciably depend on changing the wavelength from 532 nm to 355 nm. However a faster growth has been obtained on ablating with the 355 nm than 532 nm for the same energy density. Moreover the surface morphology of the films becomes smoother when the deposition is carried out using the third harmonics for ablation. The films were grown without any intentional heating of the substrate at various oxygen pressures on fused quartz, Polyimide and Polyethylene terathalate (PET) substrates. The substrate to target distance was increased from 3.5 cm in steps of 0.5 cm up to 6 cm. The films were also grown on fused quartz at higher substrate temperatures.

The thicknesses of the films were measured using Vecco Stylus profilometer. The thicknesses of thin film grown with 532 nm line were approximately 1000 A^o and that of the films grown with the 355nm line were approximately 1200 A^o. The structural analyses of the films were carried out using a Rigaku X–ray diffractometer with Cu Kα line in the $\theta - 2\theta$ geometry. The resistivities of the films were measured using the two probe method with a Keithley's source measure unit (SMU 236). The optical

transmissions were recorded using Jasco uv-vis-nir spectrophotometer. The excitation and emission spectra of the samples were recorded using the spectrofluorometer (FlouroMax-3).

4.3.A Deposition Of Aluminium Doped Zinc Oxide Thin Films At High Temperatures.

The deposition parameters such as the laser energy, substrate to target distance, substrate temperature, and oxygen pressure were initially optimised. ZnO:Al films were deposited at laser fluence of 2.2 J/cm^2 at 532 nm. At lower energies the growth rate of the film is very low. The substrate to target (S–T) distance was fixed at 5 cm for ablation with 532 nm. The films deposited at S–T distances below 5 cm were dark brown to black in colour and were amorphous in nature by the X–ray analysis. The growth rate of films deposited at S–T distances above 5cm was very low hence S–T distance was fixed at 5cm.

The films grown under high vacuum (2x10^{-6} mbar) at room temperature were amorphous. The films prepared under high vacuum at substrate temperatures up to 300 ^{o}C were also amorphous as indicated by the X-ray diffraction (XRD). The typical X–ray pattern of amorphous film is shown in figure 4.1.

The growth of crystalline ZnO by PLD requires a Zn:O ratio closer to one [32]. A background oxygen pressure is required to interact with and compensate the excess of Zn in the ablated plume. Prasad et. al. [33] reports that films grown even in the presence of O_2 background pressure were oxygen deficient. Though the films grown in vacuum($ZnO_{0.75}$) were more deficient than those grown in presence of 5 m torr ($ZnO_{0.95}$) O_2 gas, none of the films were stoichiometric.

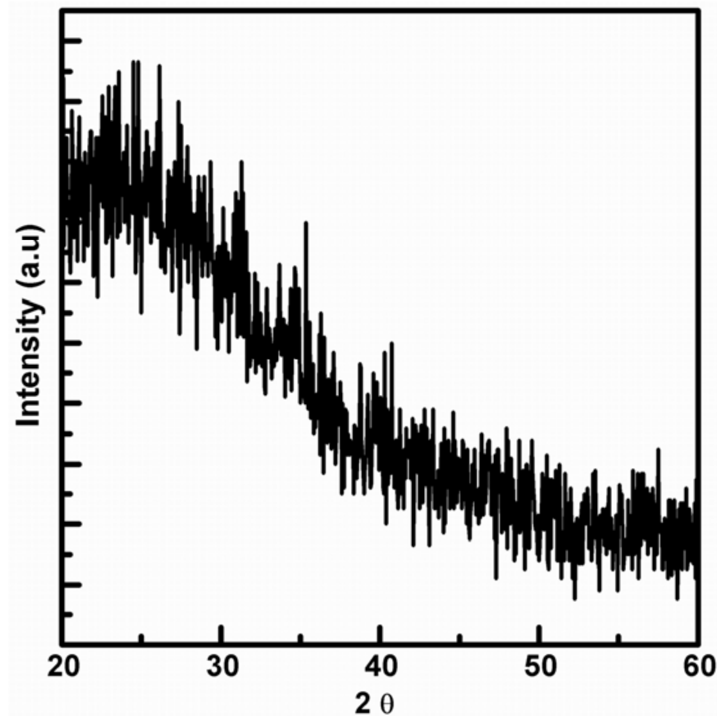

Figure 4.1: Typical XRD pattern of amorphous ZnO:Al thin films grown by PLD.

In order to understand the growth mechanisms and the plasma parameters affecting the film growth, the plasma plume was studied by the optical emission spectroscopic technique (OES). The target and chamber are kept at ground potential. The plume emanating from the target surface is focused using a spherical lens (f = 50 mm) kept inside the chamber so as to collect maximum flux, onto an optic fiber bundle. The other end of which is optically coupled to the entrance slit of a monochromator (Spex 320, Jobin Yvon, 1200 grooves/mm grating, 0.06nm spectral resolution). The imaging of the spectrum is done by a CCD (Spectrum One 2000, 1024×256 pixels), which is coupled to the exit slit of the monochromator. The spectra of the plume were taken in vacuum (~10^{-6} mbar) and also in three different ambient gas (oxygen) pressures. The optic fiber bundle was moved along the direction of propagation of the plume (Z-axis) from the target surface to a distance of 20mm using an x-y translator having an accuracy of 1μm. The

CCD was triggered externally using a voltage pulse from the output of the laser controller so as to ensure that the investigation of the plume was carried out at specific time delays after the laser pulse has impinged onto the target. The CCD is interfaced with a PC using GPIB cable for storage and subsequent data processing.

The OES spectra (Fig 4.2) show strong emission lines of neutral Zn, Zn^+ and neutral oxygen.

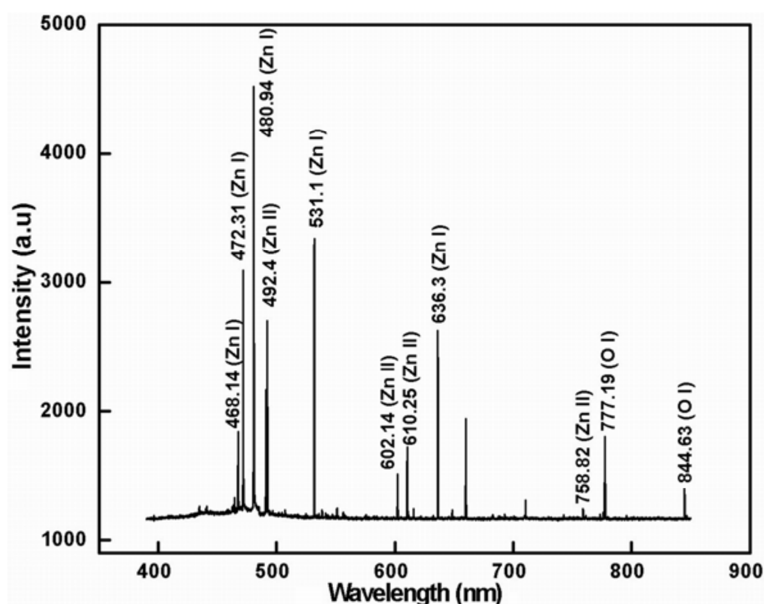

Figure 4.2. Optical emission spectrum of the plume produced by laser ablation of ZnO:Al target with frequency tripled Nd:YAG Laser**.**

The integrated emission intensity as a function distance from the target surface for oxygen (OI) 844nm is shown in figure 4.3. The integrated intensity has been obtained by integrating the whole area under the emission profile, which gives an indication of the amount of excited species in the plume reaching at a given distance. In the presence of oxygen background pressure the intensity of OI, Zn and Zn^+ picks up with distance from the target surface and then shows an exponential decrease. While without any

oxygen background pressure the oxygen and Zn neutral species are very small as evident from the integral intensity.

The plasma contains more Zn^+ ions in vacuum than in the presence of oxygen background pressure. The ZnO:Al target pre and post ablated surface was analysed by SEM and energy dispersive X–ray (EDAX). This also indicates that the surface of ZnO:Al target after ablation under vacuum is highly Zn rich than the pre-ablated and those ablated in oxygen background. The Zn rich target and the low oxygen in the plasma, when the deposition is carried out in vacuum result in the Zn:O ratio deviating from 1:1 stoichiometry which is essential for the growth of crystalline films.

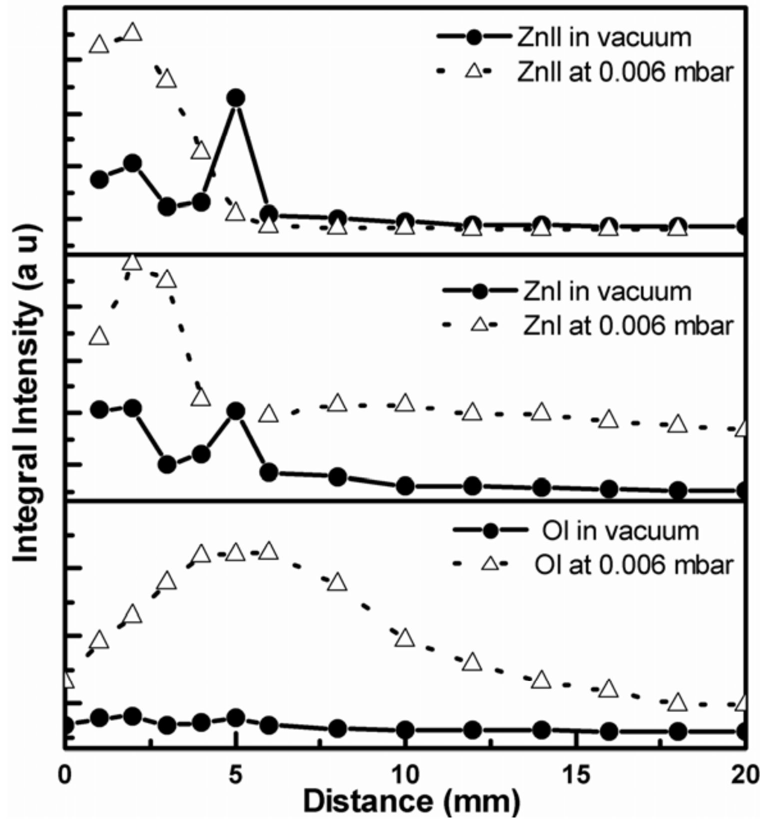

Figure 4.3. Variation of integral intensity of atomic species with distance from the target surface.a) oxygen neutrals b) zinc neutrals and c) Zinc ions.

Thus films grown at high vacuum are not stoichiomertic and are hence amorphous. The ZnO:Al films were grown on quartz substrates at various substrate temperatures keeping the substrate to target distance (5 cm) and laser fluence of 2.2 J/cm^2. Keeping the substrate temperature fixed, the films were grown at various oxygen pressure. The films were crystalline only for a particular O_2 pressure (fig 4.4). The pressure required for the growth of crystalline ZnO was found to decrease with increase in temperature i.e. the films were crystalline at high temperature and low oxygen background.

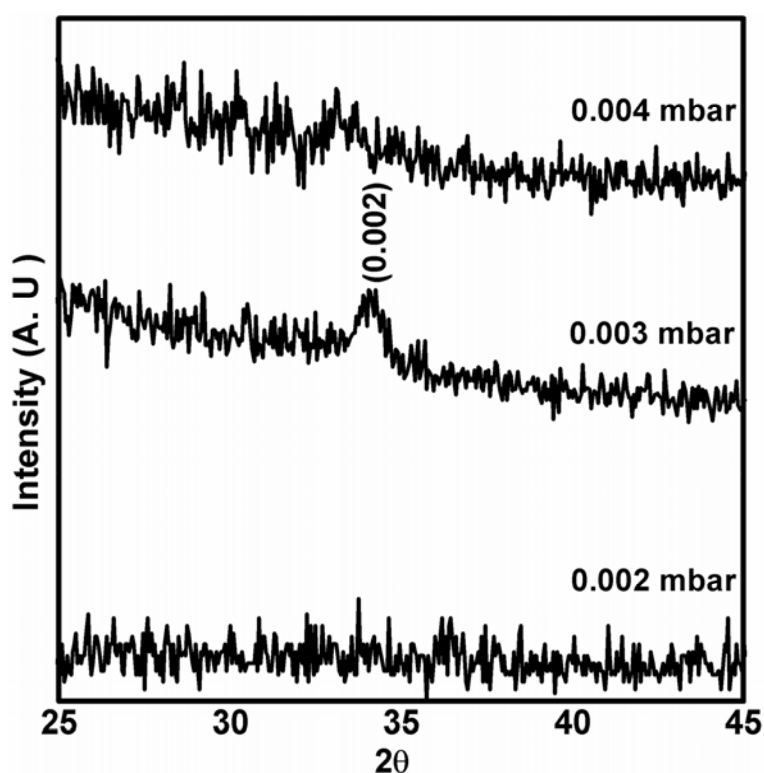

Figure 4.4. XRD pattern of films grown at 50^{0}C at various O_2 pressures.

The higher substrate temperature may give additional energy to the adatom especially to the neutral Zn. This may increase the reactivity of neutral Zn with oxygen forming ZnO. Thus the higher substrate temperature requires only low oxygen pressure. The best crystalline film or epitaxial film has been reported to be obtained at substrate temperatures 700^{0}C and above. The oxygen pressures used by various workers for the growth of films vary

from 10 m torr to 10^{-5} torr. The difference in oxygen pressure has been suggested due to the pressure distance scaling law in PLD [21]. In the present study it has been observed that the oxygen pressure required for the growth of crystalline film not only depends on target to substrate distance but also on substrate temperature. There exists a pressure temperature scaling in PLD for fixed target to substrate distance. The inability to grow crystalline films at high vacuum at room temperature could be due to the fact that the high energy of the adatoms in ablated plume are knocking out the deposited atoms from the substrate. The oxygen introduced into the chamber increases the collisions of ablated species and thus reduces the energy of the ablated species and facilitates the oriented growth. Too much oxygen however would reduce the energy of the species very much that they would not be able to move on the surface of the substrate to positions of least energy. Thus there is an optimum pressure required for growth of crystalline thin films at a particular substrate temperature

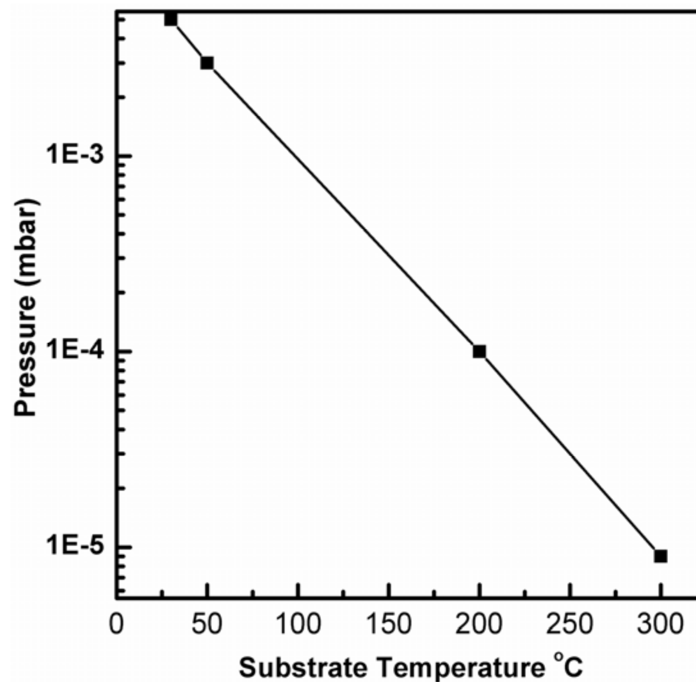

Figure 4.5. Optimum oxygen pressure required for growth of crystalline ZnO:Al thin films at various substrate temperature (S – T of 5 cm.)

The oxygen background pressure required for the growth of crystalline film decreases as the substrate temperature increases (Fig.4.5). The control of oxygen pressure for the growth of crystalline films becomes very critical at higher substrate temperatures. For example crystalline films deposited at a substrate temperature of 300 ^{0}C requires low oxygen ambient of $9x10^{-6}$ mbar and a slight variation in oxygen pressure result in amorphous films while crystalline films have been deposited at an oxygen pressure ranging from 0.003 mbar to 0.007 mbar when the substrates were not heated. The resistivity of the ZnO film decreases with the substrate temperature. (Fig 4.6) The lowest resistivity of 1.62 X 10^{-3} Ω cm^{-1} could be obtained for films grown on quartz substrates at an oxygen pressure of 1 X 10^{-4} mbar and substrate temperature of 200 ^{o}C. The variation of FWHM and resistivity with substrate temperature is shown in figure 4.6.

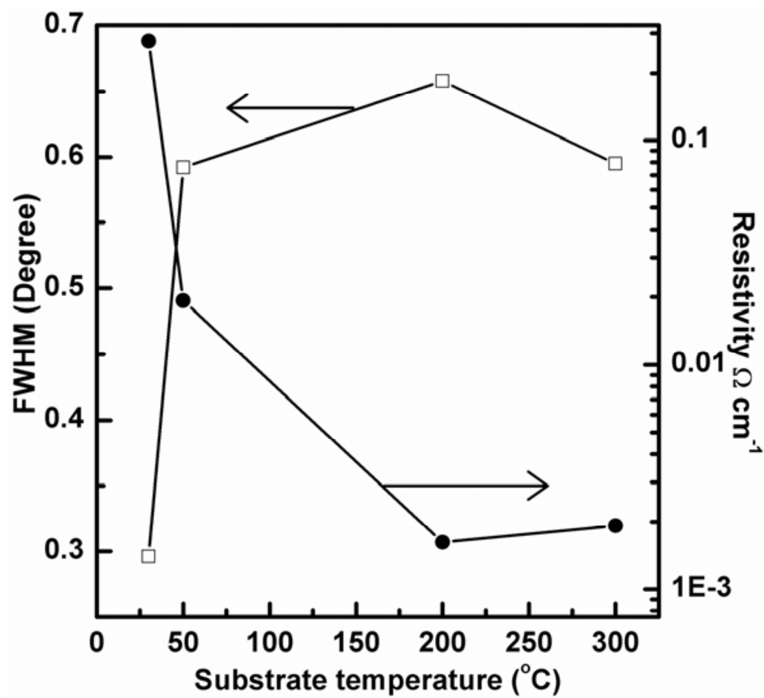

Figure 4.6. The variation of FWHM and resistivity with substrate temperature of ZnO:Al thin films

The FWHM shows an increase up to 200 °C and then slightly decreases. This may be due to the evaporation of zinc and/or oxygen atoms from the substrate surface at higher substrate temperatures. The resistivity also is decreasing upto 200 °C and then slightly increasing.

The bandgap of the ZnO:Al films grown at different substrate temperature is found to increase with substrate temperature (Fig 4.7). The bandgap is found to be higher than that reported for the stochiometric ZnO. The increase in bandgap may be related to the Burstein Moss (B–M) shift [34]. The B–M shift is proportional to the carrier concentration. There is a decrease in resistivity as the substrate temperature increases which also support the fact that there is increase in carrier concentration.

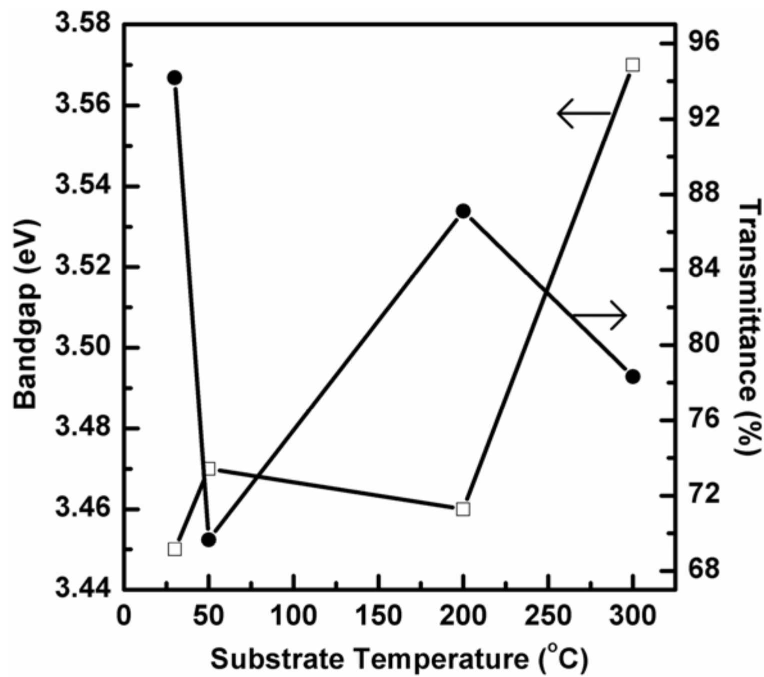

Figure 4.7. The variation of transmission (at $\lambda = 550$ nm) and bandgap with substrate temperature of ZnO:Al thin films.

PL emission was studied with the spectrofluorometer Flouromax–3. 285 nm was used to excite the samples and 15 seconds integration time was given to make sure that sufficient signal was picked up by the detector. The input slit of the PMT was set as 1.5 nm and output slit of the PMT were set to 3 nm. The PL spectrum obtained for a bare quartz substrate is shown in figure 4.8.

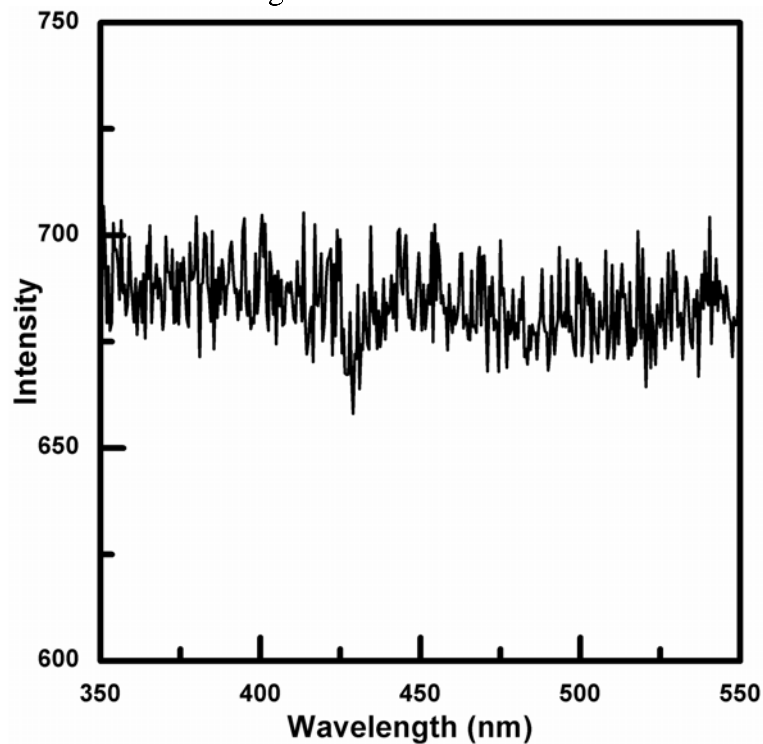

Figure 4.8. PL Spectrum of bare quartz substrate.(λ_{ex} = 285nm)

The typical PL spectrum of ZnO:Al thin films is shown in figure 4.9. There are mainly three different lines in the spectrum one is at 389 nm(3.19 eV) in the UV region, another at 468.5 nm (2.67) in the blue region and the third one at 543.5 nm(2.29 eV) in the green region.

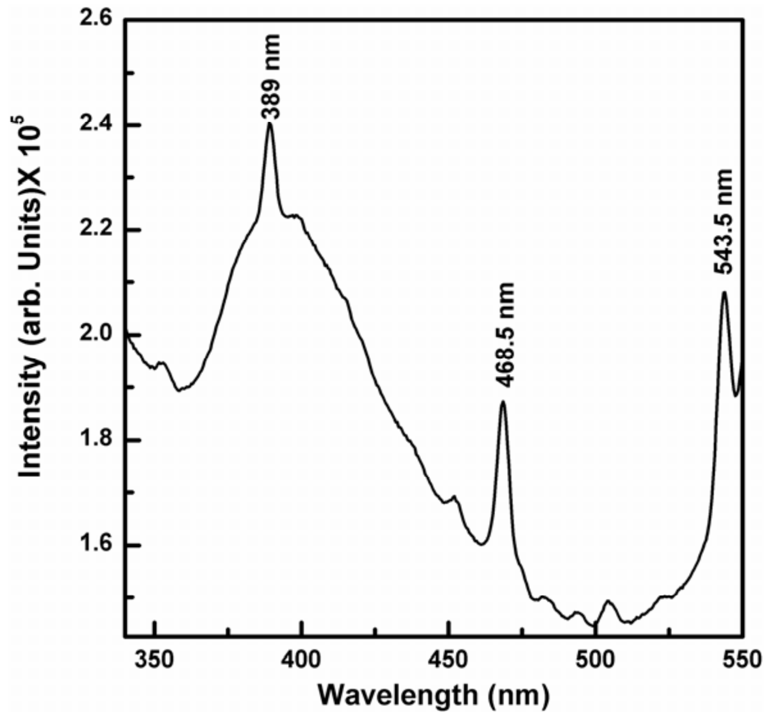

Figure 4.9. Typical PL spectrum of ZnO:Al samples

The ultraviolet photoluminescent emission (3.19 eV) from the ZnO:Al target and the films grown on quartz and PET is the characteristic recombination emission due to the exciton transition from localised level below the conduction band to the valance band [35]. The formation of localised level below the conduction band is related to the breaking of lattice periodicity, in the present case the Al^{3+} ions replacing the zinc can generate these localised levels. The PL emissions at higher wavelengths are related to the defects such as oxygen vacancies and imperfections of crystalinity due to the low temperature of formation [36].

The blue emission of the PL is generally attributed to the oxygen vacancies, since the oxygen vacancies can produce two defect donor level located at 1.3 –1.6 eV below the conduction band and 0.3–0.5 eV. The energy interval

from the shallow donor level to the top of the valence band is about 2.8 eV [36].

The green emission (2.29 eV) observed in the PL emission spectra is smaller than the bandgap energy of ZnO film, which is found to be 3.3 eV. The green emission must be related to local level in the bandgap. The recombination of singly ionised oxygen vacancy electrons with photo-excited holes in the valence band would result in the green emission [37].

The analysis of the PL spectra is carried out by taking the ratio of the area under the gaussian fits of emission lines at uv (389 nm) to the area under the emission at blue line (468.5 nm) or the area of the gaussian fit of the area under green line (543.5 nm.). Thus a large ratio means that the emission at uv is higher than the emission at blue or green.

The analysis photoluminescence spectra show that the uv emission is maximum for the room temperature deposited films at high oxygen pressure. The variation of resistivity and the ratio of PL intensity of uv to green emission with substrate temperature is shown in figure 4.10.

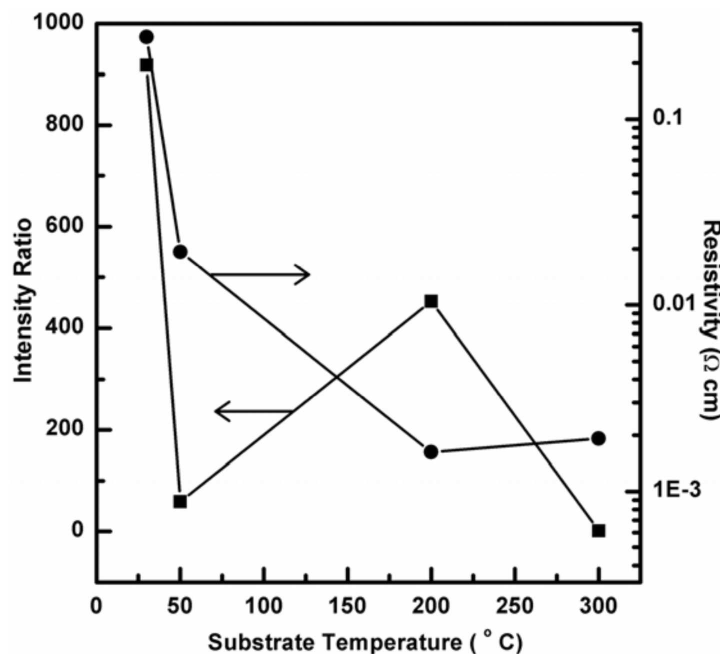

Figure 4.10. The variation of resistivity and the ratio of PL intensity of uv to green emission with substrate temperature of ZnO:Al thin films.

4.3.B Deposition Of Aluminium Doped Zinc Oxide Thin Films At Room Temperature.

Polycrystalline films were obtained on depositing the films at room temperature with a laser fluence of around 2.2 J/cm^2 at 532 nm. The substrate to target distance was fixed at 5 cm for ablation with 532 nm. The oxygen pressure was varied from 0.003 mbar to 0.008 mbar. Figure 4.11 shows the XRD pattern of the ZnO:Al film grown on glass substrates at room temperature at various oxygen pressures.

The variation of full width at half maximum (FWHM) of the (002) peaks of the ZnO:Al thin films with the oxygen pressure is shown in figure 4.12. The crystalinity of the films are found to increase with oxygen pressure upto 0.005 mbar and then there is increase in FWHM of the (002) peak with increase of pressure. This could be due to the variation in stoichiometry of the films. At very low oxygen pressures, the oxygen adatoms would be escaping from the substrate surface while at higher oxygen pressures, they

would find it more and more difficult to reach the substrate since the collisions with oxygen molecules would increase substantially.

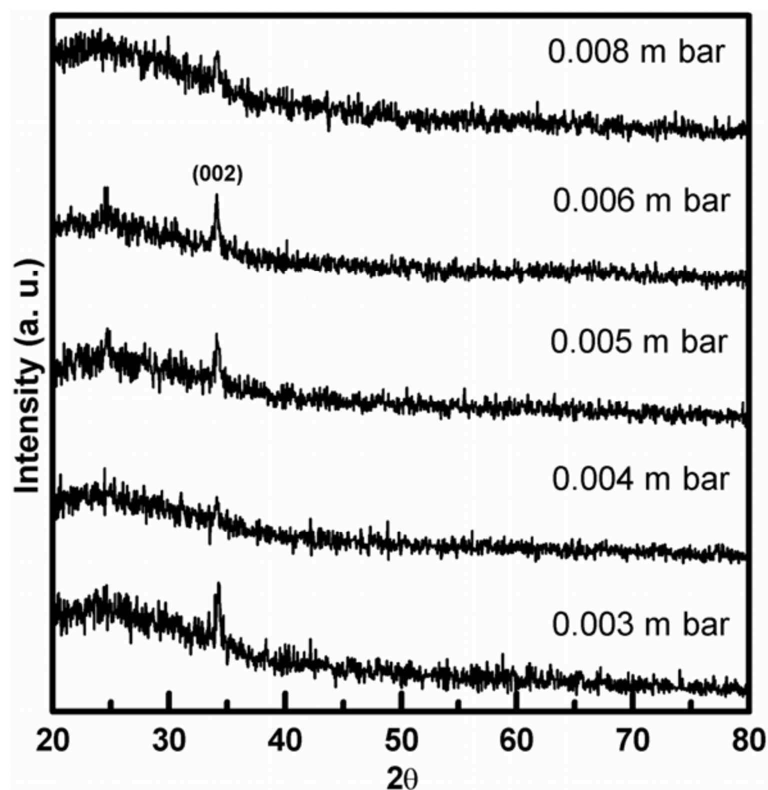

Figure 4.11. XRD pattern of the ZnO:Al film grown on glass substrates at room temperature at various oxygen pressures.

In the present study, an oxygen pressure of 0.005 mbar is found to be the optimum for growth of highly crystalline ZnO:Al thin films at room temperature by PLD. Depositing the ZnO:Al thin films by ablating with 532 nm and 355 nm, there was not much difference in the quality of the films produced.

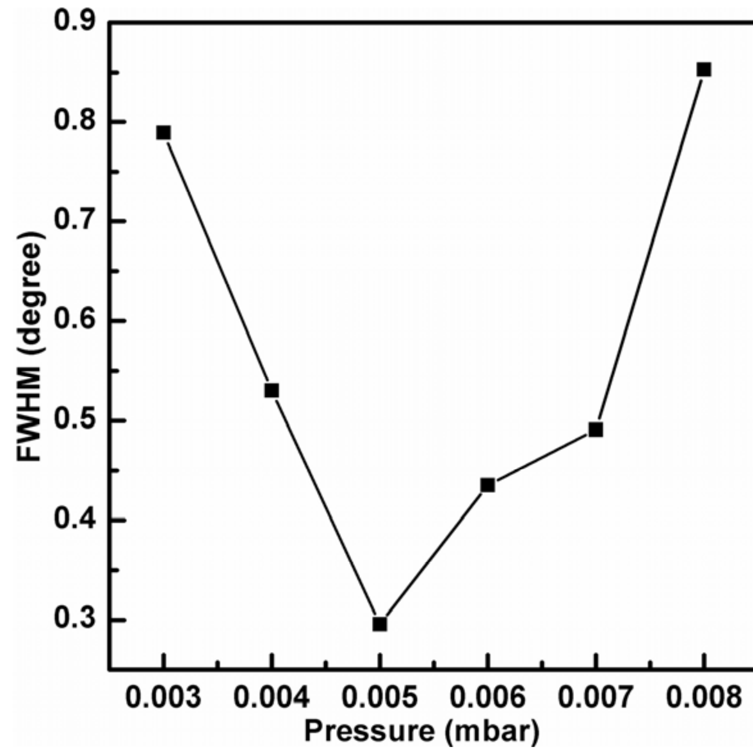

Figure 4.12. Variation of FWHM with oxygen pressure of ZnO:Al thin films grown at room temperature.

The surfaces of the thin films were smoother when the ablation was carried out using third harmonics of Nd:YAG (355nm) (fig 4.14). The atomic force micrographs of thin films deposited by ablating with third harmonics show that they have an average roughness of 9.76 nm (figure 4.14). Thin films deposited by ablating with second harmonics (532 nm), have an average roughness of 16.19 nm. (fig. 4.13).

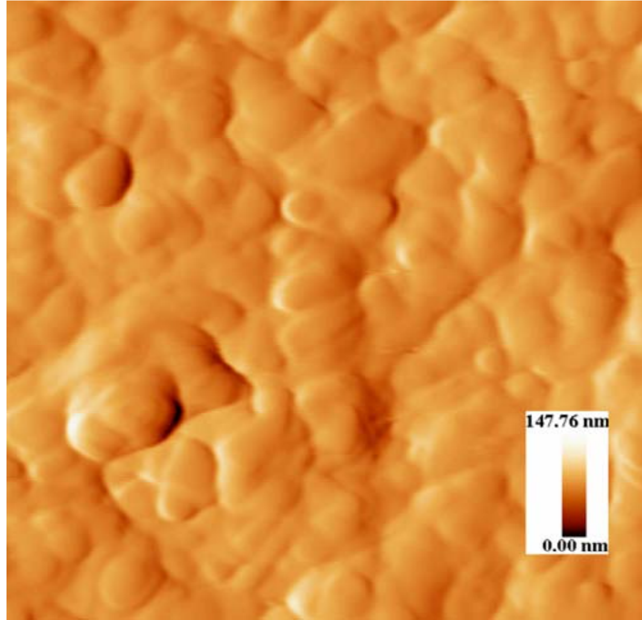

Figure 4.13. AFM picture of ZnOAl thin films grown by ablating with second harmonics (532 nm) of Nd:YAG laser at room temperature.

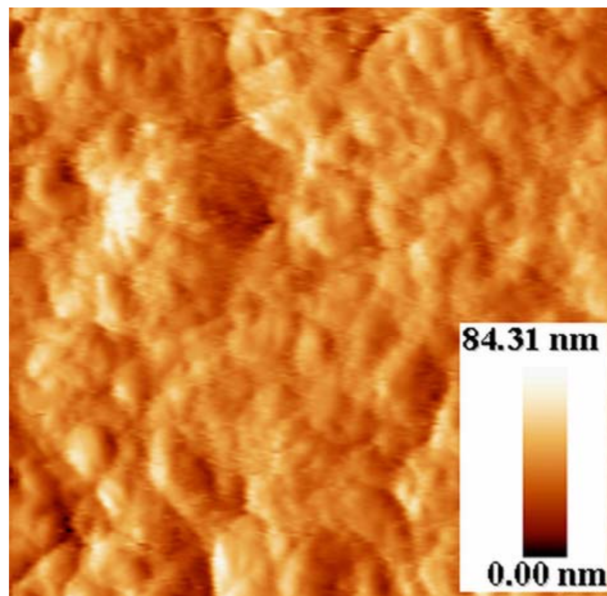

Figure 4.14. AFM picture of ZnOAl thin films grown by ablating with third harmonics (355 nm) of Nd:YAG laser at room temperature.

Thin films of ZnO:Al were also grown on flexible plastic substrates. The ablation was carried out using the frequency tripled (355 nm) Nd:YAG laser at the fluence of 2.7 J/cm^2. The substrate to target distance was 6 cm. Polyimide and Polyethylene terathalate (PET) were used as substrates and ZnO:Al thin films were grown at room temperature. Oriented ZnO:Al thin films could be grown on both types of plastics. Figure 4.15 shows the XRD pattern of ZnO:Al thin films grown on polyimide substrates.

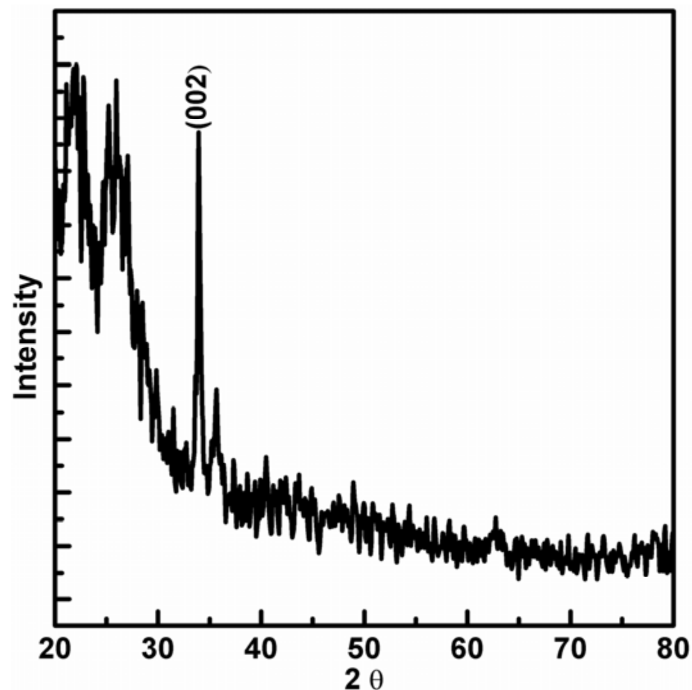

Figure 4.15. XRD pattern of ZnO:Al thin films grown on Polyimide substrates at room temperature.

Figure 4.16 shows the XRD pattern of the of ZnO:Al thin films grown on PET substrates. FWHM of 0.266^o could be obtained for films grown on PET substrates. Which is comparable to the FWHM of 0.296^o obtained for films grown on quartz substrates with 532 nm line of Nd:YAG at room temperature.

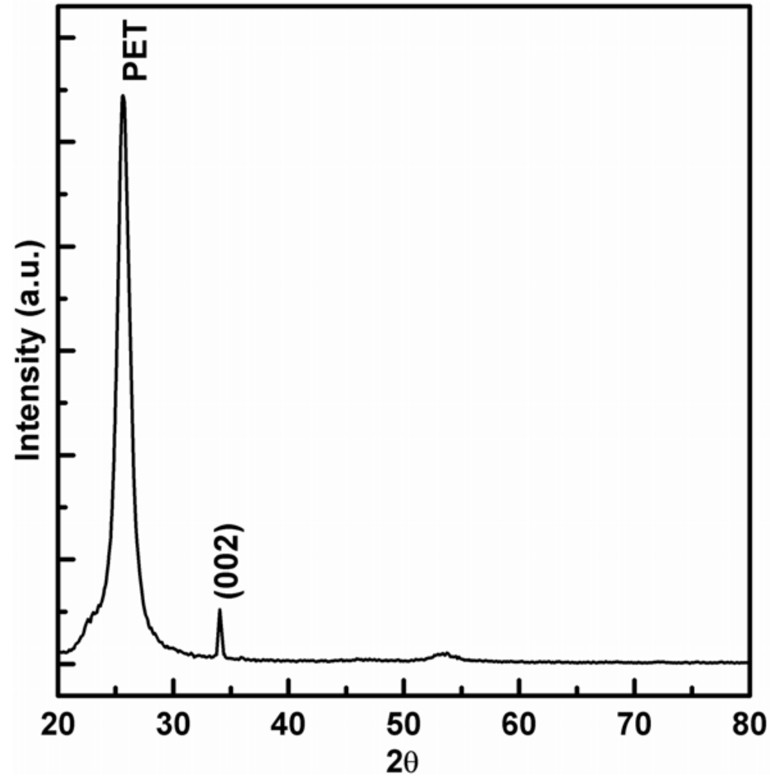

Figure 4.16. XRD pattern of ZnO:Al thin films grown on PET substrates at room temperature.

The films were amorphous by X–ray diffraction when grown at room temperature at pressure below 0.003 mbar or above 0.008 mbar. A minimum full width at half maximum (FWHM) for the (002) peak for the films grown at room temperature was observed at an oxygen pressure of 0.005 mbar (fig 4.12.). The variation of resistivity and FWHM of (002) diffraction peak with oxygen pressure is shown in figure 4.17.

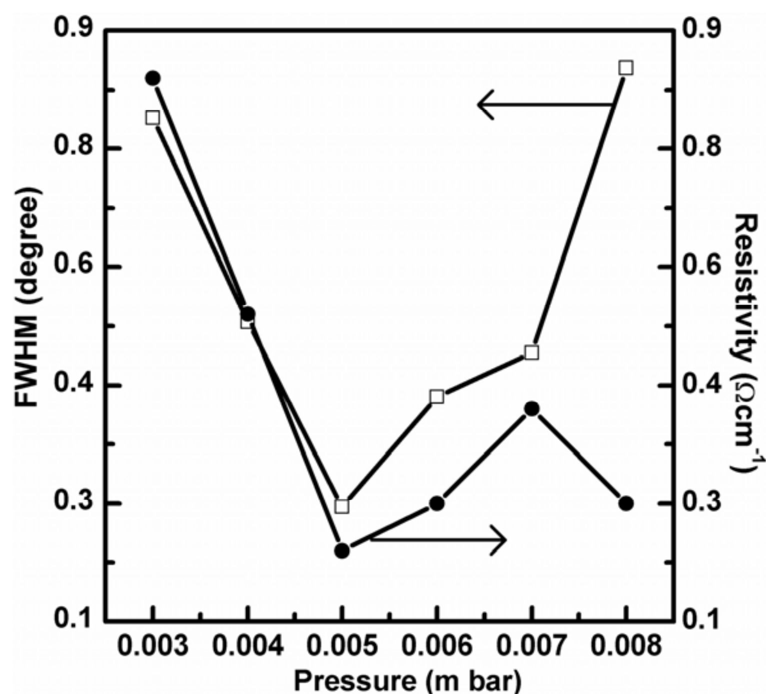

Figure 4.17. The variation of resistivity and FWHM with oxygen pressure of ZnO:Al thin films grown at room temperature

The dependence of resistivity of the ZnO:Al films on the oxygen pressure can be related to the crystallinity of the films. The FWHM of the diffraction peak is a measure of the size of crystallites. Good crystallinity leads to lower resistivity because of less grain boundary scattering. The resistivity of the film grown at 0.005 mbar is minimum (2.76×10^{-1} Ω-cm)

The films grown on quartz and PET substrates are highly transparent (>85%) in the visible region. The polyimide substrate, which is coloured, absorbs radiation below 500 nm and the transmission above 550 nm is about 60% (Fig 4.18). The transmissions of the all other films are above 85%. The optical bandgap was evaluated from the transmission spectra.

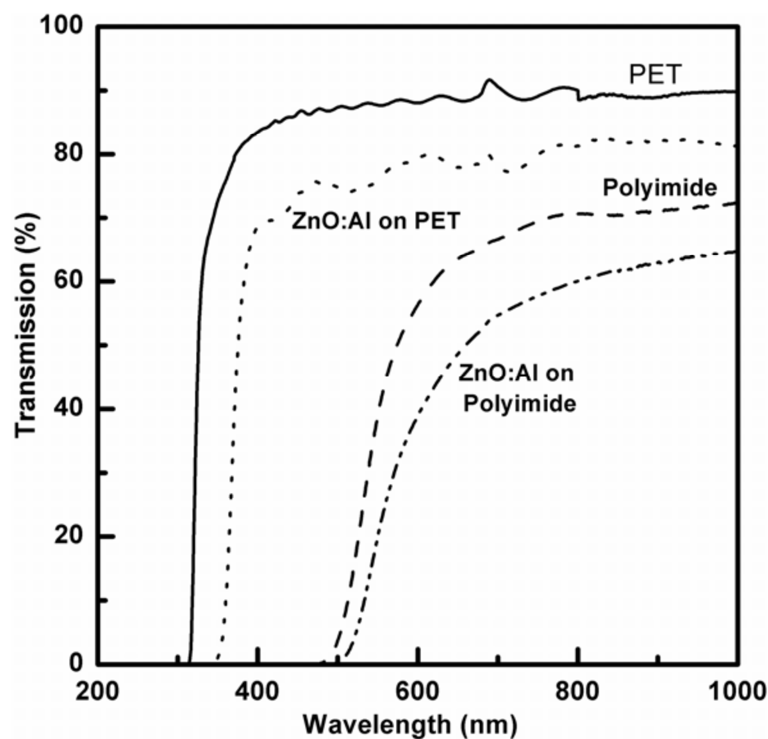

Figure 4.18. Transmission spectra of ZnO:Al on PET and Polyimide substrates and bare substrates.

The absorption coefficient α was evaluated using the measured value of thickness of the film using the relation $I = I_o e^{-\alpha t}$. The band gap of the ZnO:Al films were calculated from the transmission spectra by assuming a parabolic band structure for the material, the absorption coefficient and band gap can be related by the expression $\alpha h\nu = A(h\nu - E_g)^{1/N}$ where E_g is the band gap energy and α is the absorption coefficient corresponding to frequency ν [38]. The constant N depends on the nature of electronic transition. In the case of ZnO:Al films N is equal to 2, for direct allowed transition. The direct bandgap of ZnO:Al thin film was estimated by potting $(\alpha h\nu)^2$ vs $h\nu$ and extrapolating the linear portion near the onset of absorption edge to the energy axis. A typical plot is shown in figure 4.19.

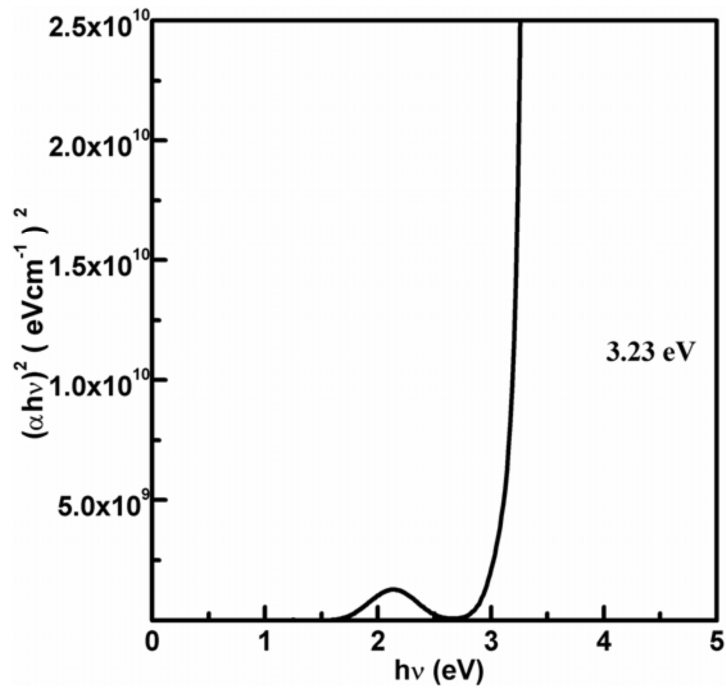

Figure 4.19. Typical plot of $(\alpha h\nu)^2$ vs hν of ZnO:Al thin films grown on quartz substrates.

Typical transmission spectra of ZnOAl thin films grown on quartz substrate is shown in figure 4.20.

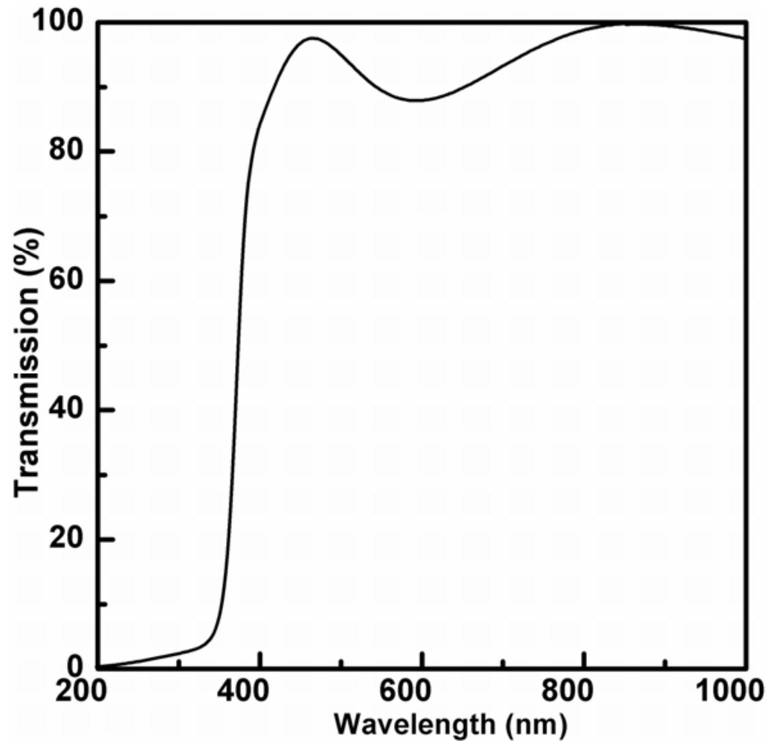

Figure 4.20. Typical plot of transmission spectrum of ZnO:Al thin films grown on quartz substrates.

The transmission and bandgap are maximum for films grown at 0.005 mbar oxygen pressure. The bandgap is found to increase with decrease of oxygen partial pressure. This can be related to the Burstein Moss shift [34]. The lower oxygen partial pressures result in more oxygen vacancies in ZnO films and hence an increase in the carrier concentration. The Burstein – Moss shift is proportional to carrier concentration. Hence there is an increase in the bandgap with decrease in oxygen pressure during PLD. Further decreasing the oxygen pressure results in excess carriers and bandgap narrowing [39]. The variation of transmission and bandgap with the oxygen pressure is shown in figure 4.21.

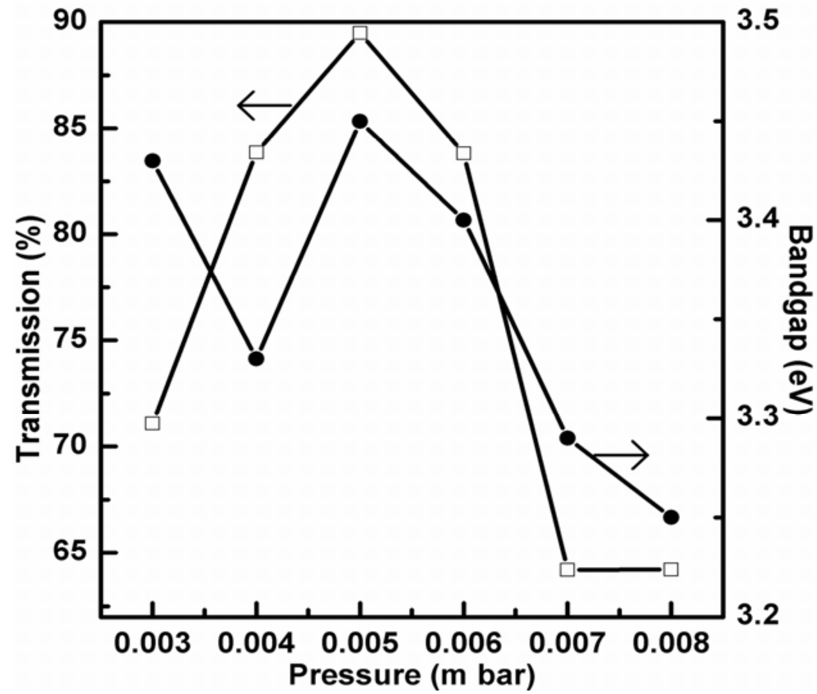

Figure 4.21. The variation of transmission at 550 nm and bandgap with the oxygen pressure of ZnO:Al thin films grown on quartz substrates at room temperature.

Figure 4.22 shows the variation of PL Intensity ratio of 389 nm to 543.5 nm and 389 nm to 468.5 nm for the films deposited at room temperature at various oxygen pressures.

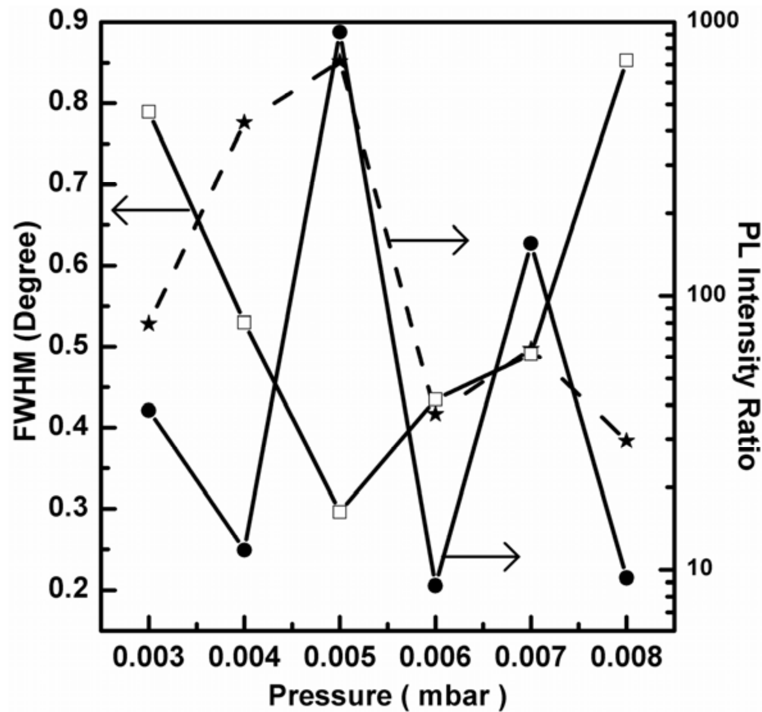

Figure 4.22. Variation of FWHM of X-ray diffraction peak, ratio of PL intensities of 389 nm to 543.5 nm (solid line) and of 389 nm to 468.5 nm (dotted line) with oxygen pressure of ZnO:Al thin films grown at room temperature.

The PL intensity of the 389 nm is maximum for film deposited at oxygen pressure of 0.005 mbar. These films have better crystalinity as evident from the smaller FWHM of X ray diffraction peaks. Better crystalinity is obtained when the Zn:O ratio is nearly stochiometric 1:1 hence the emission at longer wavelength due to oxygen vacancies and imperfections are minimum. Figure 4.23 shows the variation of ratio PL emission intensities of 389 nm/543.5 nm and 389 nm/468.5 nm of the ZnO:Al films grown at various substrate temperature. The PL intensity at 389 nm due to the exciton transition is maximum when the films have better crystalinity.

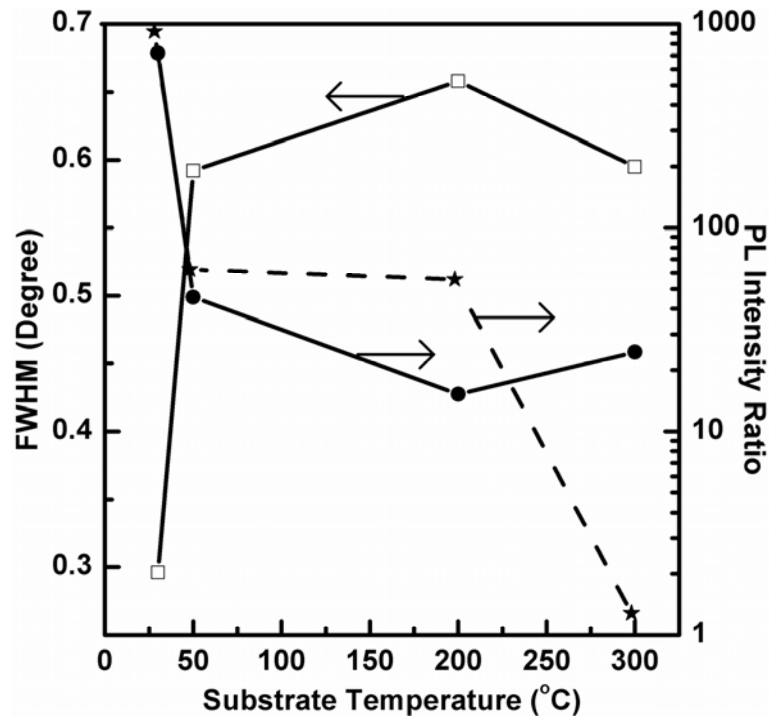

Figure 4.23. Variation of FWHM of X-ray diffraction peak, ratio of PL intensities of 389nm to 543.5 nm (solid line) and of 389 nm to 468.5 nm (dotted line) with oxygen pressure of ZnO:Al thin films as function of substrate temperature.

Table 4.2 summarises the resistivity, transmittance and PL emission of ZnO:Al thin films grown on quartz substrates at 50°C , 200°C and on PET substrate at room temperature.

Table 4.2. Summary of properties of ZnO:Al thin films grown by PLD.

Temperature (^oC)	30	200	30
Substrate	Quartz	Quartz	PET
Pressure (mbar)	0.005	1.00E-04	0.006
Relative PL intensity ratio uv/blue	719.0	128.7	0.42
Relative PL intensity ratio uv/green	917.9	452.6	1.13
FWHM (degree)	0.296	0.658	0.266
Bandgap (eV)	3.45	3.46	3.34
Transmittance at 550 nm (%)	94.2	87.1	85%
Resistivity (Ω cm)	0.276	$1.62X10^{-3}$	2.5

4.3.C Deposition Of Gallium And Nitrogen Codoped Zinc Oxide Thin Films At Room Temperature.

From a first principles calculation[40], it was proposed that ''co-doping'' of donor acceptor dopants (e.g. Ga and N, respectively) in ZnO might lead to p-type ZnO. In this method the simultaneous doping of both acceptor (N) and donor (Ga) into the ZnO lattice were carried out with an acceptor concentration twice that of the donor concentration to get a maximum conductivity in p-ZnO. The essential approach of this method is to stabilize the N substitution in the appropriate ZnO lattice sites by the formation of N–Ga–N type bonds, which reduce the N–N repulsive interaction (Madelung Energy) thereby making the acceptor level shallower, thus enhancing the acceptor doping. Successful growth of p-ZnO by co doping of gallium and nitrogen has been achieved first by Joseph et al. [41] with a room temperature resistivity of 0.5 Ω cm and a carrier concentration of 5 x 10^{19} cm^3 in p-type ZnO thin films deposited on glass substrate.

In the present study p type ZnO has been grown by PLD. Gallium doped zinc oxide targets were ablated in mixture of N_2O and oxygen atmosphere. The target of 5 atomic weight % of Ga doped ZnO was prepared by mixing ZnO and Ga_2O_3 (99.99% purity) powders with agate mortar and pestle. The powder was pressed and sintered at 900^0C for 5 hours in air. The target is a polycrystalline disk. Its surface is found to be pale yellow in colour, but this

changed noticeably, even upon exposure to just a single laser shot. After irradiation, the ZnO:Ga target is grey in colour within focal region and in its immediate surroundings. The diameter of the target is 1 inch.

The thin films were deposited at laser fluence of 2.7 J/cm^2 at 355nm on quartz substrates keeping the substrate to target distance 6 cm. The deposition was carried out at room temperature. The deposition chamber was initially pumped down to 2 x 10^{-6} mbar and then partially filled with N_2O flow upto 5 x 10^{-5} mbar then O_2 flow was adjusted to increase pressure to 0.006 mbar. The thin films deposited under combined O_2 and N_2O atmosphere were amorphous as indicated by XRD. The films show a transmission of > 80% in the visible range (fig 4.24). The inset of the figure 4.24 shows the transmission of gallium doped zinc oxide thin films. Thus there is no deterioration in the optical properties due to the nitrogen doping.

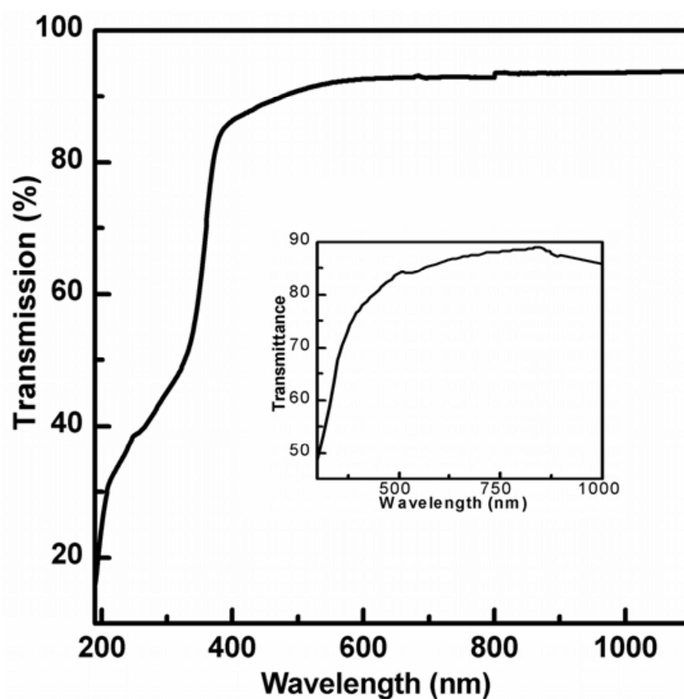

Figure 4.24. Transmission of gallium and nitrogen doped zinc oxide thin films. The inset shows the transmission spectra of gallium doped zinc oxide thin films.

The thermopower measurement of the films indicates that the films have a p type conductivity. The thermopower of the ZnO:(Ga,N) thin films are shown in figure 4.25. The Seebeck coefficient of p type ZnO:Ga,N films is +29.29 mV/K.

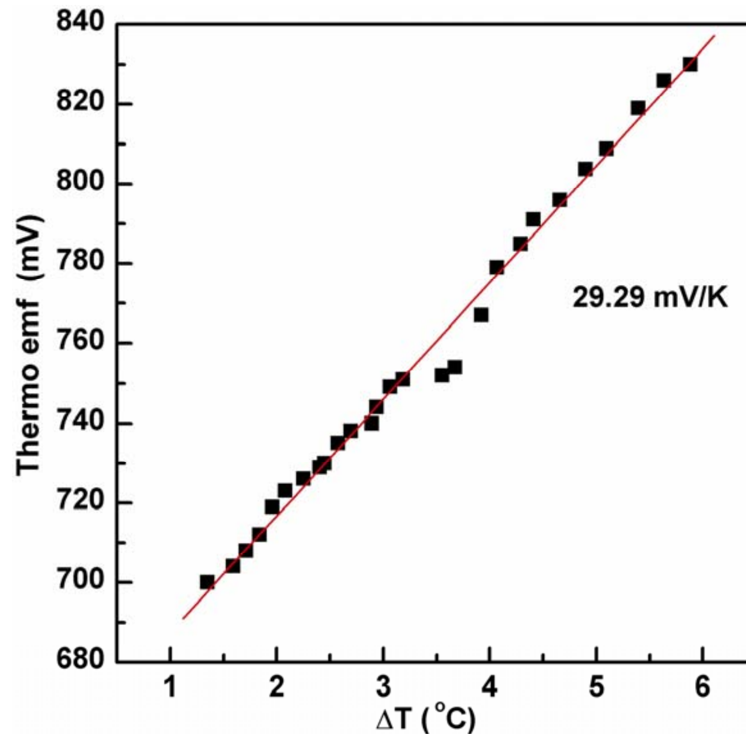

Figure 4.25. Thermopower of gallium and nitrogen doped zinc oxide thin films.

The gallium and nitrogen codoped thin films of zinc oxide have larger resistivity than aluminium doped zinc oxide thin films. The resistivity of the gallium and nitrogen codoped thin films show a resistivity of 2.5 x 10^2 Ω cm. Which is two orders of magnitude higher than the room temperature deposited aluminium doped zinc oxide thin films (0.28 Ω cm).

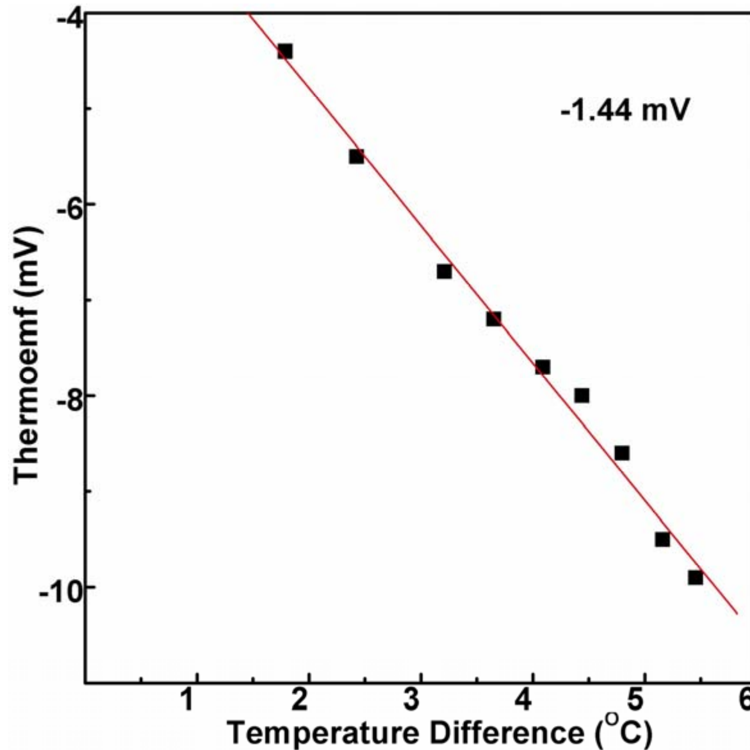

Figure 4.26. Thermopower of n type ZnO:Al thin films.

The Seebeck coefficient of ZnO:Al thin films is –1.44 mV/K (fig 4.26). Using the p type ZnO:(Ga,N) and n type ZnO:Al, a p–n junction was fabricated. The p type ZnO:(Ga,N) thin films were first grown on quartz substrate by PLD at room temperature. The n type ZnO:Al thin films were grown on top of the p type ZnO:(Ga,N) layer through a shadow mask. The ZnO:Al thin films were also deposited at room temperature by PLD. The third harmonics (355 nm) of Nd:YAG was used for both the depositions. For the transmission studies, approximately 1 cm^2 area was coated. For the current voltage characterisitics, ZnO:Al films of 3mm diameter were deposited. The structure of the device is as shown in figure 4.27. The diode structure has a total thickness of 285 nm and an optical transmission of 80% in the visible region (fig 4.28).

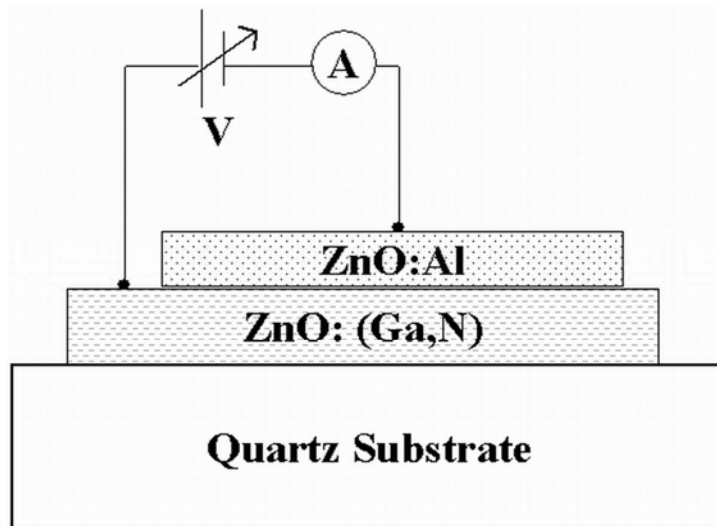

Figure 4.27. Structure of p–n junction of ZnO:(Ga, N) and ZnO:Al thin films.

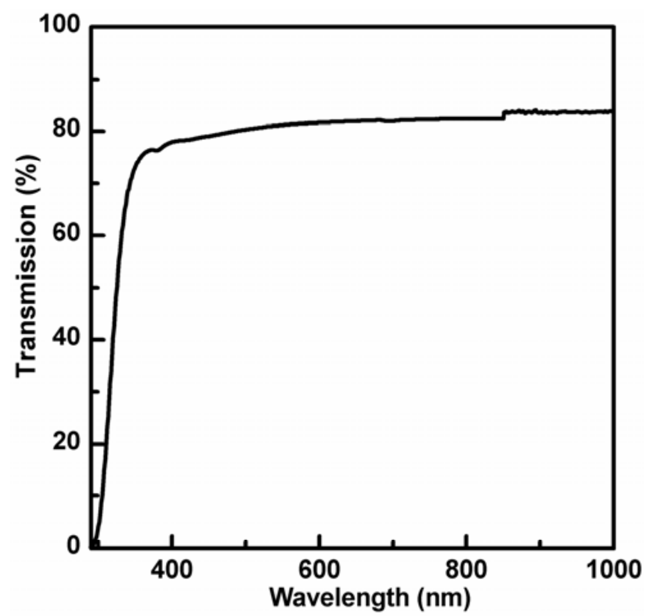

Figure 4.28. Transmission spectra of the ZnO homojunction diode.

The junction fabricated with n type ZnO:Al thin films and p type ZnO: (Ga, N) show non linear characteristics as shown in figure 4.29. The forward to reverse ratio of the current is 5.06. The ratio of forward current to reverse current is 5. The turn on voltage is very low this can be improved by reducing the no of carriers in the aluminium doped zinc oxide thin films. ZnO:Al thin films are degenerately doped when they are used as transparent electrode. This will raise the fermi level to near the conduction band effectively reducing the turn on voltage of the devices fabricated. Undoped ZnO thin films have lower carrier concentration than aluminium doped zinc oxide. Using undoped zinc oxide might improve the characteristics of the zinc oxide homojunction. Improving the interface between the p type zinc oxide and the n type zinc oxide would also improve the characteristics of the device.

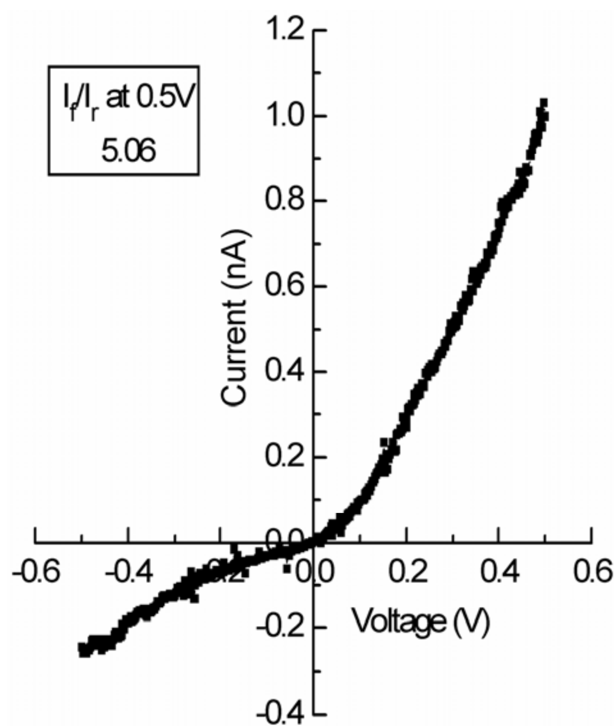

Figure4.29. Current – voltage characteristics of the junction of nitrogen and gallium doped zinc oxide and aluminium doped zinc oxide thin films.

4.4. Conclusions

Good quality c axis oriented ZnO:Al thin films were grown on various substrates at room temperature. Low resistive and highly transparent thin films were prepared by PLD at room temperature on quartz and polymer substrates. The oxygen pressure required for the growth of crystalline films is found to decrease with increase of substrate temperature. ZnO:Al thin films with resistivity 2.5 Ωcm and 85% transparent in the visible region were grown on PET substrates by PLD at room temperature.

Highly transparent and moderately conducting thin films of gallium and nitrogen codoped zinc oxide were deposited at room temperature. Seebeck coefficient of +29.29 mV/K is obtained from the thermopower mearurements, indicating the p type conduction in these films. The p–n junction fabricated with the p type gallium and nitrogen codoped zinc oxide thin films and the n type aluminium doped zinc oxide shows a forward to reverse ratio of 5.06. The gallium and nitrogen codoped zinc oxide thin films are amorphous as indicated by x –ray diffraction.

4.5. References

[1.] J. H. Morgan and D. E. Brodie, Can. J. Phys. **60,** (1982) 1387.

[2.] M.K.Jayaraj, A. Aldrin, and R.Manoj, Bull. Mater. Sci. **25** , (2002) 227.

[3.] V.Craciun, J.Elders, J.G.E.Gardeniers, and Ian W. Boyd, Appl. Phys. Lett. **65**, (1994) 2963.

[4.] A. Suzuki, T. Matsushita, N. Wada, Y. Sakamoto, and M. Okuda, Jpn. J. Appl. Phys. **35,** (1996) L56.

[5.] C. Tonon, C. Duvignacq, G.Teyssedre, and M. Dinguirard, J.Phys. D: Appl Phys. **34,** (2001) 124.

[6.] M. Purica, E. Budianu, and E. Rusu, Thin solid films **383,** (2001) 284.

[7.] M. Penza, C. Martucci, V.I.Anisimkin, and L.Vasanelli, Materials science fourm **203,** (1996) 137.

[8.] R. K. Theraja and A. Mitra, Appl. Phys. B **71,** (2000) 181.

[9.] D. M. Bagnall, Y. F. Chen, Z. Zhu, T. Yao, S. Koyama, M. Y. Shen, and T. Goto, Appl. Phys. Lett. **70,** (1997) 230.

[10.] M. Joseph, H. Tabata, and T. Kawai, Jpn J. Appl. Phys. **38,** (1999) L1205.

[11.] Y. R. Ryu , S. Zhu, D. C. Look, J. M. Wrobel, H. M. Jeong, and H.W. White, Journal of Crystal Growth **216,** (2000) 330.

[12.] K. Kim, H. Kim, D. Hwang, J. Lim, and S. Park, Appl. Phys. Lett. **83**, (2003) 63.

[13.] H. Kim, C. M. Gilmore, J. S. Horwitz, A. Pique, H. Murata, G.P. Kushto, R. Schlaf, Z. H. Kafafi, and D. B. Chrisey, Appl.Phys.Lett. **76**, (2000) 259.

[14.] L. Zugang, Z. Weiming, J. Rongbin, Z. Zhilin, J. Xueyin, X. Minzhao, and F. Bin, J.Phys. Condens.Mater. **8,** (1996) 3221.

[15.] L. Znaidi, G. J. A. A. S. Illia, S. Benyahia, C. Sanchez, and A.V. Kanaev, Thin Solid Films **428**, (2003) 257.

[16.] J. Lu, Z. Ye, J. Huang, L. Wang, and B. Zhao, Appl. Sur. Sci. **207**, (2003) 295.

[17.] K. Haga, T. Suzuki, Y. Kashiwaba, H. Watanabe, B. P. Zhang, and Y. Segawa, Thin Solid Films **433**, (2003) 131.

[18.] A. B. M. A. Ashrafi, I. Suemune, H. Kumano, Jpn. J. Appl. Phys. **41**, (2002) 2851.

[19.] T. Nakamura, H. Minoura, and H. Muto, Thin Solid Films **405**, (2002) 109.

[20.] M.Lorenz, H. Hochmuth, J. Lenzner, T. Nobis, G. Zimmermann, M.Diaconu, H. Schmidt, H. Von Wenckstern and M. Grundmann, Thin Solid Films **486,** (2005) 205.

[21.] X. W. Sun and H. S. Kwok, J. Appl. Phys. **86**, (1999) 408.

[22.] S. T. Tan, B. J. Chen, X. W. Sun, H. S. Kwok, X. H. Zhang and S. J. Chua, J.Appl.Phys. **98,** (2005) 13505

[23.] K. K. Kim, H. S. Kim, D. K. Hwang, J. H. Lim, S. J. Park, Appl. Phys. Lett **83**, (2003) 63.

[24.] S. J. Henley, M. N. R. Ashfold, D. Cherns, Surface and Coatings Technology **177–178**, (2004) 271.

[25.] V. Craciun, J. Elders, J. G. E. Gardeniers, and L. W. Boyd, Appl. Phys. Lett. **65**, (1994) 2963.

[26.] S. Choopun, R.D. Vispute, W. Noch, A. Balsamo, R. P. Sharma, T. Venkatesan, A. Lliadis, D. C. Look, Appl.Phys. Lett. **75**, (1999) 3947.

[27.] R. D. Vispute, V. Talyansky, Z. Trajanovic, S. Choopun, M. Downes, R. P. Sharma, T. Venkatesan, M. C. Woods, R. T. Lareau, K. A. Jones and A. A. Lliadis, Appl.Phys. Lett. **70**, (1997) 2735.

[28.] K. Y. Cheong, Norami Muti, S. Roy Ramanan, Thin Solid Films **410** (2002) 142.

[29.] H. Sato, T. Minami, S. Takata, T.Miyata and Ishii, Thin Solid Films, **236** (1993) 14.

[30.] P. Nunes, B. Fernandes, E. Fortunato, P. Vilarinho, R. Martins, Thin Solid Films **337** (1999) 176.

[31.] A. B. M. Almamun Ashrafi, Ikuo Suemune and Hidekazu Kumano, Jpn. J. Appl. Phys. **41** (2002) 2851.

[32.] F. Claeyssens, A. Cheesman, S. J. Henley, and M. N. R. Ashfold, J. Appl. Phys. **92**, (2002) 6886.

[33.] S. V. Prasad, S. D. Walck, J. S. Zabinski, Thin Solid Films **360**, (2000) 107.

[34.] B. E. Sernelius, K. F. Berggren, Z. C. Jin, I. Hamberg, and C. G. Granqvist, Phys. Rev. B **37**, (1988) 10244

[35.] T. Aoki and Y. Hatanaka, and D. C. Look, Appl. Phys. Lett. **76**, (2000) 3257.

[36.] D. H. Zhang, Z. Y. Xue, and Q. P. Wang, J of Phys D Appl. Phys. **35,** (2002) 2837.

[37.] K.Vanheusden, C. H. Seager, W. L. Warren, D. R. Tallant, and J. A. Voigt, J. Appl. Phys. **79**, (1996) 7983.

[38.] P.Y.Yu, M.Cardona Fundamentals of semiconductors: Physics and material properties, Springer, Berlin 1996.

[39.] K. F. Berggren and B. E. Sernelius Physical Review B **24**, (1981) 1971.

[40.] T. Yamamoto, H.K. Yoshida, Jpn. J. Appl. Phys. 38 (1999) L166.

[41.] M. Joseph, H. Tabata, T. Kawai, Jpn. J. Appl. Phys. **38** (1999) L1205.

Chapter 5

Transparent Conducting Zinc Oxide Thin Film Prepared By Off Axis RF Magnetron Sputtering

Highly conducting and transparent ZnO:Al thin films have been grown by off axis rf magnetron sputtering on glass substrate without any post deposition annealing treatment. The electrical and optical properties of the films deposited at various substrate temperatures and target to substrate distance were investigated in detail. Optimized ZnO:Al films have conductivity 2000Scm^{-1} and average transmission in the visible range is higher than 85%.The conductivity and mobility show very little temperature dependence.

5.1. Introduction

Zinc Oxide is a n-type compound semiconductor with a wide direct band gap of 3.3e.V. Thin films of ZnO find application as transparent conducting electrode in photovoltaics in the place of expensive tin doped InO_2 (ITO) in displays [1], electric transducers [2]. More recently, the reports on possible p- type doping of ZnO have aroused much interest in ZnO thin films [2-5].
Doping of ZnO films with Al, Ga, In, Ge has reported to improve their electrical properties [6]. Al doped ZnO films have been widely studied and have low resistivity 2-5x10^{-4} Ωcm that is comparable to that of ITO films.

Several deposition techniques have been used to grow doped and undoped ZnO thin films including chemical vapor deposition (C.V.D) [7], magnetron sputtering [8], spray pyrolysis [9], pulsed laser deposition [10], chemical bath deposition [11] and evaporation [12].
ZnO films with very smooth surface and good quality crystal structure have been synthesized by off axis sputtering [13]. The optimization of substrate temperature, gas pressure, substrate to target distances and orientation in order to get highly conducting, transparent and smooth films with good crystal structure is reported in this chapter.

5.2. Experimental procedure

The ZnO films were prepared by rf magnetron sputtering in the off axis sputtering geometry as shown in figure 5.1. The sputtering targets were prepared from powder of ZnO 99.99 + % purity and dopant Aluminum oxide with purity 99 + %. In the case of Al doped samples, the ZnO and Al_2O_3 powder were mixed using agate mortar and pestle. The powder was pressed to form a 2 in diameter target. The targets were sintered at 900°C for ten hours in air with intermediate grinding. Two types of targets, one with no dopant, and another with 2% of Al were used for the deposition of the films. Before depositing the films, the ZnO target surfaces were cleaned by presputtering under the film deposition conditions for 30 minutes. The films

were deposited at various substrate target distances, rf power and sputtering pressure.

The sputtering was carried out in high purity Ar gas. For the growth of transparent and conducting metal oxide thin films it is essential that non stochiometric metal rich oxide films be deposited [14]. The resistivity was found to increase drastically when oxygen was introduced to the sputtering gas. Fused quartz was used as the substrate. The film growth temperature was measured by a thermocouple attached to substrate holder placed over the heater block.

The structure of the thin films and targets were analyzed using an X-Ray diffractometer. Atomic force microscope (AFM) was used to study the film morphology. The conductivity and hall coefficients were determined by using Van Der Pauw technique. Transmittance was measured using a Jasco uv-vis-nir spectrometer.

The film growth conditions were optimized to obtain highly conducting transparent films. The film deposition was carried out on axis (target and substrate parallel) and off axis (fig 5.1) substrate perpendicular to target.

The off axis configuration results in non-uniform film thickness across the substrate. The deposition rate is higher at the points on substrate that are near the target and it decreases as the points on the substrate position moves further away from the target. However off axis configuration gives much better results than on axis configuration. To minimize the thin film non-uniformity the quartz substrate of 1 x 1 cm was used for the deposition and evaluation of the electrical and optical properties. All the data presented here are for films grown on amorphous silica substrate at a pressure of 10 m bar. The deposition rate was obtained as the ratio between film thickness and sputtering time. The thicknesses of the films were measured using Vecco Stylus profilometer and also by optical interference method.

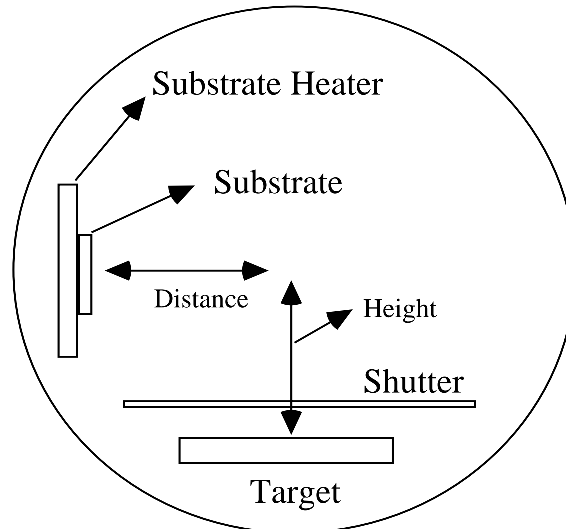

Figure 5.1. Off axis sputtering configuration used for depositing ZnO thin films.

The deposition rate is directly proportional to the rf power as shown in figure 5.2. Keeping the substrate to target height at 2.5 cm, the deposition rate was found to fall drastically as the substrate to target distance increased (Fig.5.3). Beyond 2 cm substrate to target distance, the deposition rate is too low because the substrate is outside the plasma.

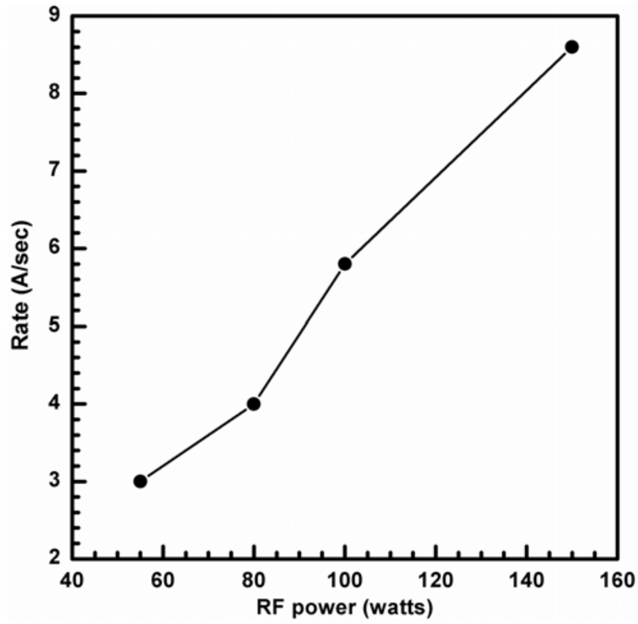

Figure 5.2. Variation of sputtering rate with rf power

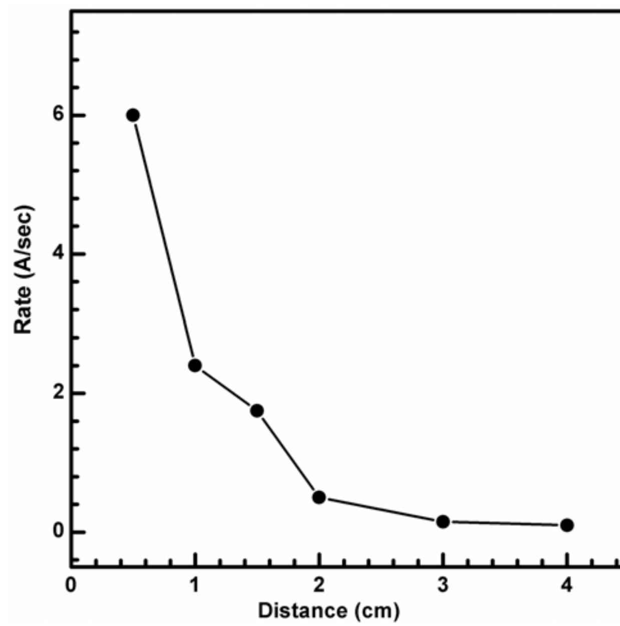

Figure 5.3. Variation of sputtering rate with substrate to target distance with the substrate to target height at 2.5 cm

5.3.Results and Discussions

The X-ray diffraction pattern of ZnO films and targets are shown in figure 5.4. The X-ray diffraction shows only 002 peak indicating the films polycrystalline. And c axis of the grains becomes uniformly perpendicular to the substrate surface. The surface energy density of the 002 orientation is the lowest in ZnO crystal [14]. Grains with lower surface energy will become larger as the film grows. Then the growth orientation develops into one crystallographic direction of the lowest surface energy. This means that 002 texture of the film may easily form.

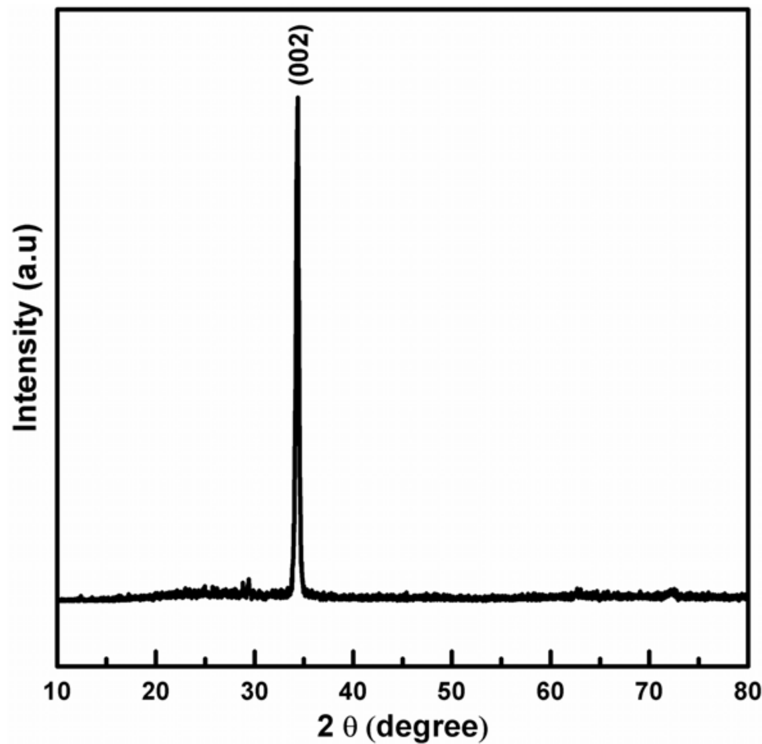

Figure 5.4. XRD pattern of ZnO:Al thin films deposited by off axis sputtering.

ZnO:Al films are highly transparent and shows >85% transmission in the visible region irrespective of the doping and substrate to target distance. The transmission spectrum of ZnO:Al films deposited under identical sputtering conditions but varying the substrate to target distance is given in figure 5.5.

Figure 5.6 shows the transmission of undoped ZnO thin films. All the films exhibit a transmission >85% in the visible region. However there is a shift in the absorption band edge. The shift in the absorption edge can be accounted in terms of increase in carrier concentration and blocking of low energy transitions causes a Burstein Moss (BM) effect, which enhances the optical band gap. Figure 5.7 shows the variation of optical band gap vs. electron density of ZnO:Al films.

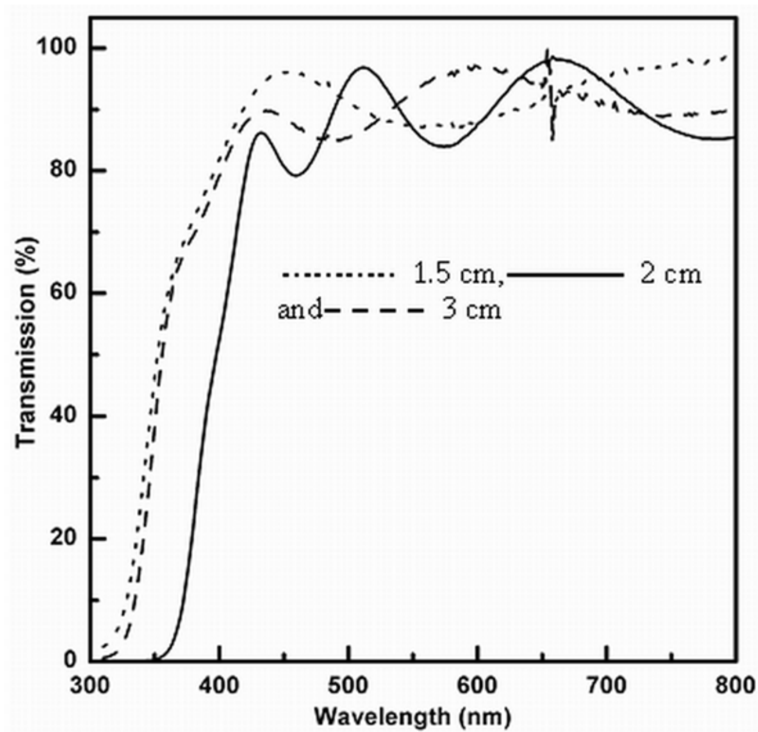

Figure 5.5. Transmission spectra of ZnO:Al thin films deposited by off axis sputtering at various substrate to target distances

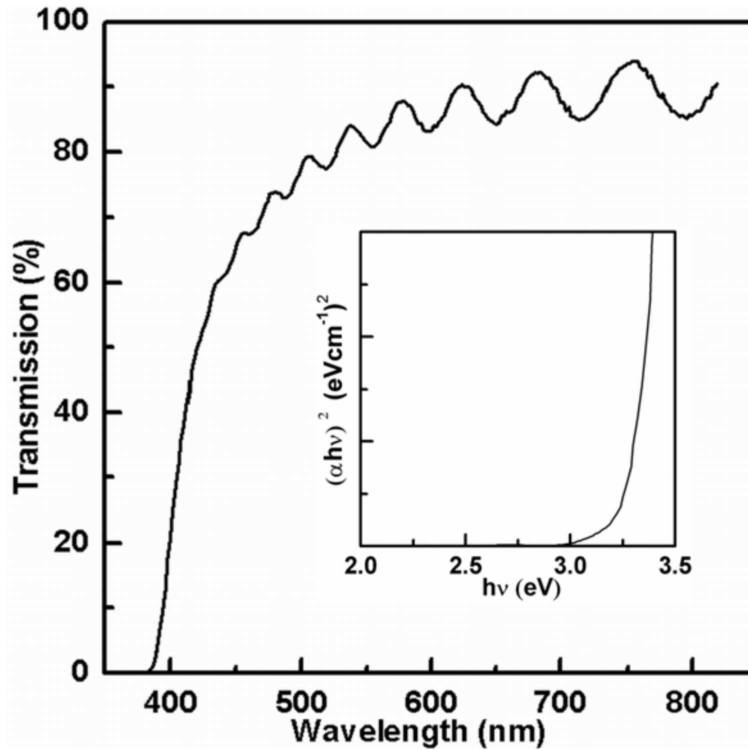

Figure 5.6. Transmission spectra of undoped ZnO thin films deposited by off axis sputtering

The carrier concentration was obtained from Hall measurement data and the optical band gap was evaluated from the transmission spectra. The absorption coefficient α was evaluated using the measured value of thickness 't' using the relation $I = I_O e^{-\alpha t}$. The optical absorption coefficient 'α' near the absorption edge is given by $\alpha \propto A (h\nu - E_{op})^{1/2} / h\nu$. The direct band gap of ZnO thin film was estimated by plotting $(\alpha h\nu)^2$ vs. $h\nu$ and extrapolating the linear portion near the onset of absorption edge to the energy axis. A typical $(\alpha h\nu)^2$ vs. $h\nu$ plot of ZnO film is shown in the inset of figure 5.6. The optical band gap shows increase with increase of carrier concentration(fig 5.7).

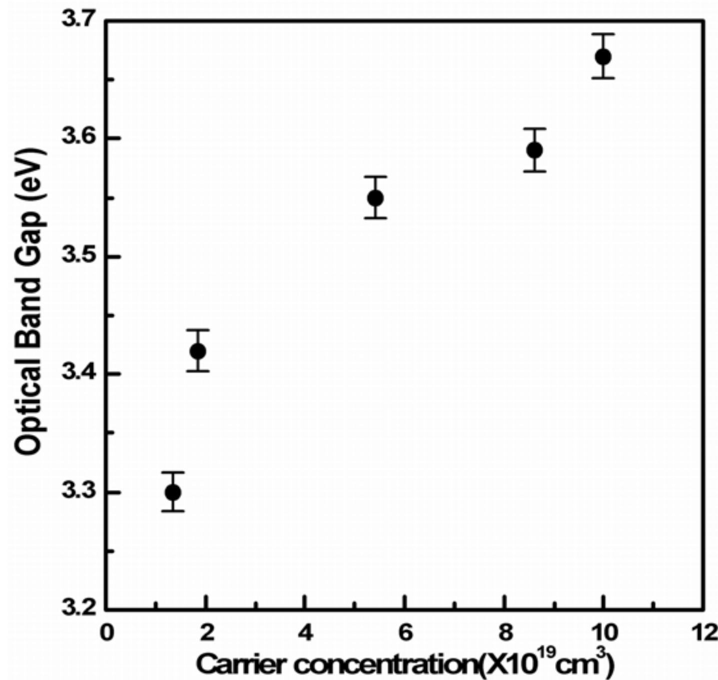

Figure 5.7. Variation of band gap with carrier concentration of ZnO:Al thin films

The optical gap is defined as the minimum energy needed to excite an electron from the valence band to the conduction band. In pure undoped crystals the optical gap equals the energy separation between the band edges. On heavy doping, the donor electrons occupy states at the bottom of the conduction band, since Pauli principle prevents states from being doubly occupied, the optical band gap is given by the energy difference between the states with Fermi momentum in the conduction and valence band. This type of blocking of low energy transitions is known as Burstein - Moss effect[15].

The conductivity of the ZnO:Al sputtered films increase with the increase of substrate temperature and show a maximum around 150° C (Fig.5.8) and falls very rapidly above the substrate temperature of 250° C. The composition analyses by EPMA show that Al composition in the film is the same as that of the target and independent of the substrate temperature.

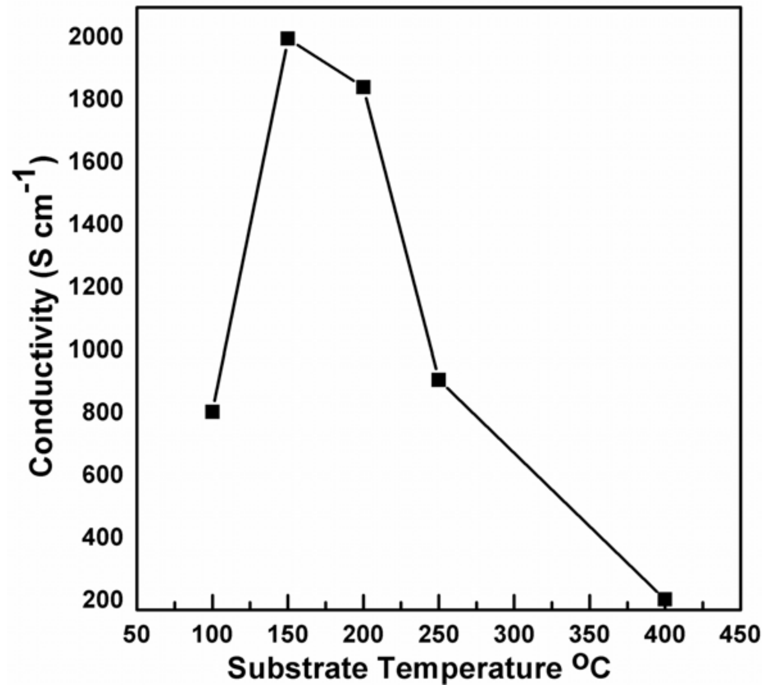

Figure 5.8. Variation of conductivity with substrate temperature for films grown at substrate to target distance 1.5 cm and height 2.5 cm.

The films grown by off axis sputtering have an average roughness of 2.5 nm while the films grown by on axis sputtering have an average roughness of 25.42 nm (fig 5.9 a). The off axis sputtering provides method to deposit very smooth films. The AFM picture of the off axis sputtered films show that all the films are very smooth and have very similar morphology independent of the substrate temperature. (Fig.5.9 b.) The change in conductivity is due to both change in carrier concentration as well as the mobility as indicated by hall measurements. The increase in carrier concentration may be due to the formation of metal rich oxide films. The best film properties in terms of conductivity and transmission were obtained for a substrate temperature of 150°C.

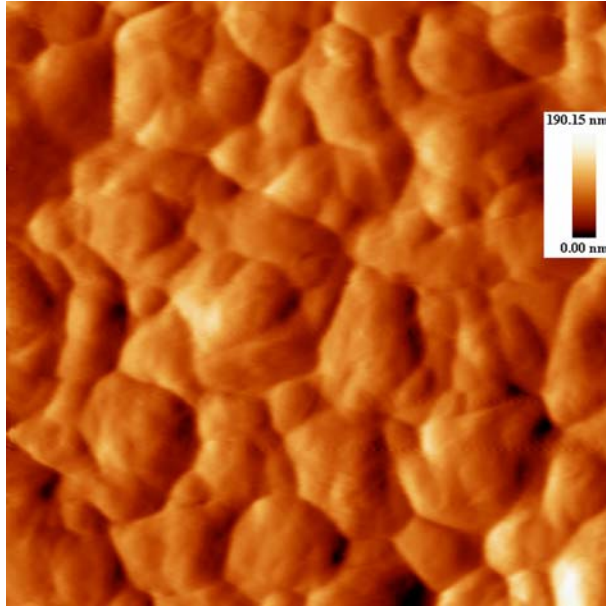

Figure 5.9 a. AFM picture of on axis sputtered Zinc oxide thin films

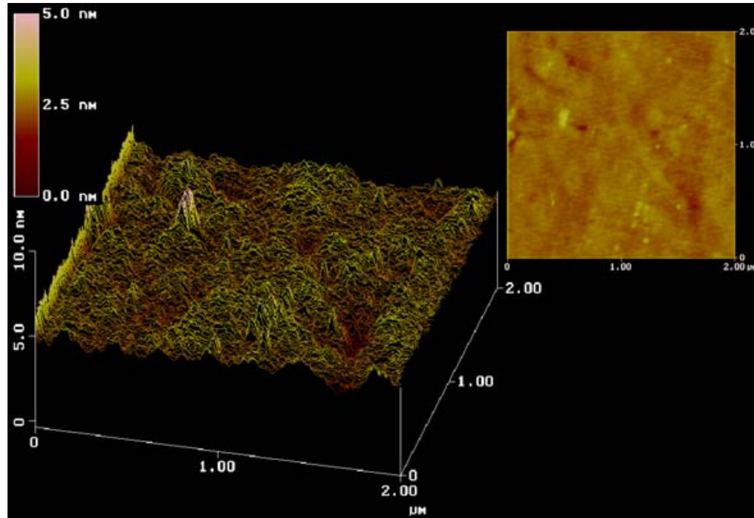

Figure 5.9 b. AFM picture of zinc oxide thin films grown by off axis sputtering.

Figure 5.10 shows the variation of conduction and mobility as function of substrate temperature keeping the substrate–target distance 1.5 cm and substrate to target height at 2.5 cm.

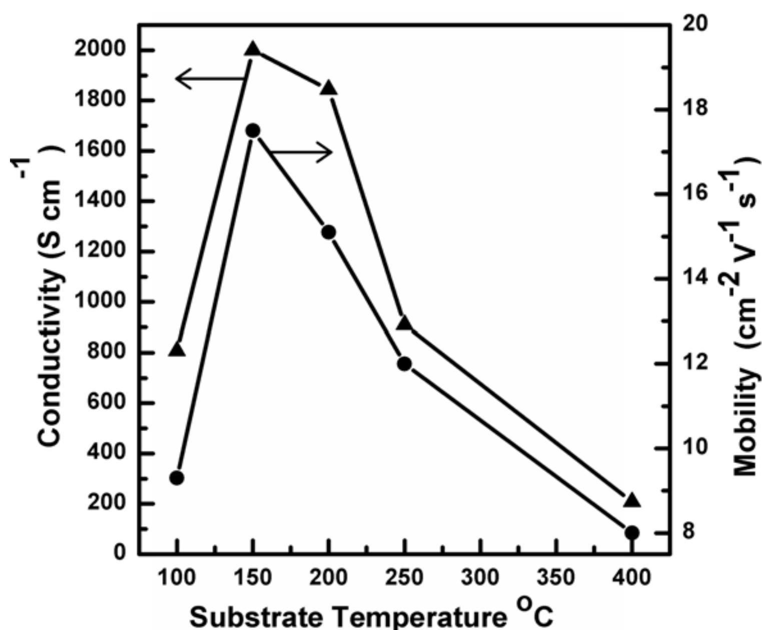

Figure 5.10. Variation of conductivity and mobility of ZnOAl thin films with substrate temperature

Higher conductivity was observed for films deposited at substrate to target distance of 1.5 cm. The Hall measurement shows the higher conductivity is due to the increase in both carrier concentration as well as the mobility of the carrier.

The resistivity of both ZnO:Al and ZnO films show very little dependence on temperature(fig.5.11). It can be observed that the resistivity of undoped ZnO increases slightly with decreasing temperature. This dependence is too small in the case of ZnO:Al films. The nearly temperature independence of the resistivity confirms that the ZnO films are degenerate semiconductors.

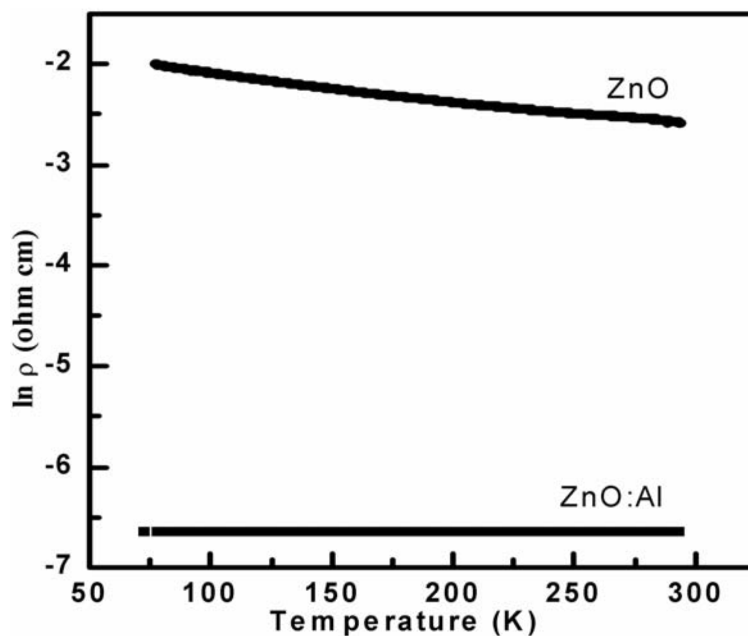

Figure 5.11. Variation of resistivity of ZnO and ZnO:Al thin films with temperature.

5.4. Conclusion

Undoped zinc oxide and aluminum doped zinc oxide films were prepared by rf magnetron sputtering of presynthesised target. All the films exhibit a transmission over 80% in the visible region. The electrical resistivity of the film strongly depends on the substrate temperature, substrate to target distance and orientation of the substrate. The increase in conductivity is due to the increase of carrier concentration and also due to the increased mobility of the carriers. Under the optimized deposition condition the ZnO:Al film show a resistivity 4.5X 10^{-4}ohm cm with transparency of >85%. Morphology of the films shows the films are very smooth.

5.5 References

1) M.C Addonizo, A.Antonaia, Cantele and C.Privato, Thin Solid Films **349** (1999), 93
2) T.Yamamoto, H.Yoshida Jpn. J. Appl Physics pt2,**38** (1999)L1453
3) M Joseph, H Tabata and T.Kawa Jpn. J. Appl Physics, **38**(1999) pt2 L1205
4) K. minegishi, Y.Kikuchi, K Yano Jpn. J. Appl Physics, **36** (1997) L1453
5) Y.R.Ryu, S. Zhu, D. C. Look, J. M. Wrobel, Amjeony, H. W. White J. Crystal Growth **216**(2000) 330
6) R. Wang, L. L. H. King, A. W. Sleight J. Mater Res.11 (1996) 1659
7) J. Hu, R. G. Gordan J. Appl Physics **72**(1992) 5381
8) J. F. Chang, H. L. Wang, M. H. Hon J. Crystal growth **211** (2000) 93
9) K.J. Ramakrishna Reddy, H. Gopalaswamy, P.J. Reddy and R.W. Miler. J. Crystal Growth **210**(2000) 516
10) H. Kim, C.M. Gilmore, J. S. Horwitz, A. Pique, H. Murata, G. P. Kushoto, R. Schlaf, Z. H. Kafai and B. D. Chrisey Appl. Phys **76**(2000) 259.
11) H. Sato, T. Minami, S. Takata, T. Miyata and M. Ishii. Thin solid films **236**(1993)14
12) Majin, Ji Feng, Z De-Heng, Ma Hong-Li, Li Shu-Ying. Thin Solid Films **357**(1999)98
13) S. Zhu, C. H. SU, S.L. Lehouzky, P. Peters, M.A. George. J. Crystal Growth **211**(2000)106
14) K.L. Chopra, S. Major, D.K. Pandaya. Thin Solid Films **102**(1983)1
15) N. Fujimura, T. Nishihara, S. Goto, J. Xu, T. Ito J.Crystal Growth **130** (1993)269
16) A.P. Roth, J.B. Webb and D.F. Williams Phys Rev B **25**(1982)7836
17) B.E. Sernellius, K.F. Berggren, Z.C. Jin, I. Hamberg and C. Grangrist Phys Rev B **37** (1988) 10244

Chapter 6

Properties Of RF Sputtered Calcium Doped $CuYO_2$ p-Type Transparent Conducting Films

Transparent thin films of copper yttrium oxide doped with 2% calcium have been prepared by RF magnetron sputtering. The conductivity of films increases to 8 Scm^{-1} on intercalation of oxygen at high pressure, and reduces the transparency in the visible region. The temperature dependence of the conductivity indicates semiconductor behaviour with low activation energy of 0.59 eV at room temperature. The positive sign of Seebeck coefficient (+274μVK^{-1}) confirms the p-type conductivity of the films. The optical bandgap of Ca doped $CuYO_2$ was found to be 3.15 eV. The photoluminescence spectra show a broad emission at 545nm that quenches on Ca doping.

6.1.Introduction

Transparent conducting oxide (TCO) thin films have a wide range of applications in optoelectronic devices [1], because of their unique transparent and conducting properties. Most of the TCO's exhibit n-type electrical conductivity. Indium tin oxide (ITO) and aluminum doped ZnO which has a bandgap > 3eV, transmission >80% in the visible region and conductivity of the order of $10^4 Scm^{-1}$ are n type conductors. These n-type TCO's have wide range of application but limited as passive component such as transparent electrodes and IR reflecting coatings etc. The development of p-type TCO's will open up new applications in optoelectronic devices. The theoretical predication of the possibility of producing p-type conducting ZnO [2] by co doping with nitrogen and gallium has aroused much interest in the field of TCO's. There are several reports in the recent literature on the growth of p-type ZnO [3-9]. However the reproducibility of good p-type ZnO TCO material remains a difficult task. p-type conductivity has also been reported in NiO films [10] which has 30% transparency in the visible region. The $CuAlO_2$ thin films having a delafossite structure has shown a transparency 80% in the visible region and infrared region with electrical conductivity $1Scm^{-1}$[11]. This has generated much interest in p-type conducting transparent thin films [12]. P-type conductivity was found in a number of delafossites compounds $CuYO_2$ [13], $CuScO_2$ [14], $CuCrO_2$ [15,16], $CuGaO_2$ [17,18] and $CuInO_2$ [19].

$CuYO_2$ is p-type semiconductor having wide bandgap isostructural with $CuAO_2$ delafossite (where A= Fe, Co, Rh, Ga,Sc,Y or lanthanides) [20]. Intercalation with oxygen to form $CuAO_{2+\delta}$ phases is possible for compounds with large A^{3+} cations. Cava et al [21,22] have investigated the properties of polycrystalline $CuYO_{2+\delta}$ and $CuLaO_{2+\delta}$ phases. The $CuYO_{2+\delta}$ doped with calcium show conductivity as high as $10Scm^{-1}$ after the oxygen intercalation. Similar observation of increase in conductivity has been reported for $CuScMgO_{2+\delta}$ films on oxygen intercalation [23]. But the oxygen intercalation results in the reduced transmittance in these films.

The electrical and optical properties of the Ca doped $CuYO_2$ films are presented in this chapter. The variations in the electrical and optical properties on annealing these films under various oxygen partial pressures have also been studied. The Photoluminescence(PL) emission and excitation (PLE) of $CuYO_2$ and Ca doped $CuYO_2$ is also presented.

6.2.Experimental

Ca doped $CuYO_2$ was synthesized in the laboratory from a intimate mixture of CuO and Y_2O_3 and CaO. This mixture was pelletized and heated at 1100^oC for 24 hours in air. The powder thus synthesized were polycrystalline $Cu_2Y_{1.96}Ca_{0.04}O_5$ ($CuYO_2$:Ca)(Fig6.1) [22].
This powder was again heated in flow of argon at 1050 ^oC for 70 hours producing $CuY_{0.98}Ca_{0.02}O_2$ (($CuYO_2$:Ca)$_2$). The sputtering target was prepared by pressing the Ca doped $CuYO_2$ powder into a 2 inch diameter pellet and heating at 1100 ^oC for 12 hrs. The sputtering was carried out by on-axis geometry on to fused quartz substrates. Initially when the films were sputtered at room temperature, the substrate temperature was found to increase up to 80^oC hence all the subsequent sputtering were carried out at a substrate temperature of 100^oC.

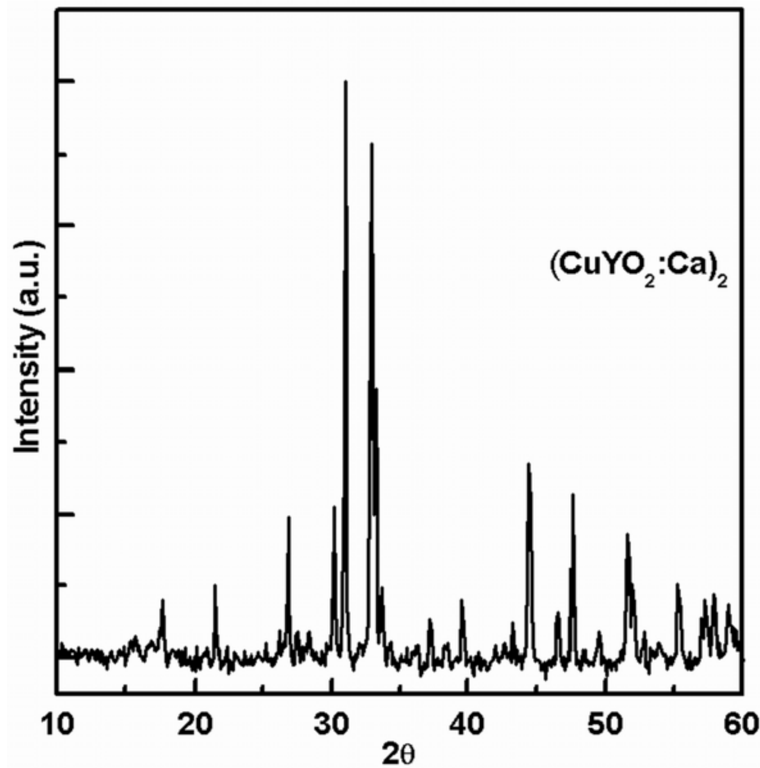

Figure 6.1. XRD pattern of $(CuYO_2{:}Ca)_2$ powder.

The sputtering chamber was initially pumped down to a pressure of $2x10^{-5}$ mbar and then filled with argon gas up to 0.008 mbar. Pre sputtering was carried out for 20 minutes before each deposition. The as deposited films were dark coloured and insulating. The films were subjected to a post deposition annealing at 700 ^oC in air for 10 minutes followed by 10 minutes annealing in argon atmosphere at 900 ^oC, which result in transparent Ca doped $CuYO_2$ films. The oxygen intercalation was achieved by annealing the films at various oxygen partial pressures. The annealing chamber was initially evacuated to $5x10^{-6}$ mbar and oxygen was fed into the chamber through a mass flow controller during the annealing. The crystal structure of the films were analysed by Rigaku X-ray diffractometer in θ–2θ geometry using Cu K_α radiation. All the as deposited films were amorphous. The composition of the target as well as the sputtered films were analysed using energy dispersive x-ray (EDX) measurements. The EDX measurements

show the films have the same compositions of the target with Cu/(Y+Ca) ratio equal to one. The conductivity was measured by two-probe method using the silver electrodes in the planar geometry using a Keithley source measure unit (SMU 236). The transmission spectra of the films were recorded using a UV-Vis-NIR spectrophotometer (Hitachi U – 3410), The Ca doped $CuYO_2$ films showed p-type conductivity that was confirmed by thermoelectric power measurements. The PL emission and the PL excitation spectra were recorded using Fluorimeter (Fluoro Max -3).

6.3.Results and discussion

Figure 6.2 shows the X-ray diffraction (XRD) pattern of the Ca doped $CuYO_2$ target used for sputtering.

Figure 6.2. X-ray diffraction pattern of the Ca doped $CuYO_2$ target used for sputtering.

The XRD pattern is consistent with delafossite structure belonging to R3m or P63/mmc [24]. The as deposited films were amorphous by XRD (fig 6.3). These films when subjected to a post deposition annealing at 700 °C in air for 10 minutes forming CuY_2O_5 phase which on reduction in argon atmosphere at 900 °C for ten minutes, result in delafossite structure belonging to 2H or 3R polytype.(fig 6.3)

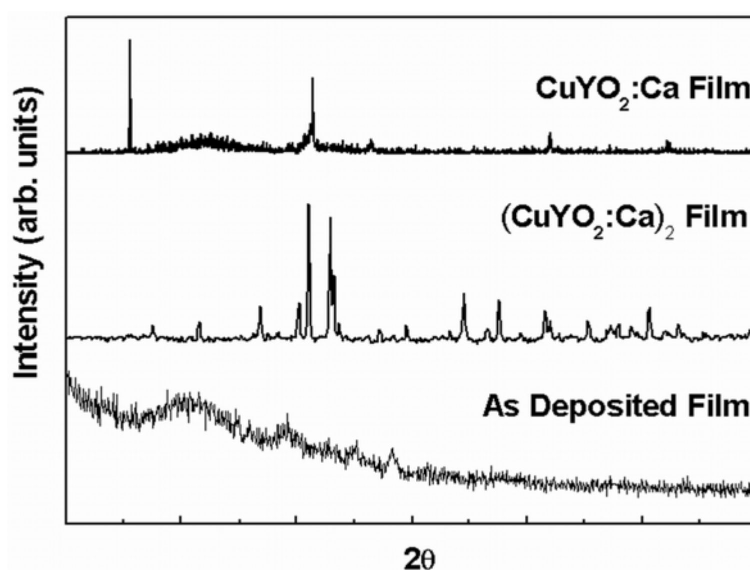

Figure6.3. XRD pattern of as deposited film, $(CuYO_2{:}Ca)_2$ phase and $CuYO_2{:}Ca$ thin film

Oxygen intercalation by annealing the films at 420°C at an oxygen pressure of one atmosphere, did not result in decomposition of the delafossites into the more stable $Cu_2Y_2O_5$ phases. However prolonged annealing at one atmospheric oxygen pressure show considerable decrease in the intensity of the diffraction peak (Fig 6.4). The transmission spectrum of Ca doped $CuYO_2$ films recorded in the range of 200-900 nm is shown in figure 6.5. The films are transparent yellow in colour. The Ca doped $CuYO_2$ films before oxygen intercalation is transparent in the visible range with average transmission of about 60%. The transparency in the visible region is found to decrease with oxygen intercalation in to the films. The highly transparent

films are less conducting and the conductivity increase with oxygen intercalation at the expense of transparency. The bandgap of the Ca doped $CuYO_2$ films were calculated from the transmission spectra by assuming a parabolic band structure for the material. The absorption coefficient and bandgap can be related by the expression $\alpha h\nu = A(h\nu - E_g)^{1/N}$ where E_g is the bandgap energy and α is the absorption coefficient corresponding to frequency ν [25].

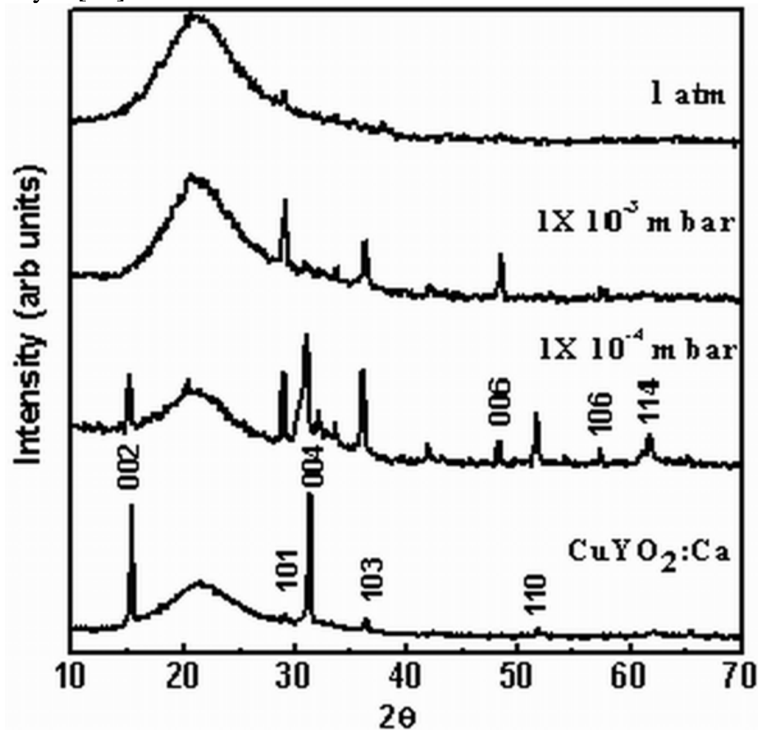

Figure 6.4. XRD pattern of $CuYO_2$: Ca thin films annealed under various O_2 pressures

The constant N depends on the nature of electronic transition. In the case of Ca doped $CuYO_2$ films N is equal to 2, for direct allowed transition. The bandgap of the films were determined from the plot of $(\alpha h\nu)^2$ versus $h\nu$ by extrapolating the linear portion of the curve to $h\nu$ equal to zero.

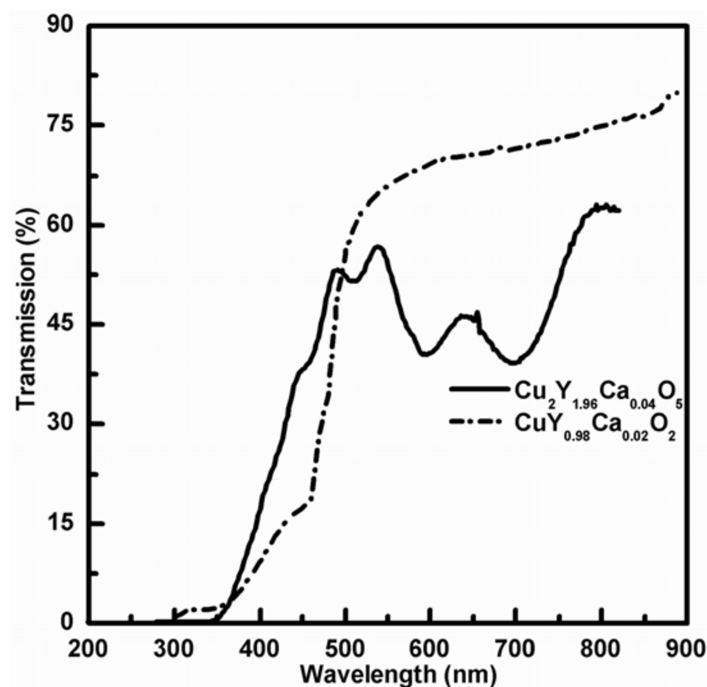

Figure 6.5. Transmission spectra of Ca doped $CuYO_2$ thin films and the thin films of the dimmer $Cu_2Y_{1.96}Ca_{0.04}O_5$.

In the present study the bandgap of Ca doped $CuYO_2$, obtained after annealing the as deposited films in oxygen atmosphere at 700°C followed by annealing in argon atmosphere at 900°C for 10 minutes each, was found to be 3.01eV. The band increases to 3.14eV on oxygen intercalation by annealing in 10^{-5} mbar oxygen pressure at 420°C. The increase in bandgap can be explained on the basis of Burstein-Moss effect [26]. Burstein-Moss shift is proportional to carrier concentration. The increase in carrier concentration due to the oxygen intercalation results in bandgap widening. On oxygen intercalation at one atmospheric pressure the bandgap is found to decrease compared with the stoichiometric Ca doped $CuYO_2$ films (figure 6.6). This can be explained as due to bandgap narrowing caused by excess carriers [27]. The addition of carriers causes the downward shift of the conduction band caused by the addition of the free carriers due to their mutual exchange and Coulomb interactions. The valance band is affected in the opposite way, owing to the added impurities the interactions among the

particles in the valence band are weakened as a result the valance band is shifted upwards. This results in the bandgap narrowing in heavily doped semiconductors. The crystallinity of these films is also very poor.

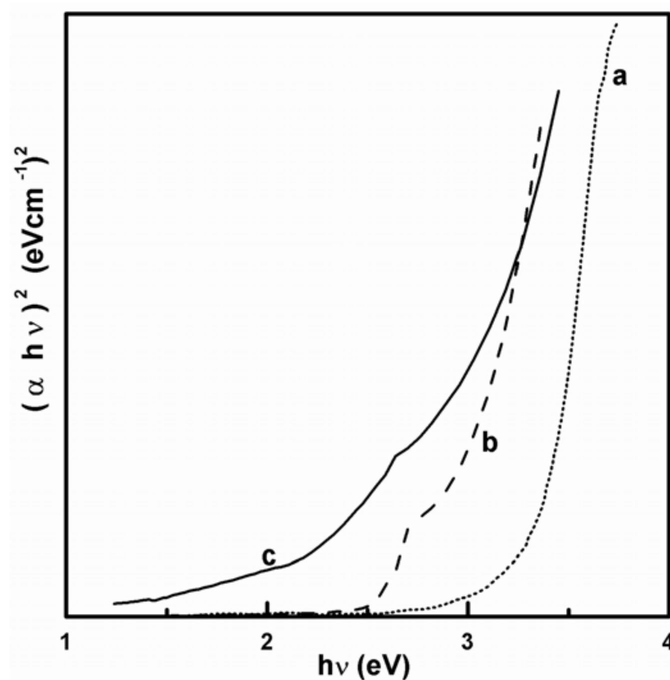

Figure 6.6. Plot of $(\alpha h\nu)^2$ vs hν for the thin films of a) $Cu_2Y_2O_5$ (3.37eV) b) Ca doped $CuYO_2$ (3.01 eV) and c) Oxygen intercalated Ca doped $CuYO_2$ (2.88 eV) .

The electrical properties of the films also show a dependence on the oxygen partial pressure during the annealing. The films before oxygen intercalation showed high resistivity.

The resistivity as well as the transmission of the Cu_2YO_2 films is found to decrease with the oxygen partial pressure during the annealing (Fig 6.7). The highest conductivity at room temperature, 8 Scm^{-1} was observed for films annealed at one atmosphere pressure.

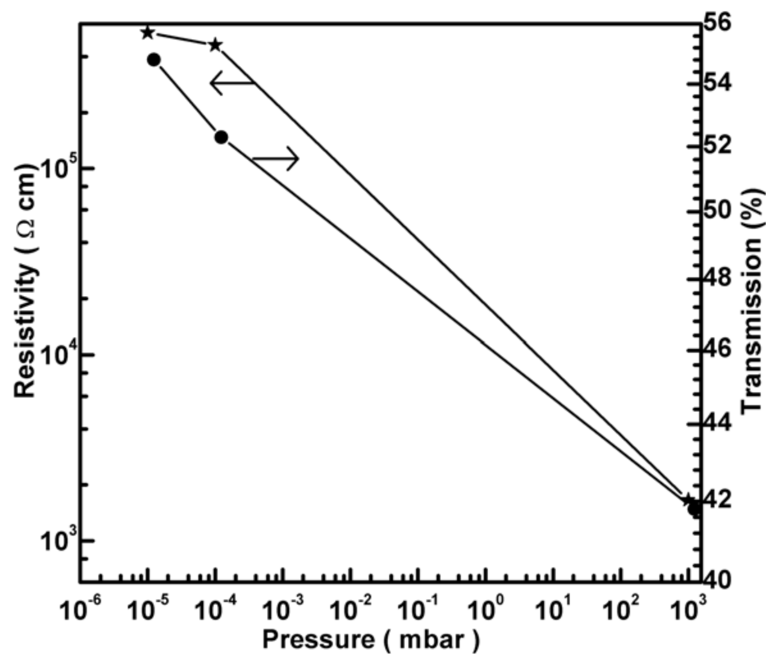

Figure 6.7. Variation of resistivity and transmission of Ca doped $CuYO_2$ film with oxygen pressure on annealing at 420°C.

The temperature dependence of the conductivity of oxygen intercalated Ca doped $CuYO_2$ films are shown in figure 6.8. The activated behaviour is typical of $CuAO_2$ p-type oxides[13–15]. The activation energy obtained from the plot of ln σ versus $10^3/T$ plot are 0.59eV and 0.19eV at high and low temperatures respectively. The ln σ versus $10^3/T$ plot is not a well fit by straight line. However ln σ vs $T^{-1/4}$ plot is close to a straight line suggesting a variable range hopping model for the conduction [28].

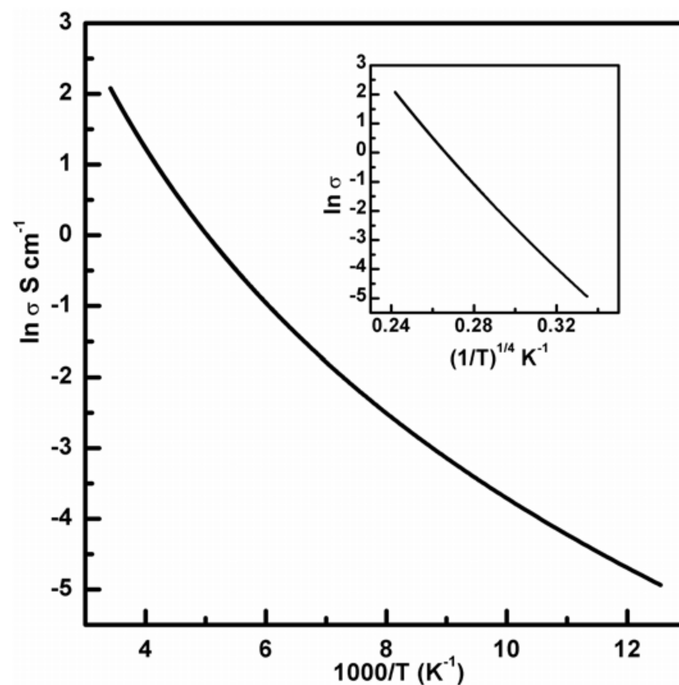

Figure 6.8. The temperature dependence of the conductivity of oxygen intercalated Ca doped $CuYO_2$ films. Inset shows the ln σ vs $T^{-1/4}$ plot.

All the films were p-type as confirmed by the measurement of Seebeck coefficient. The highest value of Seebeck coefficient (+274μVK^{-1}) was obtained for films annealed in oxygen at atmospheric pressure at 420 ^{0}C for 20 minutes (Fig 6.9).

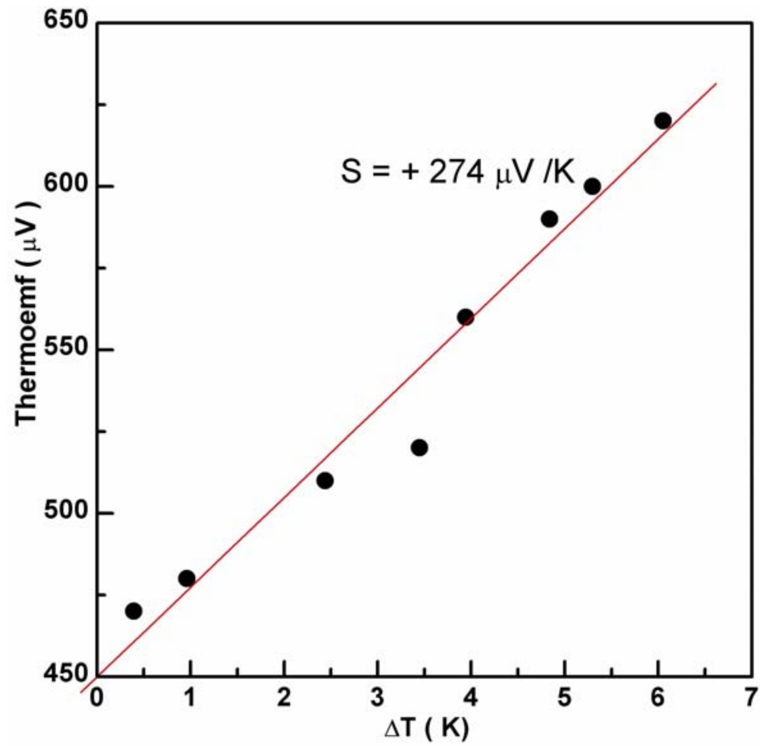

Figure 6.9. Thermopower of Ca doped $CuYO_2$ thin films annealed at 420°C under 1 atm oxygen pressure

Figure 6.10 shows the PL emission spectra and figure 6.11 shows the excitation spectra of the thin films and bulk powder samples. The undoped $CuYO_2$ powder shows a broad green fluorescence emission peaking at 545 nm with sharp shoulder peaks at 465 nm and 559 nm under excitation with 340 nm at room temperature.

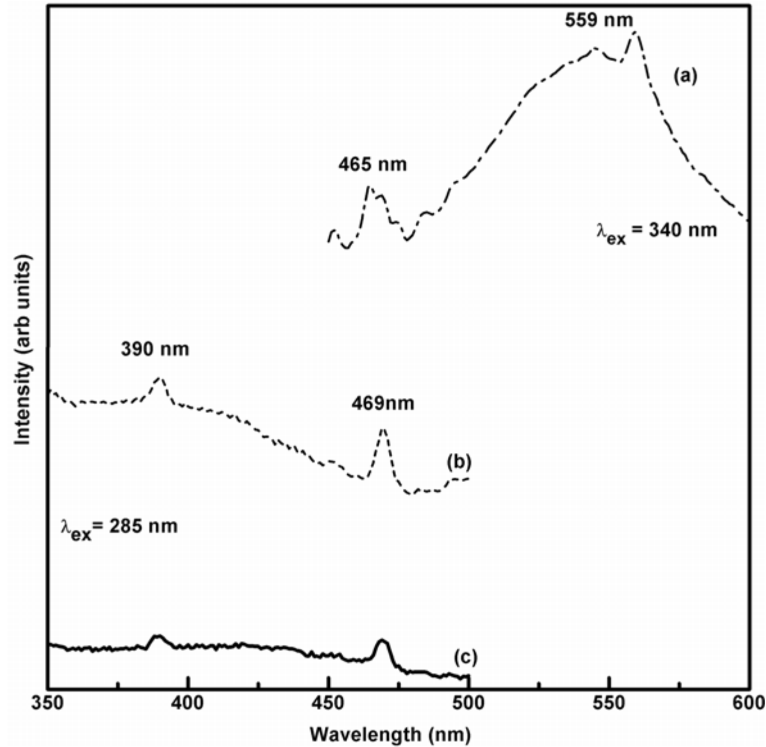

Figure 6.10. Emission spectra of (a) Pure $CuYO_2$ powder (b) Ca doped thin film samples and (c) emission spectra of Ca doped $CuYO_2$ bulk sample.

The green fluorescence emission can be attributed to $3d^{10} – 3d^9\ 4s^1$ transition [29]. The emission spectra of 2% Ca doped $CuYO_2$ powder as well as the thin films (Fig 6.10) shows that the green fluorescence (broad band 545 nm) is completely quenched and the shoulder peak at 465 nm is not affected by Ca doping. The Ca which forms an acceptor level within the energy gap of the molecular orbitals generating from the hybridization of $3d(_z2)$ - 4s and $3d(_z2)$ + 4s orbitals. The green fluorescence due to the transition $3d^{10} – 3d^9$ $4s^1$ maybe getting quenched because of the non radiative transition via the acceptor levels.

The Ca which forms an acceptor level within the energy gap of the molecular orbitals generating from the hybridization of $3d(_z2)$ - 4s and $3d(_z2)$ + 4s orbitals. The green fluorescence due to the transition $3d^{10} – 3d^9\ 4s^1$ maybe getting quenched because of the non radiative transition via the

acceptor levels. However the PLE and the PL emission spectra of the Ca doped $CuYO_2$ thin film is exactly identical with that of the Ca doped $CuYO_2$ bulk powder indicating the incorporation of calcium into the film

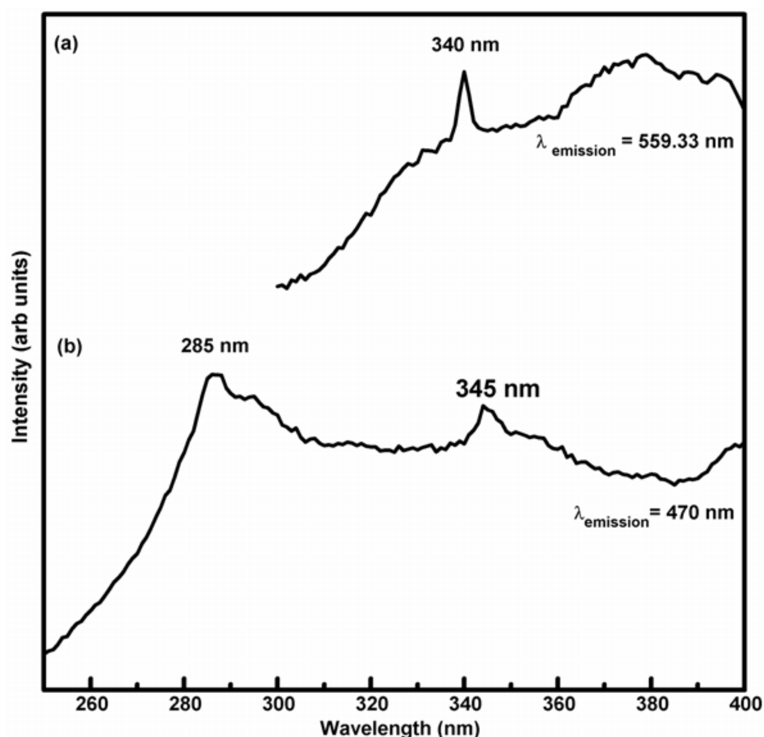

Figure 6.11. Excitation spectra of (a) Pure $CuYO_2$ powder (b) Ca doped $CuYO_2$ powder.

The junctions formed with p type $CuYO_2$:Ca and n type ZnO:Al thin films show non linear behaviour as shown in figure 6.12. The ratio of forward to reverse current is 1.3 at 4V. The transparency of the device is 45% at 550nm. The current can be increased by increasing the charge carriers in the p type $CuYO_2$:Ca thin films. Improving the interface of the p and n type would also improve the characteristics of the device.

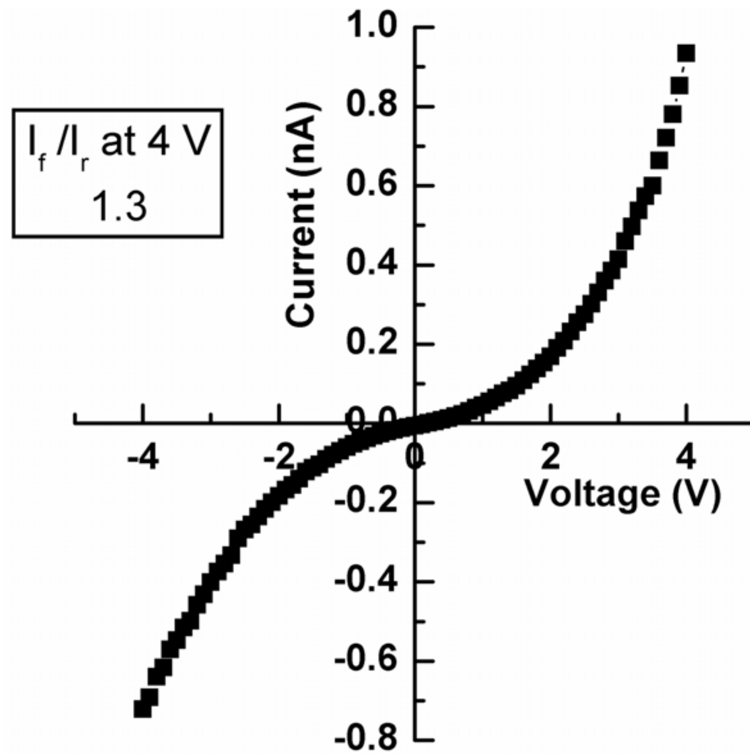

Figure 6.12. IV characteristics of junction of n type ZnO:Al deposited by PLD on p type $CuYO_2$:Ca deposited by rf magnetron sputtering

6.4. Conclusion

The Ca doped $CuYO_2$ thin films prepared by RF magnetron sputtering show p-type conductivity (8 Scm^{-1}) after the oxygen intercalation. The conductivity can be increased by oxygen intercalation but at the expense of transmission. The Seebeck coefficient of +274 $\mu V K^{-1}$ confirms the p-type conduction in these materials. The temperature dependence of the conductivity indicates a predominant hopping conduction mechanism. The films become amorphous on annealing at one atmosphere oxygen pressure. The junction fabricated with n type ZnO:Al and p type $CuYO_2$:Ca show a forward to reverse ratio of 1.3 at 4V.

6.5 References

[1.] K.L Chopra, S. Major, and D. K. Pandya, Thin solid films **102** (1983) 1

[2.] T. Yamamoto and H. K Yoshida , Jpn.J.Appl.Phys **38** (1999) L166.

[3.] D. C. look, D. C. Reynolds, C. W. Litton, R. C. Jones, D. B. Eason and G. Cantwell, Appl Phys Lett. **81** (2002) 1830.

[4.] M. Joseph, H. Tabata, H. Sacki, K. Ueda, T. Kawai , Physica B **302-303** (2001) 140.

[5.] K. Minegishi, Y. Koui, K. Kikuchi, Jpn J Appl Phys **36** (1997) L1453.

[6.] X. L. Gao, H. Tabata, T. Kawa, J Cryst Growth **223** (2001) 135.

[7.] Y. R. Ryu, S. Zhu, D. C. Look, J. W. Wrobel, H. W. Joeng and H. W. White, J.Cryst Growth **216** (2001) 330

[8.] Y. Ryu, T. S. Lee H. W. White, Appl Phys Lett. **83** (2003) 87.

[9.] K. K. Kim, H. S. Kim,D. K. Hawang, J. H. Lim, and S. J. Park, Appl Phys Lett. **63** (2003) 63.

[10.] H. Sato, T. Minami, S. Takata, and T. Yamada, Thin Solid films **236** (1993) 27.

[11.] H. Kawazoe, M. Yasukawa, H. Hyodo, M. Kurita, H. Yanagi, and H. Hosono, Nature **389** (1997) 939.

[12.] G. Thomas, Nature **389** (1997) 907.

[13.] M.K.Jayaraj, A. D. Draeseke, J.Tate, and A.W.Sleight, Thin solid films **397**(2001) 244

[14.] N. Duan, A. W. Sleight, M. K.Jayaraj, and J.Tate, Appl Phys Lett **77**(2000) 1325.

[15.] R. Nagarajan, A. D. Draeseke, A. W. Sleight, and J.Tate, J.Appl.Phys **89** (2001) 8022.

[16.] R. L. Hoffman, J. F. Wager, M. K. Jayaraj, and J.Tate , J.Appl Phys **90** (2001) 5763.

[17.] H. Kawazoe, H. Yanagi, K. Uede, and H. Hosono, MRS Bull **25** (200) 28.

[18.] J. Tate, M. K. Jayaraj, A. D. Dareseke, T. Ulbrich, A. W. Sleight, K. A. Vanaja, R. Nagarajan, and J. F. Wager, Thin Solid Films **411** (2002) 119.

[19.] H. Yanagi, K. Ueda, H. Ohata, M. Orita, H. Hirano, and H. Hosono, Solid State communication **121** (2001) 15.

[20.] R. D. Shannon, D. B. Rogers, and C.T. Prewitt, Inorg Chem **10** (1971) 713.

[21.] R. J. Cava, H. W. Zandbergen, A. P. Ramierz, H. Takagi, C. T. Chen, J. J. Krajewski, W. F. Peck.jr, J. V. Waszczak, G. Meigs, R. S. Roth, and L. F. Schneemeyer, J. Solid state chem. **104** (1993) 437.

[22.] R. J. Cava, W. F. Peck.jr, J. J. Krajewski, S. W. Chenog, and H. Y. Hwang, J.Mater Res **9** (1994) 314.

[23.] H. Yanagi, S. Park, A. D. Draeseke, D. A. Keszler and J.Tate, J. Solid state chem **175** (2003) 34.

[24.] JCPDS 37-930 and JCPDS 39-0224.

[25.] P. Y. Yu, M. Cardona Fundamentals of semiconductors: Physics and material properties, Springer, Berlin 1996.

[26.] B. E. Sernelius, K. F. Berggren, Z. C. Jin, I. Hamberg, and C. G. Granqvist, Phys. Rev. B **37** (1988) 10244.

[27.] K. F. Berggern and B. E. Sernelius Physical Review B **24** (1981) 1971.

[28.] N. F. Mott Metal-insulator transitions, Taylor and Francis, London, 1974.

[29.] A. Jacob, C.Parent, P. Boutinaud, G.L. Flem, J. P. Doumerc, A. Ammar, M.Elazhari and M. Elaatmani , Solid State Communications **103** (1997) 529.

CHAPTER 7

Summary and Outlook

7.1.Summary

Development of p and n type transparent conducting oxides will open up new and exciting applications. The active devices that are transparent to visible light including diodes, transistors and field effect transistors can be fabricated. Comparing the surface features of sputtered and PLD films clearly indicate that the films obtained by PLD are smoother. Room temperature deposition is also possible with PLD. Though off axis sputtering gives films with smoother surfaces PLD still has the advantage of being able to deposit films at room temperature. Pulsed laser deposition can be used to deposit thin transparent films on flexible plastic substrates. Active transparent devices can be fabricated on flexible substrates at room temperature.

The carrier concentration and the film thickness need to be optimised for better device performance. The deposition of individual layers can be optimised for smooth surfaces thereby improving the p – n interface. This would also improve the device performance.

The delafossites are less transparent than ZnO thin films. Devices fabricated with ZnO homojunctions have better transmittance than the devices fabricated with delafossite/ZnO hetrojunctions.

Trying to develop p type ZnO by understanding the basic mechanism of p type conductivity in those films would be a worthwhile exercise. The setup that was fabricated to measure the thermopower can be modified to measure other transport properties thereby giving valuable insight to the conduction mechanism in p type ZnO. Slight modification in the sample preparation and setup can give in addition to the Seebeck coefficient, Hall coefficient, Resistivity and Nernst coefficient. This would reveal the fermi level, the density of states effective mass and energy dependent scattering parameter related to a relaxation time. Measuring these coefficients over different temperatures would provide valuable insight into the transport phenomena in thin film samples.

In summary off axis sputtering and PLD with 355nm can produce smooth films. These methods can be used to deposit p and n TCO films with smooth surfaces. The junctions formed would give good device performance.
Room temperature deposition of thin films is possible with PLD. Transparent active devices can be deposited on flexible plastic substrate at room temperature by PLD.

All oxide devices are being fabricated and they use of the potential advantages of transparency, high temperature performance and radiation hardness[3]. Transparent thin film transistor (TFT) utilising TCO as channel layer has several merits compared to flat panel displays. The oxide TFT has advantage over the semiconductor FET in high voltage, temperature tolerances and are insensitive to visible light radiation..
UV–LED is a typical active device utilising optical transparency and p–n junction. Although ZnO is a known UV emitter at room temperature. Near UV emission has been achieved by p type $SrCu_2O_2$ and n type ZnO.[4]. Improving the device that was fabricated in the present study will yield UV emitting LEDs.

Oxide semiconductors exhibit higher carrier mobilites even in amorphous form compared to the amorphous elemental semiconductors. The TCOs, such as ZnO and SnO_2, the conduction band minimum(CBM) are mainly made of s orbitals with a large principle quantum number n. These s orbitals have a large spatial size and form hybridation even with second neighbour metal cations. This means TCOs can have good electric conductivity at high carrier densities. Thus amorphous oxide semiconductors are insensitive to local strained bonds and electron transport is not effected significantly. [5] amorphous semiconductors based devices have uniform characteristics so that large displays can be fabricated on flexible substrates. The amorphous semiconductor (InGaZnO) based TFT have high mobility (>10 $cm^2 V^{-1} s^{-1}$) and large on off currrent ratios (>10^5) [6] Amorphous semiconductors are better suited to be grown on flexible substrates than conventional semiconductors. Development of transparent

electronics on flexible substrate would be greatly facilitated by developing the amorphous semiconductor devices.

Flexible and transparent electronics are becomming a reality and will find applications in advanced optoelectronic applications such as wearable computers and displays attachable to windows.

The oxide electronics on flexible substrates have advantages like flexibility, light weight, ruggedness and low cost. The successful of fabricating all oxide based thin films transistors, LED and other electronic components on flexible substrates is a key technique to realise flexible transparent electronics. The horizon of flexible and oxide electronics is much closer and it opens up new applications that have never been thought of before.

7.2 References

[1.] Hiroshi Yanagi, Transparent p/n type oxide semiconductors with delafossite structure: Chemical design and material exploration. Thesis (2001).

[2.] D.L.Young and T.J.Coutts and V.I. Kaydanov, Review of Scientific instruments **71** (2000) 462.

[3.] A.Kudo, H.Yanagi, K.Ueda, H.Hosono, H.Kawazoe and Y. Yano, Appl. Phy. Lett. **75** (1999) 285.

[4.] H Ohata, K Kawamura, M Oita, N Sarukura, H Hosono, Appl. Phys. Lett. **77** (2000) 475.

[5.] Toshio Kamiya, and Hideo Hosono, Int. J. Appl. Ceram. Technol. **2** (2005) 285.

[6.] K. Nomura, A. Takagi, T. Kamiya, H. Ohta, M. Hirano and H. Hosono, Jap. J. Appl. Phys. **45** (2006) 4303.

Appendix

Programme for the PID controller

```
#include<stdio.h>
#include<conio.h>
#include<dos.h>
#include<graphics.h>
#include <bios.h>
#include <math.h>
#include <string.h>
#include <ieee-c.h>

#define K195 16

float set_temp, pb, int_t, der_t, pvmax, pvmin;
float sens=0.0000408;
float v_max;
float v_min;

void screen(void);
float convert(char a[80]);
 float read_in (void)
{
   int status=1,l,poll;
   char r[80];
   float val;
   initialize (21,0);      /* make PC a controller at address 21 */
  while(status!=0)
{
   send (K195,"READ?",&status );     /* device command to set mode */
   enter (r,80,&l,K195,&status );    /* read a voltage */
 }
   val=convert(r);
   return val;
```

```
}


float convert(char a[80])
{
char *rvalue,rno[30],expsign;
int length,dummyin,ddn,dummyin2,dummyin22,voltage,expval;
float mul;
float value=0;
length=0;
rvalue=a;
for (dummyin=1;rvalue[dummyin]!='N';dummyin+=1)
          {
        length+=1;
        if(rvalue[dummyin]=='.')
                  dummyin2=dummyin+1;
        if(rvalue[dummyin]=='E')
             {
              dummyin22=dummyin+1;
                    expsign= rvalue[dummyin+1];
              expval=  (rvalue[dummyin+2]-48)*10+(rvalue[dummyin+3]-48)  ;
               }
             }
        for (dummyin=1;dummyin<=dummyin2-2;dummyin+=1)
        {  mul=1;
          for(ddn=dummyin2-2-dummyin;ddn>0;ddn-=1)
             mul=mul*10;
          value=value+((rvalue[dummyin]-48)*mul);
            }
        for (dummyin=dummyin2;dummyin<=dummyin22-2;dummyin+=1)
        {  mul=1;
          for(ddn=dummyin-dummyin2;ddn>=0;ddn-=1)
             mul=mul/10;
          value=value+((rvalue[dummyin]-48)*mul);
```

```
            }



            mul=1;
        for(ddn=expval;ddn>0;ddn-=1)
        mul=mul*10;
        if(expsign=='+')
        value=value*mul;
        else
            value=value/mul;
        if (rvalue[0]=='-')
        value=0-value;
return value;
}
void  data_in()
{
            clrscr();
            printf("\n\t\tEnter Set Temperature: ");
            scanf("%f",&set_temp);
            printf("\n\t\tEnter Proportional Band: ");
            scanf("%f",&pb);
            printf("\n\t\tEnter Integral Time: ");
            scanf("%f",&int_t);
            printf("\n\t\tEnter Derivative time: ");
            scanf("%f",&der_t);
            printf("\n\t\tEnter Process Value Max: ");
            scanf("%f",&pvmax);
            printf("\n\t\tEnter Process Value Min: ");
            scanf("%f",&pvmin);
v_max=pvmax*sens;
v_min=pvmin*sens;
}
```

```
void out_volt(float c_out)
 {
        int a =((c_out+10)/20)*4096;
        int b=a;
        b>>=8;
        int low_byte=a&=0xff;
        int high_byte=b&=0xff;
        outport(0x31d,high_byte);
        outport(0x31c,low_byte);
 }
 void new_set()
        {
        closegraph();
        clrscr();
        printf("\n\n\n\tEnter Set Temperature: ");
        scanf("%f",&set_temp);
        printf("\n\n\tEnter Proportional Band: ");
        scanf("%f",&pb);
        printf("\n\n\tEnter Integral Time: ");
        scanf("%f",&int_t);
        printf("\n\n\tEnter Derivative time: ");
        scanf("%f",&der_t);

        }
void screen(void)
{
         int gdriver = DETECT, gmode ;
        initgraph(&gdriver, &gmode, "c:\\tc\\bgi"); /* initialize graphics
mode */
```

```
start: setbkcolor(0);
        setcolor(3);
        line(75,10,575,10);
        line(75,10,75,350);
        line(75,350,575,350);
        line(575,10,575,350);
        line(75,95,575,95);
        line(75,180,575,180);
        line(75,265,575,265);
        float y_sp;
        float y_span=(pvmax-pvmin)/4;
                gotoxy(5,1);
                printf("%3.1f",pvmax);
                gotoxy(6,6);
                printf("%3.1f",(pvmax-y_span));
                gotoxy(6,12);
                printf("%3.1f",(pvmax-2*y_span));
                gotoxy(6,17);
                printf("%3.1f",(pvmax-3*y_span));
                gotoxy(6,22);
                printf("%3.1f",(pvmax-4*y_span));
                gotoxy(73,1);printf("100");
                gotoxy(73,6);printf("75");
                gotoxy(73,12);printf("50");
                gotoxy(73,17);printf("25");
                gotoxy(73,22);printf("0");
                gotoxy(10,23);printf("0");
```

```
			gotoxy(20,23);printf("100");
			gotoxy(30,23);printf("200");

			gotoxy(40,23);printf("300");
			gotoxy(50,23);printf("400");
			gotoxy(60,23);printf("500");
			gotoxy(70,23);printf("600");
			gotoxy(1,12);printf("PV");
			gotoxy(35,25);printf("Time(sec.)");
			setcolor(8);
			int set_y=(10+(340*pvmax)/(pvmax-pvmin))-
(340*set_temp/(pvmax-			pvmin));
			line(75,set_y,575,set_y);
			float x,y;
		x=(pvmax-pvmin)/(v_max-v_min);
		y=pvmax-(v_max*x);
		float de;
		float deo=0;
		float sum=0;
		float dde,pi,pd;
		int count2=75;
 loop: int count1;
		float val;
		float val4[20];
		float val1[20];
		for(count1=0;count1<20;count1++)
		{
		float val2;
		val=read_in();
```

```
val=(val*x)+y;
val1[count1]=val;
val2=val;
 de=(set_temp-val2)/(pvmax-pvmin);
dde=de-deo;
deo=de;



sum=sum+de;
pi=(100/pb)*(1/int_t)*.1*sum;
pd=(100/pb)*der_t*(dde/.1);
val2=((100*de/pb)+pi+pd)*10;
if(val2>9.995)val2=9.995;
if(val2<0)val2=0;
out_volt(val2);
val4[count1]=val2;
delay(120);
}
float val3=0,val5=0;
for(int n=0;n<20;n++)
        { val3=val3+val1[n];
          val5=val5+val4[n];
         }
val=val3/20;
val5=val5/20;
int pv_y=(10+(340*pvmax)/(pvmax-pvmin))-(340*val/(pvmax-
pvmin));
int co_y=350-(34*val5);
putpixel(count2,pv_y,2);
putpixel(count2,co_y,4);
gotoxy(50,3);
printf("<-- PV= %3.3f",val);
gotoxy(50,5);
```

```
printf("    CO= %3.0f %   -->",val5*10);
gotoxy(15,2);
printf("SP= %3.2f",set_temp);
gotoxy(15,3);
printf("P= %3.1f",pb);
gotoxy(15,4);
printf("I= %3.1f",int_t);
gotoxy(15,5);



printf("D= %3.1f",der_t);
count2++;
if(count2>575)goto start;
if(bioskey(1)==0)goto loop;
}
void main()
{
data_in ();
loop1: screen();
char key=bioskey(0);
if(key=='c')
        {
        new_set();
        goto loop1;
        }
out_volt(-1);
getch();
getch();

}
```